

2014-06-30

# Interfacial and Spectroscopic Studies of Biomacromolecules and CdSe(ZnS) Quantum Dots

Nicholas F. Crawford

*University of Miami*, n.crawford1@umiami.edu

Follow this and additional works at: [https://scholarlyrepository.miami.edu/oa\\_dissertations](https://scholarlyrepository.miami.edu/oa_dissertations)

---

## Recommended Citation

Crawford, Nicholas F., "Interfacial and Spectroscopic Studies of Biomacromolecules and CdSe(ZnS) Quantum Dots" (2014). *Open Access Dissertations*. 1242.

[https://scholarlyrepository.miami.edu/oa\\_dissertations/1242](https://scholarlyrepository.miami.edu/oa_dissertations/1242)

This Open access is brought to you for free and open access by the Electronic Theses and Dissertations at Scholarly Repository. It has been accepted for inclusion in Open Access Dissertations by an authorized administrator of Scholarly Repository. For more information, please contact [repository.library@miami.edu](mailto:repository.library@miami.edu).

UNIVERSITY OF MIAMI

INTERFACIAL AND SPECTROSCOPIC STUDIES OF BIOMACROMOLECULES  
AND CdSe(ZnS) QUANTUM DOTS

By

Nicholas Franklin Crawford

A DISSERTATION

Submitted to the Faculty  
of the University of Miami  
in partial fulfillment of the requirements for  
the degree of Doctor of Philosophy

Coral Gables, Florida

August 2014

©2014  
Nicholas Franklin Crawford  
All Rights Reserved

UNIVERSITY OF MIAMI

A dissertation submitted in partial fulfillment of  
the requirements for the degree of  
Doctor of Philosophy

INTERFACIAL AND SPECTROSCOPIC STUDIES OF BIOMACROMOLECULES  
AND CdSe(ZnS) QUANTUM DOTS

Nicholas Franklin Crawford

Approved:

\_\_\_\_\_  
Roger. M. Leblanc, Ph.D.  
Professor of Chemistry

\_\_\_\_\_  
Jamie D. Walls, Ph.D.  
Professor of Chemistry

\_\_\_\_\_  
Burjor K. Captain, Ph.D.  
Professor of Chemistry

\_\_\_\_\_  
M. Brian Blake, Ph.D.  
Dean of the Graduate School

\_\_\_\_\_  
Kerim M. Gattás Asfura, Ph.D.  
Post Doctoral Associate  
Diabetes Research Institution

CRAWFORD, NICHOLAS FRANKLIN

(Ph.D., Chemistry)

Interfacial and Spectroscopic Studies of  
Biomacromolecules and CdSe(ZnS) Quantum Dots

(August 2014)

Abstract of a dissertation at the University of Miami.

Dissertation supervised by Professor Roger M. Leblanc.

No. of pages in text. (116)

Understanding of biomacromolecule interactions at the molecular level raises certain difficulties however with the Langmuir monolayer technique, interfacial interactions in two dimensions can be accurately measured to access and characterize physical, electrostatic and photophysical properties. Macromolecules such as serum albumin which comprises 50% of human blood plasma protein content is one focus of research in this thesis for its unique involvement in many biological functions. The important nature of this class of protein demands that it be studied in detail while modifying the experimental conditions in two dimensions to observe it in all types of environments. While different from bulk colloidal solution work, the two dimensional approach allows for the observation of the interaction between molecules and subphase at the air-water interface. Compiled in this thesis are studies which highlight the characterization of this protein using various surroundings and also observing the types of interactions it would have when at the biomembrane interface. Free-energy changes between molecules, packing status of the bulk analyte at the interface as well as phase transitions as the monolayer forms a more organized or aggregated state are just some of the characteristics which are observed through the Langmuir technique. This unique methodology demonstrates the chemical and physical behavior of this protein at the phase boundary throughout the compression of the monolayer.

$\beta$ -galactosidase (Escherichia coli 3.2.1.23) is a naturally occurring, regenerating enzyme which specifically hydrolyzes the  $\beta$ -D-galactosyl linkage of lactose molecules into usable sources of carbon. Spectroscopic techniques were utilized to analyze  $\beta$ -galactosidase in its native state and in different environmental aqueous conditions as well as changes of interfacial properties and conformation investigated through surface chemistry and *in situ* spectroscopy.

Characteristic for proteins consisting of tryptophan residues, UV-vis absorption was analyzed to observe changes in enzyme concentration revealing near its isoelectric point (4.6),  $\beta$ -galactosidase is most susceptible to monomer aggregation. Circular dichroism studies showed environmental aqueous alkaline conditions causes an increase in  $\alpha$ -helix and a decrease in  $\beta$ -sheet content while the opposite effect was observed in acidic conditions, increasing the  $\beta$ -sheet content to a maximum of 43% and a minimum of  $\alpha$ -helix content to 5%. Fluorescence assays showed that tryptophan emissions decreased over a short term of irradiation during experimentation leading to the conclusion that  $\beta$ -galactosidase fluorescence quenching is due to the non-radiative energy transfer of excited state donors to ground state acceptors while undergoing no major secondary structure changes. Substrate studies were conducted in order to calculate the Michaelis constant of X-gal, a glycoside substrate which undergoes hydrolysis in the presence of the enzyme. Analysis and comparison of the Michaelis constant of other known glycosides shows that X-gal has a high affinity for  $\beta$ -galactosidase.

Conditions for an optimal Langmuir monolayer were firstly obtained by varying the subphase salt concentration and the surface pressure-area isotherm was used to extrapolate the limiting molecular area of the enzyme monolayer. Surface pressure

stability measurements along with compression-decompression cycles revealed no aggregate formation. Consistent with the high content of tryptophan along with the data obtained from the isotherm, *in situ* UV-vis and fluorescence spectroscopy shows a steep rise in absorbance and photoluminescent intensity correlating to with a switch from a liquid-expanded to a liquid-condensed phase. The secondary structure, analyzed by infrared reflection-absorption spectroscopy of the monolayer at the air-water interface confirmed the stability of the enzyme evidenced by signal intensification as a function of increased surface pressure. A decrease in subphase pH increased the electrostatic repulsion as the enzyme was protonated leading to an expanded monolayer, increased the  $\beta$ -sheet content in the amide I region as well as increased the  $\alpha$ -helix content in the amide II region.

Recent years have produced many advances in quantum dot synthesis, application and analysis while their importance in the fields of chemistry, biology, engineering and physics has grown as well. Opposed to the bulk state properties, quantum dots are dependent upon the quantum confinement effect in all three spatial dimensions and so their applications have been broadened to optical switches and fluorescence labeling among others. Compiled here are extensive results in the characterization of CdSe(ZnS)-TOPO quantum dots using the Langmuir monolayer technique to approach these quantum dots in their two dimensional state as well as variation of ligands DHLA and MPS around the nanoparticles . Properties such as the limiting nanoparticle area, molar absorptivity, and self-assembly manipulation have shown the packing structure of the quantum dots at the air-water interface.

All of this is possible because of the love and support from all of my family members throughout my academic career. To my mom, since the first day of school standing on those front steps taking pictures of Robert and me, you have been a shining light of inspiration and have taught me that with hard work and dedication anything is possible when nurtured with love. To my dad, who I've seen work hard every day to provide a life and future for his family. You have taught me many lessons of life and history but the one I find most memorable is when you said, "You have your whole life to work, enjoy the times you have with the ones you love." To my big brother, Robert, the influence of growing with you and learning from you has always inspired me to push the boundaries of knowledge and understanding. Good things come to those who wait.

Karolina, my wife, my love. Your beauty is only surpassed by your intelligence and your hunger to learn and grow. Distance has only made the heart grow fonder and I am thankful every day that we took this leap together.

Our journey continues, turn these pages with me, I come home now.

*"Be a thinker, not a stinker!"*

*- Carl Weathers (Apollo Creed)*



## ACKNOWLEDGEMENTS

My dissertation is the product of hard work and dedication to the scientific method, all of which would not have been possible without my research advisor, Dr. Roger M. Leblanc. His brilliant, scientific mind and tireless work ethic has shaped me as a researcher to think analytically with a spirit of enthusiasm for discovery. In my time as a graduate student, Dr. Leblanc has not only been a research advisor but also an authority on life lessons with his years as a professor, husband, father and friend. Never was any question answered without careful consideration and I take away from Dr. Leblanc the ability to lead not by saying “Go”, but, “Let’s go”.

I would like to give my sincere appreciation to my doctoral committee members, Professor Jamie D. Walls, Professor Burjor K. Captain and Dr. Kerim M. Gattás Asfura for their valuable support in my research career and academics.

Thank you to the staff and faculty of the Department of Chemistry throughout my time at the University of Miami. In particular, thank you to Sara Sucklal, Lydia Gonzalez, Susana Gadanyi, Marlene Triana, Ed Torres, Juanita and Raul Hernandez and a special thanks to Dr. Tegan Eve for your instructions and enthusiasm over these many fall, spring and summer sessions of teaching.

I would like to thank present group members including Eric Waidely, Lorenzo Sansalone and Jerome Mulloor for all their support and collaboration. Special thanks to Shanghao Li and Sheba Johnson Kuruvilla who have been with me throughout my graduate career sharing in my success and encouraging through distress. I wish you the best in all your future careers and endeavors of scientific discovery.

Thanks to all the students from France in the CESi program who have worked with me over several summers especially Mickaël Macquet, Baptiste Fleury, Damien Ribeiro, Claire Gabet, Jean Legrand and Gaetan Gontier for all the good times in and outside the lab. Thank you to all my fellow graduate students in my class and the department, especially Randy Lawrence for all your encouragement and support in this past year. Also thanks to past group members Dr. Garima Thakur, Dr. Jianmin Xu, Dr. Chengshan Wang for their help with research.

Finally, I come to my good friends Preston Elliot, Steve Morrison, Casey “Boy” Foster, Nick McIlwain, Kathy Romano, Marisa Magnatta and all the interns. You have consistently put a smile on my face every day starting from my years in high school. Thank you for your comedy, kindness and works of charity which remind me of where I come from and who I want to be in life.

## TABLE OF CONTENTS

	Page
LIST OF FIGURES .....	x
LIST OF TABLES .....	xvi
LIST OF SCHEMES.....	xvii
LIST OF ABBREVIATIONS.....	xviii
<b>Chapter</b>	
<b>1. Introduction</b>	
1.1 The secondary structure of proteins.....	1
<i><math>\alpha</math>-helix</i> .....	1
<i><math>\beta</math>-sheet</i> .....	2
1.2 Human serum albumin.....	4
1.3 $\beta$ -galactosidase.....	5
1.4 The Langmuir technique.....	8
1.5 Spectroscopy.....	12
<i>UV-vis absorption and fluorescence spectroscopy</i> .....	12
<i>Circular Dichroism</i> .....	13
<i>Infrared Absorption-Reflection Spectroscopy</i> .....	14
1.6 Semiconductor Quantum Dots .....	15
1.7 Summary.....	19
<b>2. Experimental</b>	
2.1 Materials.....	22
2.2 Methods for spectroscopy and surface chemistry.....	23

2.2.1	Spectroscopy.....	23
	<i>Absorption</i> .....	23
	<i>Fluorescence</i> .....	25
	<i>Circular Dichroism</i> .....	26
	<i>Mass Spectrometry</i> .....	27
	<i>Transmission Electron Microscopy</i> .....	28
2.2.2	Surface Chemistry.....	28
	<i>Surface pressure-area isotherms</i> .....	28
	<i>Surface potential-area isotherms</i> .....	29
	<i>Infrared absorption-reflection spectroscopy</i> .....	30
2.3	Preparation of solution for Langmuir technique.....	31
	<i>Langmuir monolayer preparation</i> .....	31
	<i>In situ protein fibrillation</i> .....	32
2.4	Synthesis of QDs and Conjugates.....	33
	<i>Synthesis of CdSe(ZnS) Core(Shell) QDs</i> .....	33
	<i>Dihydrolipoic acid synthesis</i> .....	34
	<i>CdSe(ZnS)-TOPO ligand exchange to CdSe(ZnS)-DHLA</i> .....	34
	<i>CdSe(ZnS)-TOPO ligand exchange to CdSe(ZnS)-MPS</i> .....	35
2.5	Summary.....	35
<b>3.</b>	<b>Surface Chemistry and Spectroscopy of the Human Serum Albumin</b>	
	<b>Langmuir Monolayer</b>	
	Background.....	36
3.1	Surface chemistry of the human serum albumin Langmuir monolayer.....	37

<i>Salt concentration effect</i> .....	37
<i>Effect of pH on the HSA Langmuir monolayer</i> .....	40
<i>Compression-decompression cycles of the HSA Langmuir monolayer</i> .....	42
<i>Stability measurements of the HSA Langmuir monolayer</i> .....	44
3.2 Photophysical properties of human serum albumin.....	46
<i>UV-vis absorption and fluorescence spectroscopy in the aqueous phase</i> .....	46
<i>In situ UV-vis absorption of the HSA Langmuir monolayer</i> .....	47
<i>In situ fluorescence spectroscopy of the HSA Langmuir monolayer ...</i>	49
<i>In situ protein fibrillation</i> .....	51
3.3 Conclusion.....	52
<b>4. <math>\beta</math>-galactosidase</b>	
Background.....	54
4.1 Photophysical properties of $\beta$ -galactosidase.....	55
<i>UV-vis and fluorescence emission spectra</i> .....	55
<i>Aggregation analysis via UV-vis absorption</i> .....	56
<i>Circular dichroism spectropolarimeter</i> .....	57
<i>Fluorescence quenching over time</i> .....	59
4.2 Substrate interaction studies.....	64
<i>Michaelis-Menten constant determination: <math>\beta</math>-galactosidase interaction with X-gal</i> .....	64
4.3 Surface chemistry of the $\beta$ -galactosidase Langmuir monolayer.....	68
<i>Surface pressure- and surface potential-area isotherms</i> .....	68

<i>Compression-decompression cycles and stability measurements of the <math>\beta</math>-galactosidase Langmuir monolayer.</i> .....	71
4.4 Conformation studies of the $\beta$ -galactosidase Langmuir monolayer using IRRAS.....	74
<i>Effect of pH on the limiting molecular area</i> .....	74
<i>Infrared absorption-reflection spectroscopy of the native enzyme</i> .....	76
<i>Effect of pH on the native enzyme</i> .....	79
4.5 <i>In situ</i> photophysical properties of the $\beta$ -galactosidase Langmuir monolayer.....	81
<i>UV-vis absorption and fluorescence spectroscopy</i> .....	81
4.6 Conclusion.....	83
<b>5. Characterization of Quantum Dots</b>	
Background.....	85
5.1 Characterization by spectroscopy and microscopy.....	86
<i>UV-vis absorbance spectroscopy</i> .....	86
<i>Fluorescence spectroscopy</i> .....	88
<i>Transmission Electron Microscopy</i> .....	91
5.2 Surface chemistry of the QD Langmuir monolayer.....	92
<i>CdSe-TOPO</i> .....	93
<i>CdSe(ZnS)-TOPO</i> .....	94
<i>CdSe(ZnS)-DHLA</i> .....	96
<i>CdSe(ZnS)-MPS</i> .....	97
5.3 Conclusion.....	99

<b>6. Future Directions</b>	
6.1 Protein-lipid interactions.....	100
<i>Rationale</i> .....	100
<i>Objective</i> .....	100
6.2 Solid support studies of biomacromolecules.....	102
<i>Rationale</i> .....	102
<i>Objective</i> .....	102
<b>REFERENCES</b> .....	106

## LIST OF FIGURES

### Chapter 1

- Figure 1.1.** The most common secondary structure, the  $\alpha$ -helix is a right-handed coil conformation stabilized by hydrogen bonding through the peptide backbone.....2
- Figure 1.2.** The second most common secondary structure, the  $\beta$ -sheet conformation is also stabilized by hydrogen bonding and can be oriented in (A) parallel, continuous N- to C- terminus, arrangement or (B) anti-parallel, arranged with termini next to each other in opposite directions.....3
- Figure 1.3.** Cartoon representation of human serum albumin showing the three domains which consist mostly of  $\alpha$ -helix (62%),  $\beta$ -sheet (5%) and random coils (33%).....5
- Figure 1.4.** Two cartoon representations of  $\beta$ -galactosidase which shows (A) the four monomers in different colors which complete the tetramer and (B) the secondary structures of the tetramer which is mostly comprised of  $\beta$ -sheets (40%) and  $\alpha$ -helices (35%) with random coils (12%) and  $\beta$ -turns (13%)...7
- Figure 1.5.** Model representation of the compression of molecules at the air-subphase interface already highly ordered with minimal degrees of freedom due to the compression by the barriers. After this point in the monolayer, the molecules are exerting a large amount of surface pressure on the Wilhelmy plate and might collapse into multiple layers.....10
- Figure 1.6.** Surface pressure-area isotherm of ideal amphiphilic molecules which shows a minimal degree of interaction upon compression at the air-subphase interface during the gaseous (G) phase. Hydrophobic molecular interactions are correlated with the rise in surface pressure as the molecules reorient themselves while in an initial liquid-expanded (L-C1) phase. Further compression of this liquid-condensed (L-C2) phase correlates to a sudden rise in surface pressure after a kink ending in the collapse of the monolayer into multiple layers.....12
- Figure 1.7.** At low temperatures, the three types of materials can be simplified in understanding their propensity to allow the flow of electrons when an electric field is applied. The boxes show that metals have a small band gap, Eg, and their lower valence shell is not completely full allowing electrons to move freely into the upper conductance band. Semiconductors and insulator on the other hand have completely filled valence bands and different sized band gaps giving them particular properties.....17



## Chapter 2

- Figure 2.1.** Model of sample excitation and fluorescence emission detection setup with a view of the 1 cm optical path length quartz cuvette.....26
- Figure 2.2.** Circular dichroism spectra of proteins which with representative secondary structures showing  $\alpha$ -helix (solid line),  $\beta$ -sheet (dashed line) and unordered (dotted line) conformation.....27

## Chapter 3

- Figure 3.1.** The  $\pi$ -A isotherms for HSA spread on three different subphases at pH 5.7; pure water (■), 0.01 (●) and 0.1 (▼) M NaCl. The accompanying  $\Delta V$ -A isotherm (▲) on a 0.01 M NaCl subphase is shown which correlates well with the  $\pi$ -A isotherm.....38
- Figure 3.2.** Effect when spreading 0.15 nmol HSA on a 0.01 M NaCl subphase at pH 5.7 (■), 2 (●) and 12 (▼).....41
- Figure 3.3.** Compression-decompression cycles for the 0.15 nmol HSA Langmuir monolayer on a 0.01 M NaCl subphase up to (A) 10, (B) 15 and (C) 20 mN/m.....42
- Figure 3.4.** Stability measurements which show over an extended time period if the HSA monolayer can stay at the air-water interface when compressed to higher surface pressures of (A) 10, (B) 15 and (C) 20 mN/m.....45
- Figure 3.5.** UV-vis absorption and fluorescence spectra of an aqueous HSA solution in pure water, pH 5.7, with a 1 cm optical path length quartz cell analyzed. Analysis of the UV-vis spectrum at  $\lambda_{\max} = 278$  nm correlates to the single tryptophan residues  $\pi$  to  $\pi^*$  electronic transition and a concentration of 1.34 mg/mL (20.16  $\mu$ M). Fluorescence spectrum was produced from a solution concentration of 0.1 mg/mL (1.42  $\mu$ M) by excitation of the tryptophan residue in HSA at  $\lambda_{\text{exc}} = 285$  nm having a maximum intensity of emission at  $\lambda_{\text{em}} = 350$  nm.....47
- Figure 3.6.** *In situ* UV-vis absorption at the air-water interface of the HSA Langmuir monolayer formed on three different NaCl concentrations, pH 5.7; (■) pure water, (●) 0.01 M NaCl and (▲) 0.1 M NaCl, analyzed at the maximum absorbance,  $\lambda_{\max} = 278$  nm, as a function of increasing surface pressure.....49
- Figure 3.7.** *In situ* fluorescence spectroscopy of HSA produced by 100  $\mu$ L of a 6 mg/mL solution on a 0.1 M NaCl subphase as compressed from 0 to 25 mN/m onto of a KSV trough with a slit width of 5 nm for both the excitation and emission spectra. Inset: Analysis at the  $\lambda_{\text{em}} = 350$  nm

corresponding to the tryptophan moiety in HSA as a function of surface pressure showing no indication of monolayer formation but rather a film as it increases steadily throughout compression.....50

**Figure 3.8.** Temperature induced HSA aggregation measured by *in situ* UV-vis absorption at a physiological temperature of 37°C showing two trends of aggregation when the monolayer is held at a surface pressure of 10 mN/m. The first six h of heating analyzed at  $\lambda_{\text{max}} = 278$  nm show a linear increase in absorbance while after this time the absorbance is constant.....52

## Chapter 4

**Figure 4.1.** Matrix-assisted laser desorption/ionization time of flight spectrum of  $\beta$ -galactosidase showing a monomer molecular weight of 116,646.1 Da.....54

**Figure 4.2.** UV-vis absorption and fluorescence spectra of an aqueous  $\beta$ -galactosidase solution in pure water, pH 5.7, with a 1 cm optical path length quartz cell. UV-vis analysis at  $\lambda_{\text{max}} = 282$  nm results in an enzyme concentration of 0.2 mg/mL (1.72  $\mu\text{M}$ ) using the  $E^{1\%}$  of 20.9. Fluorescence spectrum were produced after dilution of the enzyme by a factor of 10 (0.172  $\mu\text{M}$ ) with an excitation wavelength of  $\lambda_{\text{exc}} = 284$  nm having a maximum intensity of emission at  $\lambda_{\text{em}} = 354$  nm having slit widths of 3 nm for both.....56

**Figure 4.3.** UV-vis absorption of  $\beta$ -galactosidase solution (0.172  $\mu\text{M}$ ) with a 1 cm optical path length quartz cell by adjusting the aqueous environment to pH 2 (■), 3 (●), 4 (▲), 6 (▼), 8 (◄) and 10 (►) and analysis by UV-vis absorption spectroscopy. The  $\lambda_{\text{max}}$  over a 30 min time period increased in intensity for the pH 4 solution showing that near the pI of the enzyme there is an increase in concentration of  $\beta$ -galactosidase molecules related to the aggregation of the monomer in solution.....57

**Figure 4.4.** Circular dichroism analysis of 35 averaged scans over a 30 min time period of a  $\beta$ -galactosidase solution (0.172  $\mu\text{M}$ ) with a 0.2 cm optical path length quartz cell at different pH. As the pH is decreased from the pI of  $\beta$ -galactosidase (4.6),  $\beta$ -sheet content increases, and  $\alpha$ -helix content decreases. An increase in pH away from the pI reduces the  $\beta$ -sheet content and increase the  $\alpha$ -helix content.....58

**Figure 4.5.** Fluorescence quenching over a 20 min time period of a 0.2 mg/mL aqueous  $\beta$ -galactosidase solution in pure water, pH 5.7, with a 1 cm optical path length quartz cell. Spectra were recorded at (A) one and (B) five min intervals with an excitation wavelength of  $\lambda_{\text{exc}} = 284$  nm with slit widths of 3 nm for excitation and emission. (Inset) The maximum intensity of the emission spectra,  $\lambda_{\text{em}} = 354$  nm, was used to observe the quenching trend.....59

- Figure 4.6.** Fluorescence quenching trend of a 0.2 mg/mL aqueous  $\beta$ -galactosidase solution in pure water, pH 5.7, with a given amount of time for recovery using a single sample showed the quenching effect continued without full intensity recovery with different waiting-time periods between trials. Initial fluorescence quenching over a 30 min time period (■), 10 min waiting time period following by 30 min of fluorescence (●), subsequent 15 min waiting time period following by 30 min of fluorescence (▲), and subsequent 30 min waiting time period following by 30 min of fluorescence (▼).....60
- Figure 4.7.** Analysis of fluorescence emission of an aqueous  $\beta$ -galactosidase solution (0.2 mg/mL) in pure water, pH 5.7, at  $\lambda_{em} = 354$  nm with slit widths of 3 nm at different temperatures of 20 (■), 37 (●) and 60°C (▲) resulting in initial decrease in emission intensity but following the same quenching trend.....61
- Figure 4.8.** Fluorescence spectra analyzed at 354 nm after excitation at 284 nm having slit widths of 3 nm showing the quenching of a  $\beta$ -galactosidase solution (0.172  $\mu$ M) emission at (A) pH 4 (▲, ▼), (B) 2 (◀, ▶) and (C) 8 (◆, ◆), with little deviation from the sample in DI H<sub>2</sub>O (■, ●).....62
- Figure 4.9.** Circular dichroism before (■) and after (●) fluorescence quenching of a  $\beta$ -galactosidase solution (1.72  $\mu$ M) with a 0.2 cm optical path length. The spectra reveal little change in the secondary structure of the enzyme with the native enzyme having 6.2%  $\alpha$ -helix and 43%  $\beta$ -sheet before fluorescence and 6.5%  $\alpha$ -helix and 42.2%  $\beta$ -sheet after the quenching effects.....63
- Figure 4.10.** UV-vis absorption studies of  $\beta$ -galactosidase interacting with various concentration of X-gal (mg/mL); 0.02 (■), 0.10 (●), 0.15 (▲), 0.25 (▼), 0.35 (◀), 0.50 (▶). An increase in concentration of the substrate is correlated by an increased rate of hydrolysis allowing further analysis to determine the Michaelis constant for X-gal.....66
- Figure 4.11.** Lineweaver-Burk plot of X-gal interactions with  $\beta$ -galactosidase at different concentrations. Analysis of the plot allowed the Michaelis constant of X-gal to be calculated where the trend line crosses the x-axis,  $k_m = 6.13 \times 10^{-7}$  M.....67
- Figure 4.12.** Surface pressure-area and surface potential-area isotherms for 0.02 nmol  $\beta$ -galactosidase spread on a pH 5.7, 0.1 M NaCl subphase.....70
- Figure 4.13.** Compression-decompression cycles for the 0.02 nmol  $\beta$ -galactosidase Langmuir monolayer on a 0.1 M NaCl subphase up to (A) 10, (B) 20 and (C) 30 mN/m.....72

- Figure 4.14.** Stability measurements which shows over an extended time period if the  $\beta$ -galactosidase monolayer can stay at the air-water interface when compressed to higher surface pressures of (A) 20 and (B) 30 mN/m.....73
- Figure 4.15.** The shift of the  $\beta$ -galactosidase isotherm to a more expanded monolayer as the subphase pH is decreased. (Inset) Analysis of the decrease in mean molecular area as a function of increasing subphase pH at 20 mN/m showing a linear trend,  $y = -5972.8x + 55994$ ,  $R^2 = 0.9591$ .....74
- Figure 4.16.** IRRAS spectra for the 0.02 nmol  $\beta$ -galactosidase Langmuir monolayer spread on a pH 5.7, 0.1 M NaCl and irradiated with (A) p-polarized light and (B) s-polarized light at a 40° angle with increasing surface pressure.....77
- Figure 4.17.** The trends of major IRRAS wavenumbers in the amide I and II band region with decreasing subphase pH which show the enzyme monolayer at a surface pressure of (A) 0 and (B) 20 mN/m irradiated with p-polarized light at a 40° angle.....80
- Figure 4.18.** UV-vis absorption at the air-water interface of the  $\beta$ -galactosidase Langmuir monolayer from 0.02 nmol enzyme spread on a pH 5.7, 0.1 M NaCl subphase. (Inset) Analysis of the maximum absorbance,  $\lambda_{\max} = 282$  nm, as a function of increasing surface pressure.....82
- Figure 4.19.** Fluorescence spectra at the air-water interface of the  $\beta$ -galactosidase Langmuir monolayer from 0.02 nmol enzyme spread on a pH 5.7, 0.1 M NaCl subphase with scattering light at 420 nm subtracted. (Inset) Analysis of the maximum emission,  $\lambda_{\text{em}} = 354$  nm, as a function of increasing surface pressure.....83
- Chapter 5**
- Figure 5.1.** UV-vis absorption spectra of 13.4  $\mu\text{M}$  CdSe-TOPO (■), CdSe(ZnS)-TOPO (●), CdSe(ZnS)-DHLLA (▲) and CdSe(ZnS)-MPS (▼) dispersions with maximum absorbance at 525, 528, 527, 526 nm, respectively, and a core size of 2.63 nm.....87
- Figure 5.2.** Fluorescence spectra of CdSe-TOPO (■) and CdSe(ZnS)-TOPO (●) QDs excited at 373 nm with emission maxima at 545 and 553 nm, respectively. The QDs were monodispersed with FWHM of 30 and 46 nm, respectively. The addition of a ZnS shell to the CdSe core enhanced the optical properties by over tenfold.....89
- Figure 5.3.** Fluorescence spectra of CdSe(ZnS)-TOPO (■) compared to (A) CdSe(ZnS)-DHLLA (●) and (B) CdSe(ZnS)-MPS (▲) QDs excited at 373 nm with emission maxima at 543, 556 and 556 nm, respectively, and

	excitation/emission slit widths of 3 nm. The QDs were monodispersed with FWHM of 46, 38 and 38 nm, respectively.....	90
<b>Figure 5.4.</b>	TEM images of (A) CdSe-TOPO, (B) CdSe(ZnS)-TOPO, (C) CdSe(ZnS)-DHLA and (D) CdSe(ZnS)-MPS dispersions 50, 50, 50 and 100 nm scale bars, respectively. ....	91
<b>Figure 5.5.</b>	Surface pressure-area isotherm of 0.06 nmol CdSe-TOPO QDs spread on a pH 5.7, water subphase with a limiting molecular area of 13,500 Å <sup>2</sup> /particle.....	93
<b>Figure 5.6.</b>	Surface pressure-area isotherm of 0.06 nmol CdSe(ZnS)-TOPO QDs spread on a pH12 (■), 5.7 (●) and 2 (▲) subphase.....	95
<b>Figure 5.7.</b>	Surface pressure-area isotherm of 0.06 nmol CdSe(ZnS)-DHLA QDs spread on a pH 5.7, water subphase.....	97
<b>Figure 5.8.</b>	Surface pressure-area isotherm of 0.06 nmol CdSe(ZnS)-MPS QDs spread on a pH 12 (■) and 5.7 (●) subphase.....	98
<b>Chapter 6</b>		
<b>Figure 6.1.</b>	Schematic illustration of a Langmuir-Blodgett film deposition for an ideal amphiphillic molecule.....	103

## LIST OF TABLES

### Chapter 2

<b>Table 2.1.</b>	Reported $E^{1\%}$ values at absorbance values of 280 nm which can be used to calculate concentration for large molecular weight proteins.....	24
-------------------	--	----

### Chapter 4

<b>Table 4.1.</b>	Comparison of known Michaelis constants calculated from substrate interaction with $\beta$ -galactosidase. From comparison of other galactosides, X-gal with the lowest Michaelis constant correlates to it having the highest affinity for $\beta$ -galactosidase.....	67
<b>Table 4.2.</b>	IR band assignments using IRRAS at the air-water interface.....	78

## LIST OF SCHEMES

### Chapter 1

- Scheme 1.1.** Lactose hydrolysis by  $\beta$ -galactosidase via two processes where (1) the  $\beta$ -D-galactosyl linkage is enzymatically cleaved resulting in  $\beta$ -galactose and  $\alpha$ -glucose and (2) transglycosylation through the cleavage of the innate  $\beta$ 1-4 glycosidic bond of lactose internally returning through a  $\beta$ 1-6 bond with the previously cleaved glucose to form allolactose which is subsequently hydrolyzed to produce the monosaccharides.....6

### Chapter 2

- Scheme 2.1.** Dihydrolipoic acid synthesis by reduction of DL- $\alpha$ -lipoic acid with sodium borohydride followed by protonation under acidic conditions.....34

### Chapter 4

- Scheme 4.1.** Enzymatic  $\beta$ -D-galactosyl cleavage via hydrolysis of X-gal, a glycoside substrate, by  $\beta$ -galactosidase resulting in a blue solution.....65

## LIST OF ABBREVIATIONS

amide groups.....	N-H
carbonyl groups.....	C=O
charge of an electron.....	e
circular dichroism.....	CD
dihydrolipoic acid .....	DHLA
DHLA capped QDs.....	CdSe(ZnS)-DHLA
N,N-dimethylformamide.....	DMF
dioctadecyldimethylammonium bromide.....	DODAB
dipalmitoyl phosphatidyl choline.....	DPPC
1,2-distearoyl-sn-glycero-3-ethylphosphocholine chloride.....	DSPEC
1,2-distearoyl-sn-glycero-3-phosphate sodium.....	DSPA
effective mass of the electron in the solid.....	$m_e$
effective mass of the hole in the solid.....	$m_h$
energy gap of the quantum dot.....	$E_g(\text{QD})$
energy band gap of the bulk system.....	$E_g(\text{bulk})$
fluorescence resonance energy transfer.....	FRET
Fourier-transform infrared spectroscopy.....	FTIR
gaseous.....	G
human serum albumin.....	HSA
infrared absorption-reflection spectroscopy.....	IRRAS
in-plane bending mode.....	$\delta$
isoelectric point.....	pI



light emitting devices.....	LEDs
liquid-condensed.....	L-C
liquid-expanded.....	L-E
matrix-assisted laser desorption/ionization time of flight.....	MALDI-TOF
3-mercaptopropyltrimethoxysilane.....	MPS
MPS capped QDs.....	CdSe(ZnS)-MPS
o-nitrophenyl- $\beta$ -D-galactopyranoside.....	ONPG
permittivity of a vacuum.....	$\epsilon_0$
phenylalanine.....	Phe
quantum dots.....	QDs
radius of a quantum dot.....	R
radius of a sphere.....	r
reduced Planck's constant.....	$\hbar$
3,5-dimethoxy-4-hydroxy-cinnamic acid.....	sinapinic acid
stretching vibrations.....	$\nu$
surface pressure.....	$\pi$
surface pressure-area .....	$\pi$ -A
surface potential-area .....	$\Delta V$ -A
surface tension of the pure subphase.....	$\gamma_0$
surface tension of the monolayer covered subphase.....	$\gamma$
n-tetradecylphosphonic acid.....	TDPA
TOPO capped QDs.....	CdSe(ZnS)-TOPO
transmission electron microscopy.....	TEM

trioctylphosphine.....	TOP
trioctylphosphine oxide.....	TOPO
tryptophan.....	Trp
tyrosine.....	Tyr
5-bromo-4-chloro-3-indoyl- $\beta$ -D-galactopyranoside.....	X-gal

## Chapter 1

### Introduction

#### 1.1 The secondary structure of proteins

The function of proteins and enzymes in biological systems is based on their structure, particularly the secondary arrangement of hydrogen-bonding patterns of the peptide backbone. The secondary structure which is composed of amino acid sequences from the primary structure are commonly  $\alpha$ -helices and  $\beta$ -sheets with other types which are more rare as well as random coils defined as the lack of secondary structural motifs.

##### *$\alpha$ -helix*

The most common secondary structure, the  $\alpha$ -helix, is composed of amino acid residues in a coiled conformation with 3.6 residues per turn stabilized by hydrogen bonding throughout the backbone. Carbonyl (C=O) groups, along with amide (N-H) groups, make up the peptide backbone where hydrogen bonding between the carbonyl oxygen atoms and the hydrogen atoms from the amide group is the basis of the structural shape. Covalent attraction of the hydrogen to the nitrogen in the amine group is combined with the electrostatic interaction of the oxygen atom. This structure is further stabilized in the presence of water molecules through bonding different protein groups together by being a hydrogen bond acceptor and donor.<sup>1</sup> Separated by four residues, the repeating ( $i, i+4$ ) motif of bonding make this stable, right-handed helical structure dominant in amino acid structuralization as shown in Figure 1.1.

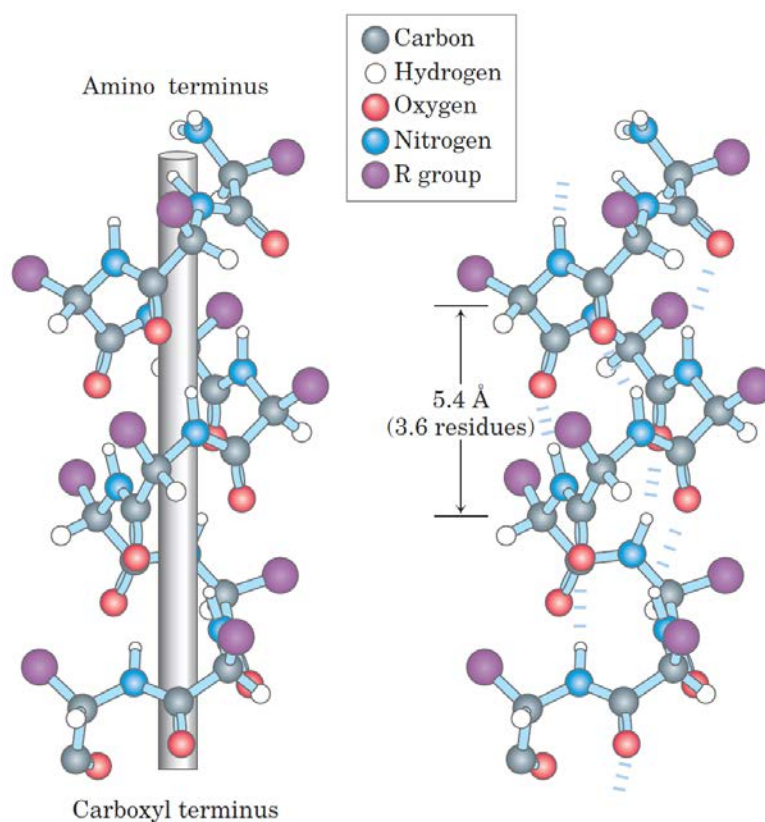


**Figure 1.1** The most common secondary structure, the  $\alpha$ -helix is a right-handed coil conformation stabilized by hydrogen bonding through the peptide backbone.<sup>1</sup>

### *$\beta$ -sheet*

Although less common than the  $\alpha$ -helix, the presence of hydrogen bonding in the second most common secondary structure,  $\beta$ -sheets, occurs laterally between the backbone which structures  $\beta$ -strands in an extended, sheet-like conformation as seen in Figure 1.2. This network of hydrogen bonding is established through a similar hydrogen bonding linkage as in  $\alpha$ -helices however between neighboring carbonyl and amide groups of adjacent  $\beta$ -strands. Two types of  $\beta$ -sheet conformation can occur which differ only by the relative direction of neighboring strands which can bond with adjacent N- to C-terminus in the same direction, parallel  $\beta$ -sheet, or in the opposite direction, anti-parallel  $\beta$ -sheet. The two orientations not only differ in structure but antiparallel provides a more

stable structure because of the planar hydrogen bonding between  $\beta$ -strands while parallel  $\beta$ -sheets hydrogen bond to be nonplanar.

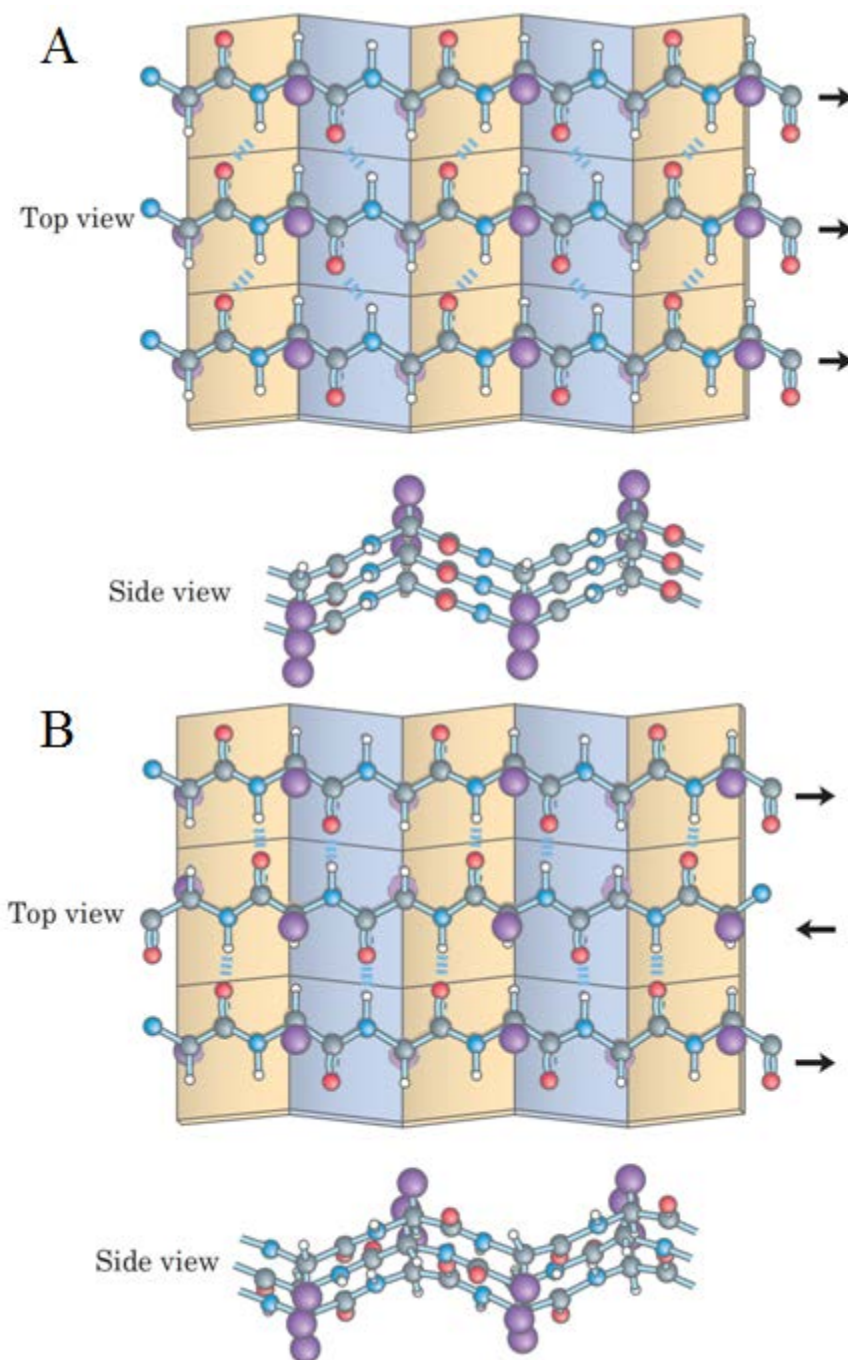


**Figure 1.2** The second most common secondary structure, the  $\beta$ -sheet conformation is also stabilized by hydrogen bonding and can be oriented in (A) parallel, continuous N- to C- terminus, arrangement or (B) anti-parallel, arranged with termini next to each other in opposite directions.<sup>1</sup>

$\beta$ -turns facilitate the connection of  $\beta$ -strands through a single residue where the peptide bond has been rotated 90 degrees relative to neighboring residues. A  $\beta$ -strand whether in the parallel or antiparallel conformation then continues the hydrogen bonding motif to continue the  $\beta$ -sheet.<sup>1</sup>

Specific conditions to maintain the structure of proteins and enzymes are therefore of particular interest when analyzing the stability from a physiochemical standpoint. If the function or activity of proteins and enzymes depends on a particular structure, manipulation of this structure by means of environmental change can reveal much through the molecular behavior.

## **1.2 Human serum albumin**

Human Serum Albumin (HSA) is an ideal protein for physical and chemical studies and has been extensively investigated due mainly to its biological importance.<sup>2-6</sup> HSA is involved in many physiological functions such as maintenance of pH and plasma oncotic pressure<sup>7,8</sup> and aside from these features, HSA is also renowned for its stability, abundance (50% of protein present in human blood plasma) and unique ligand binding properties.<sup>8-17</sup> The primary structure of HSA is composed of 585 amino acids (66,470 Da) in a single polypeptide chain with a heart-shaped three-dimensional structure that consists of three homologous domains as seen in Figure 1.3. The overall structure of HSA is 62%  $\alpha$ -helix<sup>18</sup> with nine loops held together by 17 disulfide bridges in a repeating pattern throughout these three domains starting from the amino terminus.

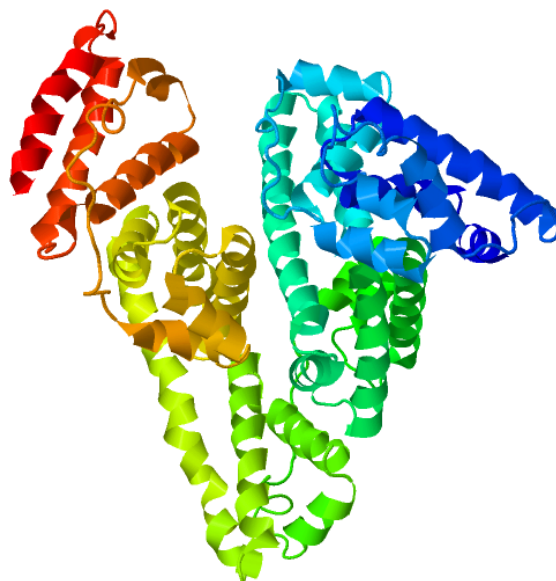


**Figure 1.3** Cartoon representation of human serum albumin showing the three domains which consist mostly of  $\alpha$ -helix (62%),  $\beta$ -sheet (5%) and random coils (33%).

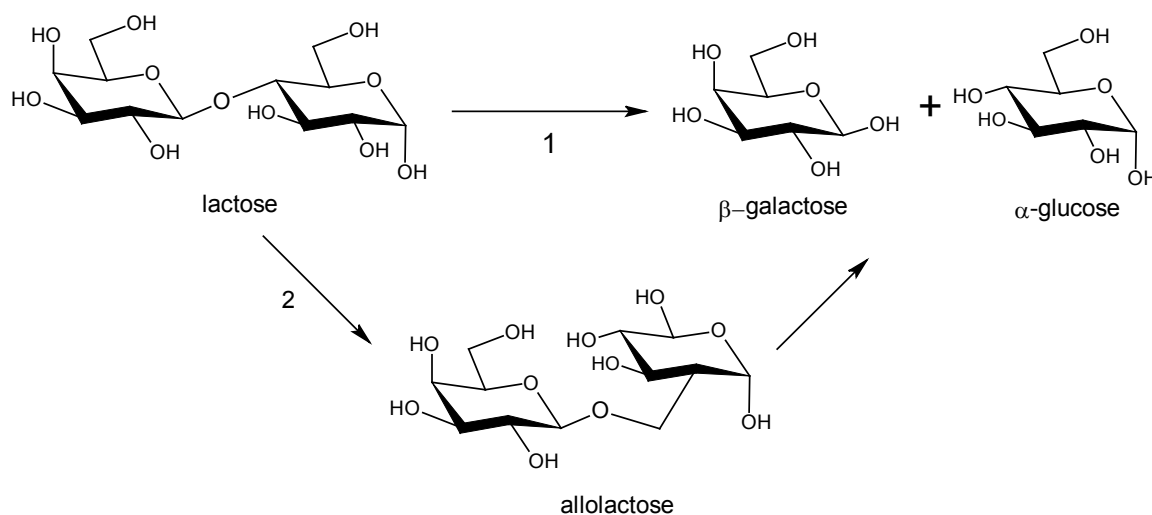
This specific protein has low amounts of tryptophan and methionine residues, an abundance of cysteine and charged amino acid residues such as aspartic and glutamic acid, lysine and arginine with acidic residues outnumbering the basic residues. At a neutral pH, the large number of ionized residues contained in HSA determine its overall net charge of -15 decreasing progressively from -9, -8 and +2 in domains I, II and III respectively resulting in an isoelectric point of  $\sim 4.8$ .<sup>7</sup>

### 1.3 $\beta$ -galactosidase

$\beta$ -galactosidase (E. coli 3.2.1.23) is an important family of hydrolase exoglycosidase enzymes. Its primary function is to cleave  $\beta$ -glycosidic bond formed between a galactose and organic substrate. To a lesser extent, this enzyme can also act on the arabinosidic and fucosidic bonds with other organic residues, such as amino acids, and it is an essential enzyme for the metabolism of both eukaryotic and prokaryotic cells. Besides fundamental interests in its role in metabolism,  $\beta$ -galactosidase is important tool in biochemistry, life

science research and industrial biotechnology. Its action on the X-gal substrate results in cleaving the glycosidic linkage to the indigo type dye, creating a strong indigo blue color which is a base reporting system for many EIA and ELISA assays as well as for histochemical staining. Finally, its large emerging applications are in the field of glycomics, where it is used extensively in sample preparation for glycan cleavage.<sup>19-22</sup>

Biologically,  $\beta$ -galactosidase is commonly referred to as essential for lactose digestion and studies have shown that the disaccharide can undergo two processes where 1.) the glycosidic bond in between the galactose and glucose moieties is cleaved by hydrolysis and 2.) transglycosylation which produces allolactose, a natural inducer of the lac operon, followed by hydrolysis into the two final monosaccharides detailed in Scheme 1.<sup>21,22</sup>



**Scheme 1.1 Lactose hydrolysis by  $\beta$ -galactosidase via two processes where (1) the  $\beta$ -D-galactosyl linkage is enzymatically cleaved resulting in  $\beta$ -galactose and  $\alpha$ -glucose and (2) transglycosylation through the cleavage of the innate  $\beta$ 1-4 glycosidic bond of lactose internally returning through a  $\beta$ 1-6 bond with the previously cleaved glucose to form allolactose which is subsequently hydrolyzed to produce the monosaccharides.**

Studies into the enzymatic active site through site-specific mutagenesis as well as labeling have demonstrated the roles of particular residues, especially Tyr-503, Glu-461,



Glu-537 and Met-502.<sup>23-28</sup> Many other properties such as the crystal structure<sup>19</sup> as well as the three-dimensional structure<sup>24</sup> have been used to develop an understanding of the substrate binding active site.  $\beta$ -galactosidase has been studied extensively to determine its molecular weight as a tetramer with a monomer composition of 1,023 amino acids weighing 116.3 kDa modeled with a isoelectric point of 4.6 in Figure 1.4.<sup>29-31</sup> The four identical subunits of the tetramer have a high content of amino acid residues, namely tryptophan, 39 residues, and tyrosine, 31 residues, compared to other biomolecules<sup>32</sup> which can be utilized to spectroscopically analyze this enzyme by observing their absorbance of UV-vis light as well as their fluorescence emission from excited-state energy levels.

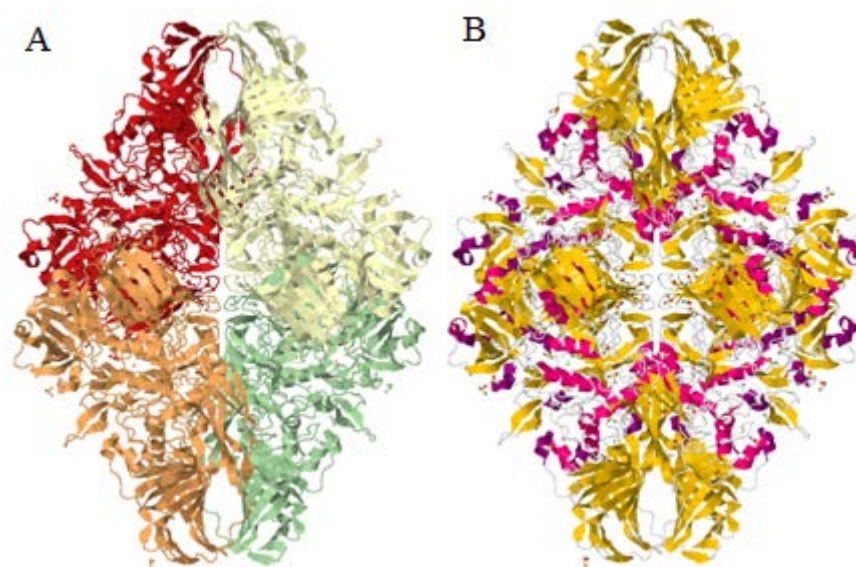


**Figure 1.4** Two cartoon representations of  $\beta$ -galactosidase which shows (A) the four monomers in different colors which complete the tetramer and (B) the secondary structures of the tetramer which is mostly comprised of  $\beta$ -sheets (40%) and  $\alpha$ -helices (35%) with random coils (12%) and  $\beta$ -turns (13%).

These two model proteins are not only biologically important but also ideal for experimentation as they contain a high number of polar, lipophilic groups that can make part of the molecule soluble in an aqueous subphase, Classically, surface pressure-area

isotherms are used to characterize interactions by observing difference from pure molecular isotherms. Compression-decompression cycles show stability of a homogenous monolayer and indicate if any hysteresis is occurring where the analyte is being lost to desorption into the subphase or if there are any formation of aggregates. Subphase variations include salts as well as pH changes which can be controlled through the Langmuir technique making it a versatile tool in characterizing molecular interactions.

#### **1.4 The Langmuir technique**

The Langmuir monolayer approach has been used extensively in the past to study proteins,<sup>33-36</sup> lipids,<sup>37</sup> enzymes,<sup>38</sup> and nanoparticles<sup>39,40</sup> as well as to understand their structural behavior with different environmental conditions<sup>41</sup> in two dimensions. This system has applications of simulating the biomembrane interface which correlates to observing molecules and their behavior at a hydrophobic-hydrophilic barrier as opposed to their behavior in bulk solution. As a model membrane system, Langmuir monolayers provide the best assessment of the chemical and physical behavior by observing analyte packing structure when surface pressure is applied as well as analyzing the intermolecular interactions while under these conditions. The Langmuir technique seeks to introduce the protein to a specific environment while changing the surroundings to suit the experimental parameters. These highly controllable experiments allow for specific selection of subphase content, pH as well as protein concentration. Among the advantages, an important parameter easily controlled is the surface pressure that is exerted by the monolayer. When simulating a biological membrane, higher surface pressures are required to accurately analyze the state of the analyte as it is compressed from an expanded phase with little intermolecular interaction to a condensed phase where

high amounts of van der Waals interactions and changes in orientation are observed.<sup>42,43</sup> Among many parameters, the Langmuir technique can be manipulated including the environmental conditions of the experiment, the spreading solvent, the purity of the analyte, the subphase, concentration, injection volume and the compression rate, much can be gleaned about the characteristics and behavior of analytes in a biological surrounding.<sup>44,45</sup> In this way characteristics and structure elucidation of membranes can be obtained and interactions can be facilitated to experimental objectives.

Surface pressure- ( $\pi$ -A) and surface potential-area ( $\Delta V$ -A) isotherms, classical methods for observing molecules at the air-subphase interface, provide information about the stability of a molecule at the interface as well as the molecular packing structure as the area of the molecules occupy is reduced through compression of the one-molecule-thick layer. Surface pressure-area isotherms are an ideal method of analyzing the compression of a monolayer formed by molecules as it reduces the surface tension of the subphase contained in a Langmuir trough system. Once a molecule is deposited at the air-subphase interface, immediate repulsion-expansion effects occur and the force energy per unit area of the subphase is lowered. As barriers skim the surface of the subphase, compressing the molecules closer together and reducing their orientation degrees of freedom, reorganization and reorientation stabilize the monolayer. The force per unit length is then represented as a positive difference between the surface tension of the subphase, which should not increase in surface pressure during compression, and the increase in surface tension of the monolayer until it collapses into multiple layers shown in Figure 1.5.<sup>46</sup>

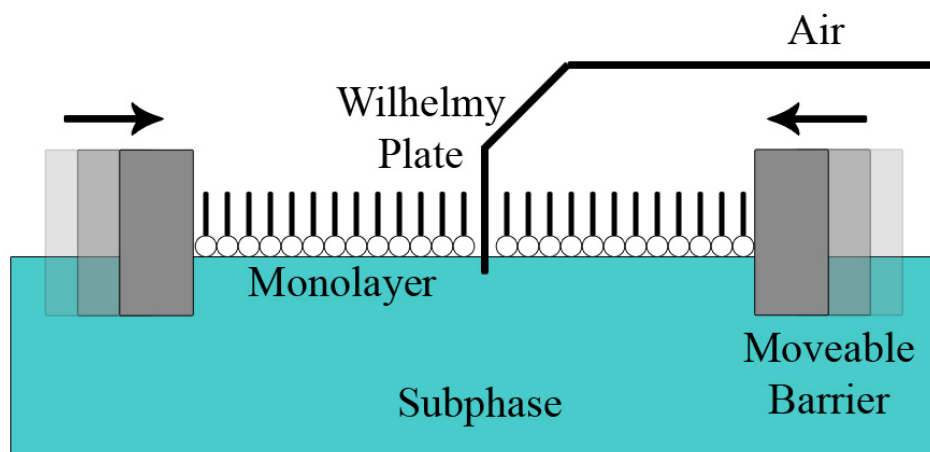


**Figure 1.5 Model representation of the compression of molecules at the air-subphase interface already highly ordered with minimal degrees of freedom due to the compression by the barriers. After this point in the monolayer, the molecules are exerting a large amount of surface pressure on the Wilhelmy plate and might collapse into multiple layers.**

Physical and electrostatic interactions are respectively examined by each technique as the monolayer transitions two-dimensional phases as the reorienting and reorganizing of the molecules at the interface. Extensions of the former technique include compression-decompression cycles and stability measurements which allow selective compression to surface pressures which can be held for long time periods or decompressed back to a state of little interaction among the molecules. Information about the aggregation or domain formation that these types of molecules might undergo or the extent of molecules expelled from the interface into the subphase can be gleaned from these experiments. The Langmuir technique is robust and reproducible and allows easy manipulation of experimental parameters to stretch the limits of any molecule while placing it in various surroundings.<sup>34</sup>

In addition to measurements involving surface pressure-, surface potential-area isotherms are performed which detail the difference in potential between the molecules at

the interface and a vibrating electrode. In conjunction, these two methods reveal the state of the molecules starting at points of zero interaction followed by compressing them to form a condensed film and finally a compact monolayer. The heterogeneity of the monolayer is described by comparing the two isotherms which shows at certain points of compression, the molecules exhibit a greater degree of electrostatic interaction between themselves and with the subphase. In this manner, this type of experimentation enables dipole interactions and van der Waals forces to therefore be detected.

In order to standardize and understand monolayers, a simpler molecule can be analyzed for its isotherm characteristics (Figure 1.6).<sup>34</sup> Uniform spreading and a sufficient waiting time-period<sup>47</sup> to allow stabilization are essential followed by compression of the molecules at the air-water interface resulting in certain phase changes as their degrees of freedom decrease as well as orientation changes.<sup>48,49</sup> Initially, as seen in Figure 1.6, as the molecules are spread at the interface, they are far apart and appear not to be interacting so much that they are referred to as being in a two-dimensional gaseous (G) phase. As the two-dimensional monolayer begins to form, the barriers move closer where a greater degree of interaction and consequently a restriction of orientation among the molecules occurs. The first of two phases is noted below a kink in the isotherm indicating a second-order phase transition (L-C1). Following this orthorhombic phase, a second condensed phase (L-C2) is noted by a sudden rise in surface pressure. The high surface pressure coupled with the proximity of the molecules reaches a maximum when the area around each molecule reaches a minimum followed by the monolayer collapsing on itself forming multiple layers.<sup>34,41</sup>

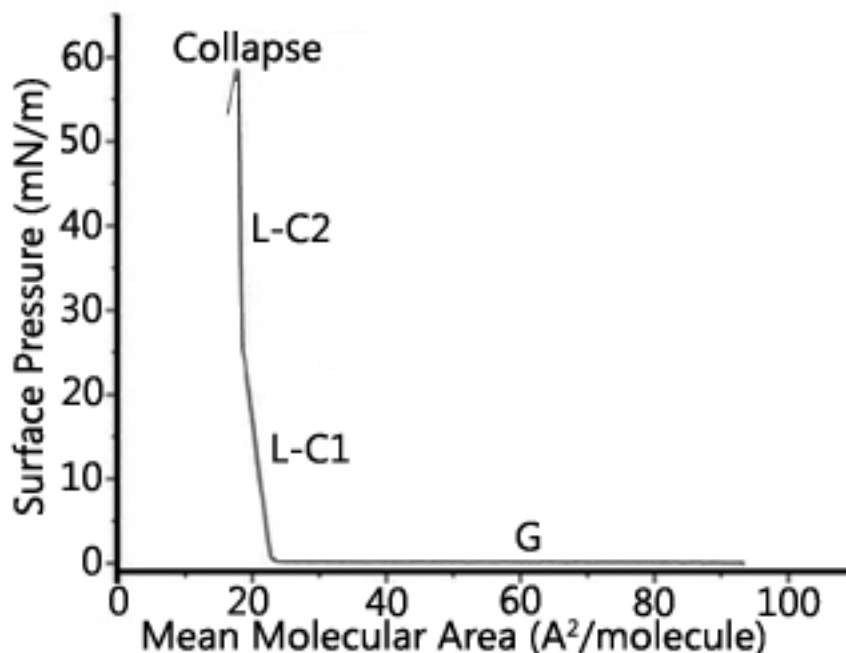


**Figure 1.6** Surface pressure-area isotherm of ideal amphiphilic molecules which shows a minimal degree of interaction upon compression at the air-subphase interface during the gaseous (G) phase. Hydrophobic molecular interactions are correlated with the rise in surface pressure as the molecules reorient themselves while in an initial liquid-expanded (L-C1) phase. Further compression of this liquid-condensed (L-C2) phase correlates to a sudden rise in surface pressure after a kink ending in the collapse of the monolayer into multiple layers.

## 1.5 Spectroscopy

### *UV-vis absorption and fluorescence spectroscopy*

In addition to the observable interactions, the Langmuir monolayer technique provides an environment ideal for observing the *in situ* photophysical properties of biomacromolecules as they undergo monolayer formation. Initially in aqueous solution, absorbance and fluorescence are commonly utilized to characterize these molecules based on particular amino acid contents. Tryptophan (Trp) is a common amino acid found in most proteins which is ideal not for its abundance but for its large molar absorption coefficient occurring from a  $\pi$  to  $\pi^*$  electronic transition and having absorption maxima at 220 nm,  $\epsilon = 3.6 \times 10^4 \text{ M}^{-1} \text{ cm}^{-1}$  and 280 nm,  $\epsilon = 5.5 \times 10^3 \text{ M}^{-1} \text{ cm}^{-1}$ . Between 200 and 300

nm, two other amino acids important for characterization due to their photophysical properties, tyrosine (Tyr) and phenylalanine (Phe), have much lower molar absorptivity at respective absorbance wavelengths. Tyrosine has absorption maxima at 222 nm,  $\epsilon = 9.0 \times 10^3 \text{ M}^{-1}\text{cm}^{-1}$  and 275 nm,  $\epsilon = 1.4 \times 10^3 \text{ M}^{-1}\text{cm}^{-1}$  while phenylalanine has absorption maxima at 205 nm,  $\epsilon = 9.6 \times 10^3 \text{ M}^{-1}\text{cm}^{-1}$  and 258 nm,  $\epsilon = 1.9 \times 10^2 \text{ M}^{-1}\text{cm}^{-1}$ .<sup>50,51</sup> In the aqueous phase the fluorescence emission maxima of these three spectroscopic probes is Phe = 282 nm, Tyr = 303 nm and Trp = 350 nm. Photophysical changes can be correlated with the  $\pi$ -A isotherm as the compression of the monolayer forces the molecules to undergo reorientation showing increases in absorbance and emission as the molecules' degrees of freedom at the interface are reduced.

### ***Circular Dichroism (CD)***

Along with the unique photophysical properties, conformational studies conducted via circular dichroism can detail changes in the secondary structure or enzymatic activity.<sup>52-54</sup> CD is commonly used in this manner to study the changes in protein conformation since characteristically,  $\beta$ -sheets have discernible bands in circular dichroism spectra between 190-260 nm which can be analyzed to determine content. Particularly at 220 nm a negative band is observed which can be attributed to  $n$ - $\pi^*$  transition whereas a positive band around 200 nm is due to  $\pi$ - $\pi^*$  transition. Further analysis of the  $\beta$ -sheet content shows that any changes in  $\beta$ -sheet length will increase the  $n$ - $\pi^*$  transition whereas an increase in width will produce stronger  $\pi$ - $\pi^*$  transitions.<sup>55-57</sup> The characteristics of  $\alpha$ -helix are apparent in the negative band at 222 nm due to the peptide  $n$ - $\pi^*$  transition and the  $\pi$ - $\pi^*$  transition producing a negative band at 208 nm and a positive band at 192 nm.

### ***Infrared Absorption-Reflection Spectroscopy (IRRAS)***

In conjunction with these measurements of average molecular area and surface potential, controlling the surface pressure as well as the surrounding subphase pH is utilized for conformational studies. The primary, secondary and tertiary structures of proteins and other biomacromolecules in aqueous solutions along with the extent of functional group conformation and position are gleaned from Fourier-transform infrared (FTIR) spectroscopy experiments. Once irradiated, certain molecular moieties will vibrate at characteristic wavenumbers allowing researchers to distinguish molecular structures.<sup>58</sup> Analyzed to determine  $\alpha$ -helix and  $\beta$ -sheet behavior, the amide I band (1700-1600  $\text{cm}^{-1}$ ) is mostly attributed to the stretching vibrations of C=O peptide bonds,  $\nu(\text{CO})$ , as well as in plane C-N bending mode,  $\delta(\text{CN})$ . Hydrogen bond strength is indirectly proportional in terms of carbonyl functional group vibrations throughout this band, therefore a greater degree of hydrogen bonding results in a lower electron density of the carbonyl group and subsequently a lower band absorption.<sup>58-60</sup> The amide II band (1600-1500  $\text{cm}^{-1}$ ) is also analyzed for secondary structure behavior which is characterized by 40% C-N stretching and 60% N-H bending.<sup>59</sup>

Information about orientation as well as conformation of protein and enzymes compressed at the air-water interface differs when compared to the bulk solution therefore it is of interest to observe these changes through interfacial experiments. Infrared absorption-reflection spectroscopy at the air-subphase interface with Langmuir monolayers allows for a controlled compression of the molecules while irradiating at specific surface pressures particular to the isotherm.<sup>61</sup> Determining the change in secondary structure of a molecule as it is compressed can be done by identifying the



bands which are associated with the  $\alpha$ -helix and  $\beta$ -sheets of the molecule. The  $\alpha$ -helix content in the amide I region absorbs between 1652 and 1657  $\text{cm}^{-1}$  <sup>59,60,62-65</sup> and  $\beta$ -sheet content which absorbs in the 1620-1645  $\text{cm}^{-1}$  region.<sup>66</sup> The versatility of manipulating the environmental conditions allows researchers to see at the air-water interface how the molecule will react when introduced to salt conditions as well as pH changes.

### **1.6 Semiconductor Quantum Dots (QD)**

The Langmuir monolayer technique allows for an investigation into the interactions between many analytes, organic and inorganic, including quantum dots. Not only does it allow two-dimensional interaction on a controlled environment but any further interactions between quantum dots and a range of other analytes is possible through the many known molecular areas of those contained in natural membranes.<sup>67-71</sup> This technique allows for the simulation of higher surface pressures common to those found in model biological membranes while avoiding phase changes which can randomly occur in the bulk hydrated dispersions.<sup>42,43</sup> Recent work in quantum dot synthesis and narrow size distribution has given rise to the possibility of biological applications which lends interest to how these particle will interact at a cellular membrane. Self-aggregation<sup>72,73</sup> luminescence,<sup>74-76</sup> and protein interaction with quantum dots<sup>77</sup> currently have been studied briefly regarding the surface chemistry at biological interfaces.

Quantum dots are compound semiconductors commonly formed from groups II and VI on the periodic table, namely (CdS, CdSe, and CdTe), in the size range of 1~12 nm. These have attracted great interest in both fundamental research and as building blocks for photonic, electronic and magnetic devices.<sup>78-80</sup> A variety of advantages which these nanoparticles innately possess such as tunable size-dependent emission with high

photoluminescence quantum yields, broad excitation spectra and narrow emission bandwidths show the potential of QDs in the field of nanotechnology. Construction of highly order QDs has already led to applications such as thin-film light emitting devices (LEDs)<sup>81</sup> and biological labels<sup>82</sup> therefore a better understanding of their behavior is still the focus of scientific research.

The three main categories of materials which possess electrical properties can be organized into conductors, semiconductors and insulators.<sup>83</sup> In the field of photophysical chemistry it is important to understand how researchers can use the basic principles of chemistry to produce nanomaterials such as quantum dots utilized for these innate properties. From a basic point of view regarding quantum dots, when an electric field is applied to such materials, the electrons will move through the materials based on the availability of empty states in the band which comprises the outer shell for electrons to occupy. This movement however is limited by the neighboring or receiving atom which must have a vacant state of similar energy for the electron to flow to which is common in solid materials. By viewing a solid in terms of molecular orbitals, one can see that the bonding of many atoms produces bonding and anti-bonding orbitals of similar energy for these electrons to flow between also referred to as energy bands. While the energy levels might be slightly different, their similarity in terms of energy is enough for electrons to move freely to the vacant states in these orbitals with the highest occupied orbital referred to as the valence band and the next available but unoccupied region referred to as the conduction band. The difference between the three main categories is found in this gap ( $E_g$ ) between the valence band and conduction band where pure metals and alloys have partially or fully unoccupied energy levels which easily promotes the flow of electrons,

shown in Figure 1.7. Insulators and semiconductors on the other hand have a fully occupied valence band as well as larger distances between these energy levels which at room temperature does not allow for conduction of electrons to occur when a voltage is applied. Insulators therefore do not conduct electricity because there are no vacant levels on neighboring atoms of similar energy while semiconductors require increases of temperature to promote electrons across the band gap to the conduction band which are then able to conduct electricity.

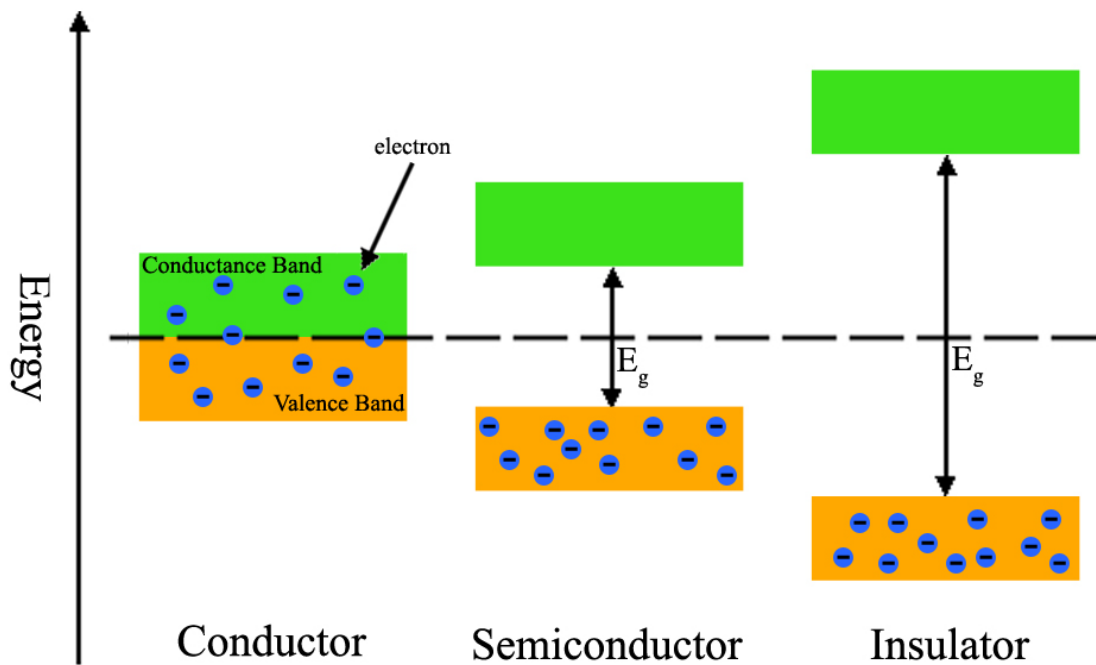


**Figure 1.7** At low temperatures, the three types of materials can be simplified in understanding their propensity to allow the flow of electrons when an electric field is applied. The boxes show that metals have a small band gap,  $E_g$ , and their lower valence shell is not completely full allowing electrons to move freely into the upper conductance band. Semiconductors and insulator on the other hand have completely filled valence bands and different sized band gaps giving them particular properties.

As previously discussed, quantum dots have nanometers sized diameters and are composed of specifically elements in two main groups of the periodic table, II and VI. These groups are chosen for purposes of doping to produce n-type semiconductors where the doping element, Se, has at least two more valence electrons than the host semiconductor, Cd. This extra electron is able to carry a current across the band gap as a voltage is applied. The size dependence is a very important concept due to the quantum mechanical implications when considering what occurs when irradiating with light at intense energy levels over that of the band gap energy. An electron will be promoted from the fully occupied valence band to the unoccupied conductance band thereby leaving behind a hole. Thought of now as an individual particle, the spatial separation between the electron and this now positively charged hole can be calculated:

$$r = \frac{\epsilon \hbar^2}{\pi m_r e^2} \quad (1.1)$$

Using a modification of the Bohr model, the separation of the electron-hole pair can be defined in three dimensions as the radius of a sphere,  $r$ . That radius is dependent on the dielectric constant of the semiconductor,  $\epsilon$ , the reduced mass of the electron-hole pair,  $m_r$ , as well as other constants. The calculations for most semiconductors confines the separation to be under between 1-10 nm which is ideal for explaining the semiconductor phenomenon by the particle in a box model which allows for observation and the quantization of energy levels. The model defines the energy gap as being correlated with the size of the nanoparticle:<sup>84,85</sup>

$$E_g(QD) = E_g(bulk) + \frac{\hbar^2}{8R^2} \left( \frac{1}{m_e} + \frac{1}{m_h} \right) - \frac{1.8e^2}{4\pi\epsilon_0\epsilon R} \quad (1.2)$$

The energy gap of the system in terms of the quantum dot radius,  $R$  says that the energy gap of the quantum dot,  $E_g(\text{QD})$ , will increase with a decrease in particle size. Other factors include the energy band gap of the bulk system,  $E_g(\text{bulk})$ , the dielectric constant of the solid,  $\epsilon$ , the effective mass of the electron in the solid,  $m_e$ , the effective mass of the hole in the solid,  $m_h$ , as well as constants including the reduced Planck's constant,  $\hbar$ , the charge of an electron,  $e$ , and the permittivity of a vacuum,  $\epsilon_0$ . Several rules for the model are assumed such as uniformity of the quantum dot inside and outside as well as the discussed electron-hole pair is always found inside the system.

## 1.7 Summary

This work was aimed to study biomacromolecules and highly fluorescent quantum dots by using the Langmuir monolayer techniques and spectroscopy. The novelty of the Langmuir technique approach is to investigate the physicochemical and photophysical properties *in situ* in comparison to the bulk solution as analyzed by classical spectroscopy. This dissertation is divided into six chapters which discusses the progress of understanding of how to use the Langmuir technique to observe the interfacial behavior of human serum albumin and  $\beta$ -galactosidase. Followed by a synthetic route to exchange ligands on quantum dots to alter their properties in solution, this work in the future can be coupled with conjugation with macromolecules like the ones discussed to create fluorescence probes and biosensors.

Chapter one introduces the Langmuir technique and discusses the biological importance of the proteins studied in this dissertation. As model proteins, HSA has been used in numerous studies for its robust nature and abundance in biological systems as well as  $\beta$ -galactosidase for its importance in galactoside hydrolysis. A brief introduction to the

Langmuir methodology and the various spectroscopic techniques which accompany and support various findings is discussed followed by the theory of quantum dots and their unique size dependent nature.

Chapter two goes more into detail of the theory of the instrumentation and technique used, especially the synthetic routes used in the production and modification of quantum dots. All procedural methodology mentioned in this section is supported by experimental evidence and interpretation in the following chapters.

Chapter three shows the experimental results from HSA first spectroscopically to understand its photophysical properties provided by the single tryptophan residue in the molecule followed by the Langmuir monolayer technique. Measurements of subphase salt concentration with surface pressure- and surface potential-area isotherms and the effect of the pure protein packing structure are analyzed throughout in this manuscript. *In situ* absorbance and fluorescence are correlated with the phase change of the isotherm throughout compression as well as observation of temperature induced aggregate formation by changes in the absorption spectra of the protein at the air-water interface.

Chapter four reports in full the spectroscopic properties of  $\beta$ -galactosidase in an aqueous solution over a series of experiments utilizing UV-vis absorption to determine concentration, circular dichroism to understand the conformational changes occurring with changes in the pH of the aqueous environment as well as fluorescence spectroscopy to observe the emission quenching over time. Substrate studies were conducted to determine the Michaelis constant for X-gal, a glycoside like lactose, as it is hydrolyzed at different rates by changing the substrate concentration interacting with  $\beta$ -galactosidase. The Langmuir monolayer technique has been implemented to analyze the surface

chemistry and *in situ* spectroscopy of  $\beta$ -galactosidase during monolayer compression. Experimentation of the stability and conformational studies has revealed the influence of pH on the nature of the enzyme while at the air-water interface.

Chapter five includes the synthesis of quantum dots analyzed by UV-vis and fluorescence spectroscopy while in solution. Starting with the core CdSe followed by addition of a photophysically stabilizing shell, CdSe(ZnS)-TOPO the experimental properties of these QDs with different hydrophilic and hydrophobic ligands are analyzed. Controlling the interparticle distance is investigated by exchange a known sized ligand which is then measured at the air-water interface.

Chapter six discusses the future work involving  $\beta$ -galactosidase and substrate studies by Langmuir-Blodgett technique.

## Chapter 2

### Experimental

#### 2.1 Materials

Human serum albumin was obtained from MP Biomedicals (Solon, OH) with molecular weight of 66,500 Da. Sodium chloride was purchased from Sigma Aldrich (St. Louis, MO) with purity higher than 99.5%.  $\beta$ -galactosidase (Lot: M7538) was also obtained from MP Biomedical (Solon, OH) with a monomer molecular weight of 116,646 Da as determined by Matrix-Assisted Laser Desorption/Ionization Time of Flight. The specific activity of the enzyme (735 units/mg dry weight) was provided by the company by analysis with o-nitrophenyl- $\beta$ -D-galactopyranoside (ONPG) which defines one unit of the enzyme which hydrolyzes 1  $\mu$ mole of the substrate per minute at 25°C, pH 7.5.<sup>86</sup> Hydrochloric acid, sodium chloride with a purity higher than 99.5%, D-lactose anhydrous and X-gal (5-bromo-4-chloro-3-indoyl- $\beta$ -D-galactopyranoside) were also obtained from MP Biomedical. Sodium hydroxide used for adjusting pH were obtained from Pharmco (Brookfield, CT). Precursor chemicals to core quantum dot synthesis such as trioctylphosphine (TOP) with a purity of 97%, trioctylphosphine oxide (TOPO) also with a high purity of above 99%, and n-tetradecylphosphonic acid (TDPA) were obtained from Strem Chemicals (Newburyport, MA). Other core precursors such as cadmium oxide (CdO), selenium (Se) and tetramethylammonium hydroxide (TMAOH) were from MP Biomedicals. Shell components such as diethylzinc with a minimum purity of 95% contained by 10 wt% in hexane and bis(trimethylsilyl) sulfide were obtained by Strem Chemicals and TCI America, respectively. DL- $\alpha$ -lipoic acid, sodium borohydride, magnesium sulfate anhydrous used in the synthesis of dihydrolipoic acid (DHLLA) were



obtained from MP Biomedicals as well as all organic solvents such as methanol and chloroform. All chemicals were used without any further purification. Water utilized in these experiments was obtained from a Modulab 2020 Water purification system (Continental Water System Corp., San Antonio, TX) with resistivity of 18 M $\Omega$ ·cm, surface tension of 71.6 mN/m, and pH 5.7 at 20.0  $\pm$  0.5°C. For experiments requiring pH exact solutions, a Lab 850 (Schott Instruments, Mainz, Germany) equipped with Blueline 15 pH electrode kept in a 3 M KCl solution and calibrated with a SI Analytics GmbH buffer set was used.

## **2.2 Methods for spectroscopy and surface chemistry**

In this section it is necessary to discuss aqueous solution spectroscopy before understanding the principles of surface chemistry using the Langmuir technique.

### **2.2.1 Spectroscopy**

#### ***Absorption***

UV-vis spectroscopy classically relates absorbance to concentration using Beer's Law:<sup>87</sup>

$$A = \varepsilon \cdot l \cdot c \quad (2.1)$$

in which absorbance,  $A$ , is a function of the molar extinction coefficient of the sample,  $\varepsilon$ , the path length of the optical cell where the light travels through the sample,  $l$ , and the molar concentration of the analyte solubilized in solution,  $c$ . Proteins, however, due to their high molecular weight and high molar extinction coefficient are often analyzed by relating concentration to an  $E^{1\%}$  value. The molar extinction coefficient requires analysis of the absorbance of a 1 M solution whereas the  $E^{1\%}$  utilizes a 1% w/v solution for absorbance analysis. Assuming a 1 cm optical path length, Beer's Law simplifies to:

$$A = \varepsilon \cdot c \quad (2.2)$$

Multiplying both sides by a factor of ten and separating out the concentration to include the molecular weight and a weight by volume variable Beer's Law can be divided into two distinct calculations with  $E^{1\%}$ .

$$Absorbance \cdot 10 = \varepsilon \cdot 10 \cdot \left( \frac{1}{Molecular\ Weight_{g/mole}} \cdot Concentration_{g/L} \right) \quad (2.3)$$

Once the absorbance of a sample with unknown concentration is measured, a reported  $E^{1\%}$  value see in Table 2.1 can be used to convert back to the molar extinction coefficient or concentration of the sample, while assuming the optical path length to always be 1 cm:

$$\frac{Absorbance \cdot 10}{Concentration_{g/L}} = \frac{\varepsilon \cdot 10}{Molecular\ Weight_{g/mole}} \quad (2.4)$$

$$E^{1\%} = \frac{\varepsilon \cdot 10}{Molecular\ Weight_{g/mole}} \quad (2.5)$$

$$\varepsilon = \frac{E^{1\%} \cdot Molecular\ Weight_{g/mole}}{10} \quad (2.6)$$

$$E^{1\%} = \frac{Absorbance \cdot 10}{Concentration_{g/L}} \quad (2.7)$$

$$Concentration_{g/L} = \frac{Absorbance \cdot 10}{E^{1\%}} \quad (2.8)$$

**Table 2.1 Reported  $E^{1\%}$  values at absorbance values of 280 nm which can be used to calculate concentration for large molecular weight proteins.**

Protein	$E^{1\%}$
Human Serum Albumin <sup>88</sup>	5.31
$\beta$ -galactosidase <sup>89</sup>	20.9

UV-vis spectra taken of the aqueous solutions were measured by a Shimadzu UV2600 spectrophotometer (Shimadzu Scientific Instruments, Columbia, MD) recording spectra between 200 and 800 nm using a 1 cm optical path length quartz cell.

### ***Fluorescence***

Fluorescence spectra were obtained with a Fluorolog-3 spectrofluorometer (Horiba Scientific, Edison, NJ) using a 1 cm optical path length quartz cell with a slit width of 3 nm for both the excitation and emission. Fluorescence spectroscopy utilizes the ability of molecules to absorb UV-vis light energy as photons which then measure the transition of these molecules from the ground electron state to an excited electron state and back to the ground state. Through this type of spectroscopy the behavior of specific moieties of proteins and enzymes can be correlated to wavelengths of light.

In aqueous solutions, excitation of the analyte from the ground electronic state to one of many vibrational excited electronic state begins by absorbing a photon. This excitation wavelength is specific to amino acids like tryptophan but it must be equivalent to the difference in energy between the ground and excited state. Energy is lost by non-radiative processes until the species, from the lowest vibrational excited state, emits a photon in the form of fluorescence when the electron returns back to the ground electronic state. The vibrational ground state which the species returns to correlates to different energies which can be interpreted as frequencies of emitted light also known as the emission wavelength.<sup>90</sup>

Important for the detection of fluorescence from excited energy states, the excitation light and emission light pass through a monochromator necessary to only transmit light which is near the specified wavelengths. Adjustable slit widths of filters help to control

the magnitude and resolution of the transmitted light and once the sample is excited, fluorescence emission is detected at a  $90^\circ$  angle to selectively detect emission and not incident light shown in the model setup in Figure 2.1.

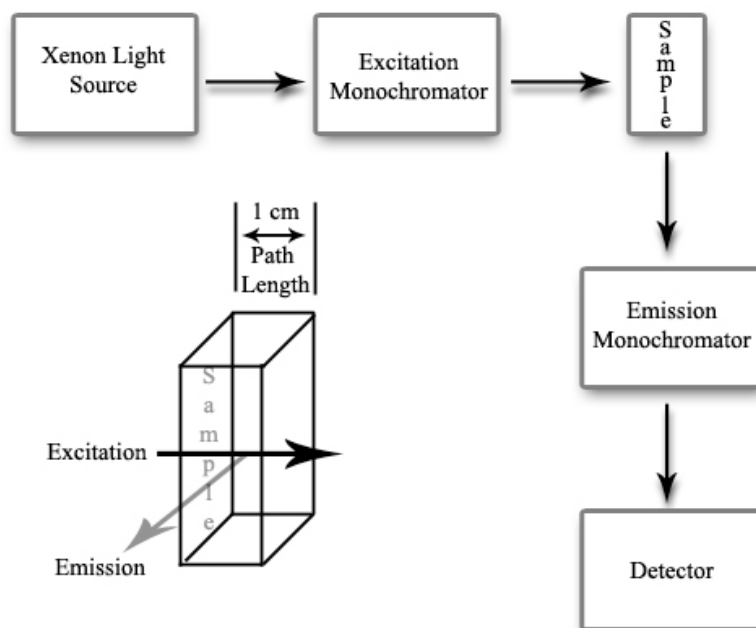


**Figure 2.1 Model of sample excitation and fluorescence emission detection setup with a view of the 1 cm optical path length quartz cuvette.**

### ***Circular Dichroism***

Useful for studying the secondary structure of proteins, circular dichroism is measured as the difference in absorption of left-handed polarized versus right-handed polarized light which arise due to structural asymmetry.<sup>91,92</sup> Circular dichroism is used to observe the  $\alpha$ -helix content with characteristic negative peaks at 209 and 222 nm as well as one positive peak at 192 nm as seen in Figure 2.2. The  $\beta$ -sheet can also be calculated from these spectra which has a negative band at 218 nm and a positive band at 195 nm. Unordered segments of proteins and enzymes have a negative band around 198 nm. CD spectra were measured using a JASCO J-815 spectropolarimeter flushed with nitrogen gas with a 150-watt xenon lamp using a quartz cell of 0.2 cm optical path length. Spectra

over a 30 min time period were recorded between wavelengths of 190 and 260 nm, the far-UV region, with a response time of 2 s, a band width of 1 nm and a continuous scanning speed of 100 nm/min. The 35 raw data spectra were averaged then smoothed using adjacent-averaging of 100 points and finally processed for  $\alpha$ -helix and  $\beta$ -sheet content using DICROWEB software with an analysis program of CONTINLL and a reference set of SP175.<sup>57,93,94</sup>

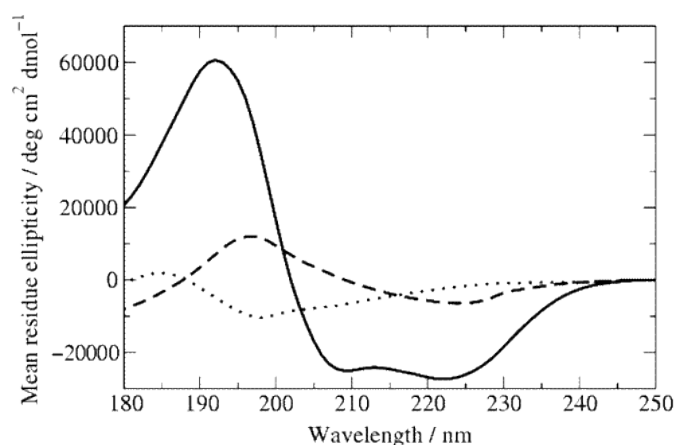


**Figure 2.2 Circular dichroism spectra of proteins which with representative secondary structures showing  $\alpha$ -helix (solid line),  $\beta$ -sheet (dashed line) and unordered (dotted line) conformation.<sup>91</sup>**

### *Mass Spectrometry*

A mass spectrometry sample analyzed using Matrix-Assisted Laser Desorption/Ionization Time of Flight mass spectrometer (Biflex IV, Bruker Daltonics, Germany) equipped with a standard nitrogen laser (337 nm). The sample was applied to a stainless steel SCOUT 384 MALDI target and dried. Sinapinic acid (3,5-dimethoxy-4-hydroxy-cinnamic acid) is used to calibrate the instrument and the spectra obtained with a minimum of 200 laser shots was processed with Bruker XMASS software after applying a Savitzky-Golay smoothing filter set at 100 adjacent points.

### ***Transmission Electron Microscopy (TEM)***

TEM analyses were performed using a JEOL 1400x TEM operated at 100 kV to collect digital images using a Gatan Camera at several magnifications. Each TEM sample was prepared by placing a drop of the sample solution on a Formvar and carbon coated 200 mesh copper grid and allowed to air dry. The samples were then analyzed under microscope and images were taken.

### **2.2.2 Surface Chemistry**

Langmuir isotherms and *in situ* UV-vis absorption and fluorescence spectroscopy were conducted in a clean room (class 1000) with constant temperature of  $20.0 \pm 0.5^\circ\text{C}$  and humidity of  $50 \pm 1\%$ . A Kibron  $\mu$ -trough (Kibron Inc., Helsinki, Finland) with an area of 5.9 cm x 21.1 cm was utilized for the surface pressure- and surface potential-area isotherms, compression-decompression cycles, and stability studies. UV-vis absorption implemented at the air-subphase interface of the Langmuir monolayers were obtained with a Hewlett-Packard (HP) 8452A spectrophotometer. Fluorescence spectra for Langmuir monolayers were measured with an optical fiber detector connected to a Fluorolog-3 spectrofluorometer (Horiba Scientific, Edison, NJ) and excitation/emission both had slit widths set to 3 nm. Both UV-vis absorption and fluorescence spectra were collected on the top of a KSV trough (KSV Instrument Ltd., Helsinki, Finland), which has an area of 7.5 cm x 30 cm and a quartz window located in the center of the Teflon trough.

### ***Surface pressure-area isotherms***

Surface pressure-area isotherms measure the change in surface tension of a pure subphase when covered with a monolayer. Common for this type of analysis, the

Wilhelmy method utilizes with a 0.51 mm diameter alloy wire probe with a sensitivity of  $\pm 0.01$  mN/m by dipping it into subphase with zero contact angle. Calibration of this method with a standard compound, usually stearic acid, allows the detector determine this change in surface pressure-area of a known compound expressed in units of mN/m. After spreading analyte on the subphase, simultaneous repulsion and expansion forces which keep the analyte at the interface lower the force energy per unit area of the subphase. Compression of the molecules at the interface by two symmetrical barriers brings the molecules closer together which forces them to reorganize and reorient to maximize hydrophilic and hydrophobic interactions with the aqueous subphase and air, respectively. Stabilization of the monolayer is recorded as the positive change in surface tension of the pure subphase ( $\gamma_0$ ) and the monolayer covered subphase ( $\gamma$ ) which defines the surface pressure ( $\pi$ ).<sup>41</sup>

$$\pi = \gamma_0 - \gamma \quad (2.9)$$

### ***Surface potential-area isotherm***

The physicochemical properties studied by analysis of surface pressure include the kinetic energy of the analyte which comprises the monolayer as well as the physical and electrostatic interactions occurring between different regions of amphiphilic molecules. Coupled with the surface pressure, surface potential-area isotherms detail the electrostatic interactions occurring at greater distances (factor of  $R^{-2}$ ) compared to hydrophobic interactions (factor of  $R^{-6}$ ). Measured as the difference in potential between the molecules at the interface and a vibrating electrode, the surface potential-area isotherm is sensitive to the change in potential created by the spreading of an analyte monolayer. When

spread, the potential at the phase boundary between the surface of the liquid and a vibrating electrode, can be measured to observe minute interactions.

The surface potential was measured with a Kelvin probe consisting of a capacitor-like system. The vibrating plate was set at  $\sim 1$  mm above the surface of the Langmuir monolayer and a gold-plated trough acted as a counter electrode. By this method, the change in capacity of the small gap between the interface and the electrode varies, which is detected as a potential change. Expressed as the potential difference,  $\Delta V$ , separated by a distance,  $d$  and enclosing a charge density,  $\sigma$ , an important factor contributes to the surface potential, the dielectric constant,  $\epsilon$ .

$$\Delta V = \frac{4\pi\sigma d}{\epsilon} \quad (2.10)$$

The dielectric constant is a function of the dipoles from the monolayer spread at the air-subphase interface. Commonly expressed as a function of molecular area, the surface potential is measured in millivolts.<sup>41</sup>

### ***Infrared reflection-absorption spectroscopy***

IRRAS measurements were conducted at the air-subphase interface under various conditions using the EQUINOX 55 FTIR spectrometer (Bruker Optics, Billerica, MA) equipped with an XA-511 external reflection accessory. The IR beam irradiated the molecules at the interface during compression of the Langmuir monolayer which was then reflected to a liquid nitrogen cooled HgCdTe (MCT) detector. Monolayer compression was stopped at desired surface pressures in order to obtain spectra with a resolution of  $8 \text{ cm}^{-1}$  by co-addition of 1200 scans.

The correlation between secondary structure and infrared light is done by reflecting IR light off of a well spread Langmuir monolayer system. Measured as the intensity of



reflected radiation as a function of wavelength,<sup>95</sup> the data is plotted as the log ratio of the reflectivity of the background subphase and the reflectivity of the monolayer vs wavenumber. IRRAS can have positive and negative bands primarily depending on the Brewster angle of water compared to the angle of incident light as well as the polarization of incident light. The two polarizations of light used to study the Langmuir monolayer differ by the electric vector oscillates in the plane of incidence and perpendicular to that plane for p-polarization and s-polarization light, respectively.

### **2.3 Preparation of solution for Langmuir technique**

#### ***Langmuir monolayer preparation***

Human serum albumin, received as a dry powder, was stored at -4°C and all solutions were obtained by dissolving HSA in pure water, pH 5.7, obtained on a daily basis from the Modulab 2020. Langmuir monolayers were obtained with bulk HSA solutions of 0.1 mg/mL (1.5  $\mu$ M) unless otherwise noted in the text. Reproducible monolayers were obtained on a 0.01 M sodium chloride subphase and the spreading 0.15 nmol of the protein. At the air-subphase interface, deposition of the protein in solution was conducted by placing droplets of equal size on the surface of the subphase using a 100  $\mu$ L syringe (Hamilton Co., Reno, Nevada). Experiments were then continued after a waiting-time period of 15 min in order to allow the HSA monolayer to reach equilibrium.

$\beta$ -galactosidase was diluted to a concentration of 0.2 mg/mL and confirmed by subsequent analysis via UV-vis absorption. The accuracy of the concentration was dependent on the dilution factors from the initial dry powder which was then confirmed by utilizing the reported  $E^{1\%}$  (20.9) of the enzyme. All solution work involving changes to the aqueous pH environment and substrate studies was done with a dilution factor of

ten in terms of enzyme concentration as confirmed by the above mentioned method. UV-vis absorption analysis was conducted at the maximum absorption of tryptophan ( $\lambda_{\max} = 282$  nm) and fluorescence spectroscopy was conducted with an excitation wavelength of  $\lambda_{\text{exc}} = 284$  nm with both excitation and emission slit widths of 3 nm and comparative analysis was prepared using the  $\beta$ -galactosidase emission maximum wavelength at  $\lambda_{\text{em}} = 354$  nm. Reproducible monolayers were obtained on a sodium chloride subphase (0.1 M) and the spreading volume of the enzyme was 65  $\mu\text{L}$  while using the Kibron instrument and 150  $\mu\text{L}$  while using the KSV instrument. At the air-subphase interface, deposition of the enzyme in solution was conducted by placing droplets of equal size on the surface of the subphase using a 100  $\mu\text{L}$  syringe (Hamilton Co., Reno, Nevada). Experiments were then continued after a waiting time period of 15 min in order to allow the  $\beta$ -galactosidase monolayer to reach equilibrium at a compression rate of  $6,086 \text{ \AA}^2 \text{ molecule}^{-1} \text{ min}^{-1}$ .

X-gal solutions were prepared by solubilizing X-gal in a minimal amount of a polar, hydrophilic, aprotic solvent, N,N-dimethylformamide (DMF), which is considerably polar for solubilizing the substrate while not hydrolyzing the glycosidic linkage. 1xPBS buffer (pH 7.2) was prepared with NaCl (13.7 mM), KCl (2.7 mM),  $\text{Na}_2\text{HPO}_4$  (10 mM),  $\text{KH}_2\text{PO}_4$  (2 mM). Substrate concentration was brought to 1.0 mg/mL in the 1xPBS solution in a flask also containing  $\text{MgCl}_2$  (2 mM),  $\text{K}_3\text{Fe}(\text{CN})_6$  (5 mM) and  $\text{K}_4\text{Fe}(\text{CN})_6$  (5 mM) (Sigma Aldrich, St. Louis, MO).

### ***In situ protein fibrillation***

While at the air-subphase interface, fibrillation of HSA was induced by forming a Langmuir monolayer and keeping the surface pressure constant while heating the KSV trough. On a subphase of pH 5.7, 0.01 M NaCl, 45  $\mu\text{L}$  of 0.5 mg/mL HSA solution was

spread and after a 15 min waiting-time period, the monolayer was compressed to a surface pressure of 10 mN/m. A circulating flow of water at 37°C was utilized to heat beneath the KSV trough to keep the subphase temperature constant. Laser light was reflected off the subphase covered trough outside of the partially compressed barriers in order to measure any evaporation of subphase. Evaporation was countered by slow addition of pH 5.7 pure water as to not change the subphase salt concentration or disturb the monolayer. *In situ* UV-vis absorption measurements were taken at one hour time intervals and analyzed at a  $\lambda_{\text{max}} = 278$  nm.

## 2.4 Synthesis of QDs and Conjugates

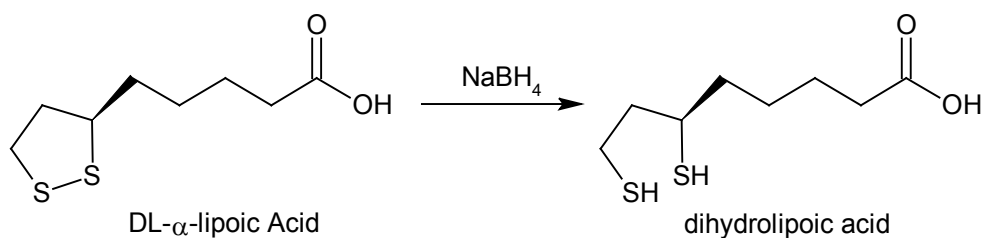
### *Synthesis of CdSe(ZnS) Core(Shell) QDs*

(CdSe)ZnS core-shell nanoparticles were synthesized in trioctylphosphine oxide following standard procedures described in literature.<sup>96</sup> Starting with the synthesis of CdSe core, a three-necked round bottom flask containing 54 mg of CdO, 223 mg of TDPA, and 3.77 g of TOPO were reacted under Ar protection. Utilizing the hot injection method, a solution of selenium power (41 mg) in 2.0 mL of trioctylphosphine was added when the temperature of the solution was a consistent 270°C. A nucleation time of 10 min was immediately quenched by submerging the reaction vessel in an ice bath leading to a homogeneously sized quantum dot solution. Anhydrous methanol precipitation removed all excess ligand followed by dispersion in chloroform allowed for spectroscopic studies of the nanoparticles. The addition of the ZnS shell involved the same reaction vessel containing 5.0 g TOPO which was liquefied by heating to 80°C. After the core solution in chloroform was added to the solvent, all chloroform was evaporated allowing for the addition of 1.78 mL diethylzinc and 0.4 mL of bis(trimethylsilyl)sulfide in a dropwise

fashion over a period of 5 min. The solution was left stirring overnight leading to a homogeneously sized CdSe/ZnS core/shell QD solution. After cooling and washing the solution, the quantum dots were stored in a butanol:TOP (1:2; v/v) solvent at 4°C to ensure stability for subsequent spectroscopic studies.

### ***Dihydrolipoic acid synthesis***

Synthesis of DHLA was performed by dissolving 1 g of DL- $\alpha$ -lipoic acid in methanol and water at 0°C. This mixture was reduced with 2 g of sodium borohydride and left to stir for 4 h. The grey solution was then acidified to pH 3 using HCl, extracted with chloroform, dried with magnesium sulfate and evaporation in the roto-vap produced the acid.



**Scheme 2.1 Dihydrolipoic acid synthesis by reduction of DL- $\alpha$ -lipoic acid with sodium borohydride followed by protonation under acidic conditions.**

### ***CdSe(ZnS)-TOPO ligand exchange to CdSe(ZnS)-DHLA***

Ligand exchange to produce water soluble hydrophilic quantum dots used the freshly synthesized DHLA in excess, 0.5 g, with 5 mL of CdSe(ZnS)-TOPO QDs dispersed in methanol. The mixture is heated to a temperature under that of QD nucleation, 60-80°C for 4 h with stirring while the TOPO ligand was replaced by DHLA on the surface of the quantum dots. Basification of the quantum dots by slow addition of potassium tert-butoxide deprotonated the terminal carboxyl groups on the ligands which precipitated the

QDs from solution. The precipitate was isolated and re-dispersed in water to obtain the hydrophilic QDs.

### ***CdSe(ZnS)-TOPO ligand exchange to CdSe(ZnS)-MPS***

The modification of the TOPO capped (CdSe)ZnS QDs by 3-mercaptopropyltrimethoxysilane (MPS) is the following: 1 mL of (CdSe)ZnS QDs in butanol : TOPO (1 : 2; v/v) were precipitated by anhydrous methanol. The wet precipitate was washed with methanol three more times to remove excess TOPO ligand. Then the wet powder was dispersed in 50  $\mu$ L of distilled MPS. After shaking, 500  $\mu$ L of tetramethylammonium hydroxide methanol solution (pH 10) was added. The optically clear mixture was diluted with 10 mL of anhydrous methanol basified to pH  $\sim$ 10 with TMAOH. After 1 h of shaking under the protection of an argon atmosphere, the MPS capped QDs were purified by 50 K Amicon® Ultra filter device.

## **2.5 Summary**

Chapter 2 details the theory of the instrumentation and techniques used for experimentation of HSA,  $\beta$ -galactosidase and quantum dots. Langmuir monolayer technique is described from a theoretical basis and experimentation procedure including the monolayer formation and *in situ* analysis are described also.

## Chapter 3

### Surface Chemistry and Spectroscopy of the Human Serum Albumin Langmuir Monolayer

#### Background

Human serum albumin is considered ideal for its biological and physicochemical importance which has been studied in detail.<sup>2-6</sup> The function of this ubiquitous, globular protein (50% of protein present in human blood plasma) aids in the maintenance of bodily blood pH and oncotic pressure<sup>7,8</sup> and in addition it has unique properties in its stability and ligand binding.<sup>8-12</sup> These properties are interesting with respect to the interfacial behavior of large molecules such as HSA where the inter- and intramolecular interactions are observable which differ from the molecules' behavior in bulk solution.

The Langmuir monolayer approach utilizes the innate properties of molecules like HSA, including hydrophilicity, polar and charged amino acid residues on the surface along with the isoelectric point, to manipulate the behavior of these molecules. Multiple, previous studies have shown that HSA forms a stable Langmuir monolayer which has been utilized for its abundance in biological interfaces to describes lipid<sup>13-17,41,97</sup> and surfactant<sup>42,43,47,98-101</sup> interactions. A hydrophilic-hydrophobic barrier accurately correlates a molecule's behavior to experimental stresses by observing firstly the ability to remain at this type of interface and also how these molecules behave when interacting over a broad range of surface pressures comparable to those found at the biomembrane.<sup>47,48,102</sup>

In this study, the novelty of the Langmuir technique approach is to investigate the physicochemical and photophysical properties that pure HSA has at the air-water interface and how this stable protein can be manipulated. Measurements of subphase salt

concentration with surface pressure- and surface potential-area isotherms and the effect of the pure protein packing structure are analyzed throughout in this chapter. *In situ* absorbance and fluorescence spectroscopy are correlated with the phase change of the isotherm throughout compression as well as observation of temperature induced aggregate formation by changes in the absorption spectra of the protein at the air-water interface.

### **3.1 Surface chemistry of the human serum albumin Langmuir monolayer**

#### ***Salt concentration effect***

Early experiments<sup>103</sup> established reproducible isotherms of serum albumin Langmuir monolayers which varied the concentrations of NaCl in the subphase at low pH away from the 4.8 isoelectric point of HSA. Isotherms showed that an increase in ionic strength of the subphase causes the monolayer to become more closely packed. In order to confirm the results, experiments were done near the pI of HSA which concluded that with an increase of the limiting molecule area was correlated to an increased ionic strength of the subphase and consequently a more condensed monolayer.

Formation of the HSA Langmuir monolayer was optimized to observe the interfacial behavior of the molecules when compression to high surface pressures by firstly investigating its behavior on a pure water subphase. As seen in Figure 3.1, the surface pressure-area isotherm produced is in good agreement with literature material<sup>34,36,102</sup> and indicated all phases of ideal monolayer formation. Indicated by no immediate increase in surface pressure, the molecules at the beginning of the isotherm are in a state of minimal interaction and heterogeneous orientation at the interface referred to as the gaseous state. A slight increase at  $1,850 \text{ \AA}^2/\text{molecule}$  details a greater degree of interaction

intermolecularly at the interface followed by a sharp rise in surface pressure. Commonly referred to as the liquid-condensed phase, this correlates to a gradual restriction of orientation. In this case, the sharp rise in surface pressure is followed by a collapse of the monolayer into multiple layers at a surface pressure of  $\sim 24$  mN/m at  $1,140$   $\text{\AA}^2/\text{molecule}$ . The steepest part of the isotherm, typically during the liquid-condensed phase reveals an important property of the analyte. When extrapolated down to a zero surface pressure, the limiting molecular area is the condition of the monolayer in a closely packed state which in this case is measured at  $1,650$   $\text{\AA}^2/\text{molecule}$ . Used for comparison amongst different environments, on a pure water subphase, the limiting molecular area is small for a molecule as large as HSA however, the isotherm describes a well spread protein monolayer at the air-water interface.<sup>104</sup>

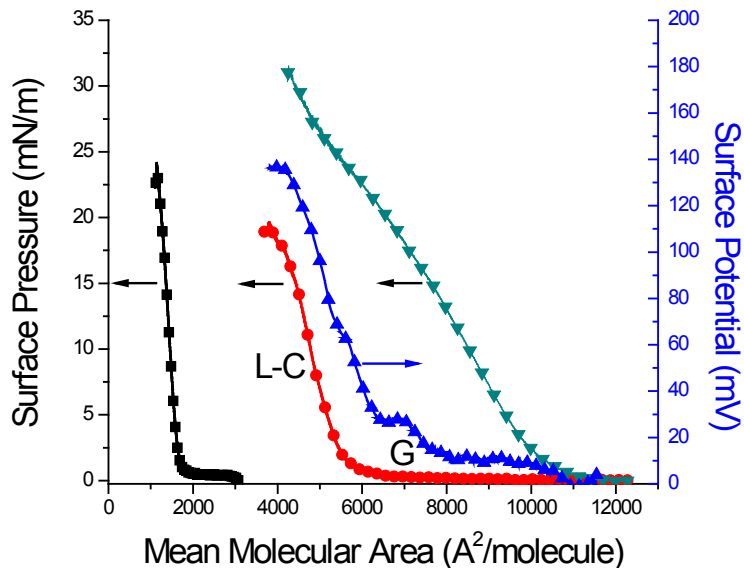


**Figure 3.1** The  $\pi$ -A isotherms for HSA spread on three different subphases at pH 5.7; pure water (■), 0.01 (●) and 0.1 (▼) M NaCl. The accompanying  $\Delta V$ -A isotherm (▲) on a 0.01 M NaCl subphase is shown which correlates well with the  $\pi$ -A isotherm.



In previous literature, a variety of subphases have been used to understand how the protein would interact in the presence of different ion concentrations when working with a mixture of monolayers by introducing propyl alcohol into the subphase.<sup>104,105</sup> Literature results showed that an increase in mean molecular area resulted from an increase in ionic strength of the HSA solution from a mixture of NaCl and amyl alcohol. The study was taken further to show that contrary to the propyl alcohol as a spreading agent, when amyl alcohol was employed, the results were the opposite and an increase in ionic strength resulted in a lower limiting molecular area. Miscibilities of the spreading agent were the explanation of these results since in both cases as the protein unfolded, it remained at the air-water interface. In the case of propyl alcohol, an increase in the ionic strength of the spreading solution caused a decrease in intramolecular interaction that allowed the molecules to unfold easily thereby improving the spreading of the film. Amyl alcohol however did not provide solubility of the protein in the water subphase because the spreading agent is less miscible than propyl alcohol causing less and less to be kept at the air-water interface as the ionic strength was increased.<sup>104,105</sup>

Adding a concentration of salt to the subphase which will dramatically increase the number of molecules which reside at the air-subphase interface. When on a pure water subphase, the expulsion of molecules into the subphase does not depict an accurate, closely packed state when extrapolating the limiting molecular area however, the addition of sodium chloride in this experiment immediately shows an increase in molecular area. A decrease in analyte volume spread from 375 to 100  $\mu\text{L}$  at the interface was required due to an immediate increase in surface pressure without any compression. As seen in Figure 3.1, at a 0.1 M NaCl subphase concentration, an immediate increase in surface

pressure is observed indicating that the molecules are not in a well-ordered state and the homogeneity of the monolayer will not produce an accurate limiting molecular area. Decreasing the subphase concentration to 0.01 M NaCl shows that the isotherm starts at 12,275 Å<sup>2</sup>/molecule with no surface pressure as the molecules are in a gaseous state. Followed by the liquid-condensed phase at 6,190 Å<sup>2</sup>/molecule, the isotherm rises in surface pressure as the molecules reorient themselves while the monolayer is undergoing compression until the collapse at a surface pressure of ~20 mN/m at 3,800 Å<sup>2</sup>/molecule.

The surface pressure-area isotherm as described above details the physical interactions such as intermolecular reorientation at minimal distance of interaction therefore in conjunction, the surface potential-area isotherm is conducted which measures electrostatic interactions such as van der Waals forces as well as coulombic interactions.

When overlaid with the  $\pi$ -A isotherm obtained on a 0.01 M NaCl subphase in Figure 3.1, an increase in surface potential is immediately evident upon compression due to the large amount of electrostatic interactions and large changes in the surface dipole can be correlated with the phase changes observed in the  $\pi$ -A curve as well. The change in slope when observing the surface potential-area isotherm is about identical at 4,100 Å<sup>2</sup>/molecule as with the surface pressure-area isotherm. The Langmuir monolayers produced when utilizing a salt subphase are more condensed and more accurately represent the behavior and physicochemical properties of the protein.

### ***Effect of pH on the HSA Langmuir monolayer***

The influence of pH was studied by introducing HSA to very acidic (pH = 2) and very alkaline (pH = 12) subphases. Both pH extreme subphases produced an expanded isotherm upon comparison to that of subphase near the pI of 4.6 with lower surface

pressures producing the most expanded films. Analyzing these results seen in Figure 3.2 in terms of the ionic form which the HSA molecule takes reveals that in very low pH, the albumin is positively charged with an increase in electrostatic repulsion of the  $R-NH_3^+$  groups causing an expanded film due to the elongated shape of the molecule.

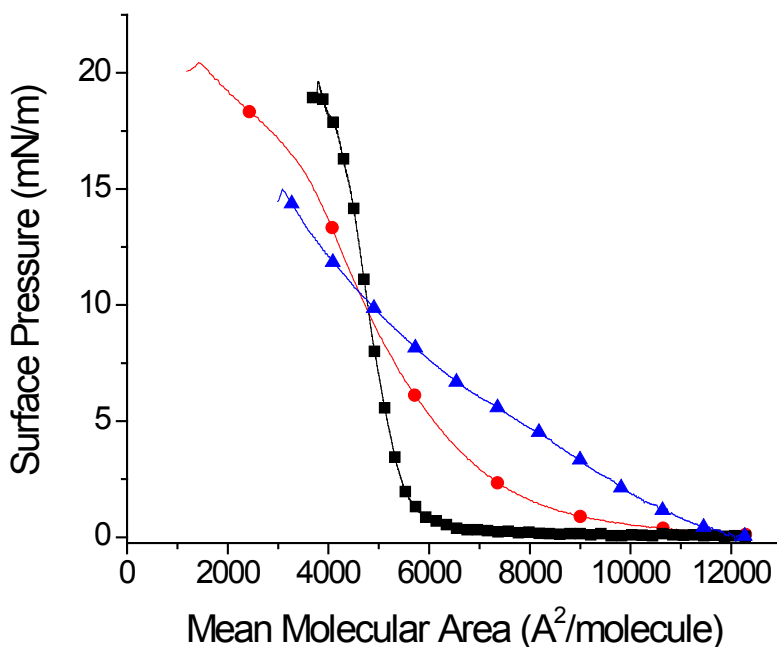


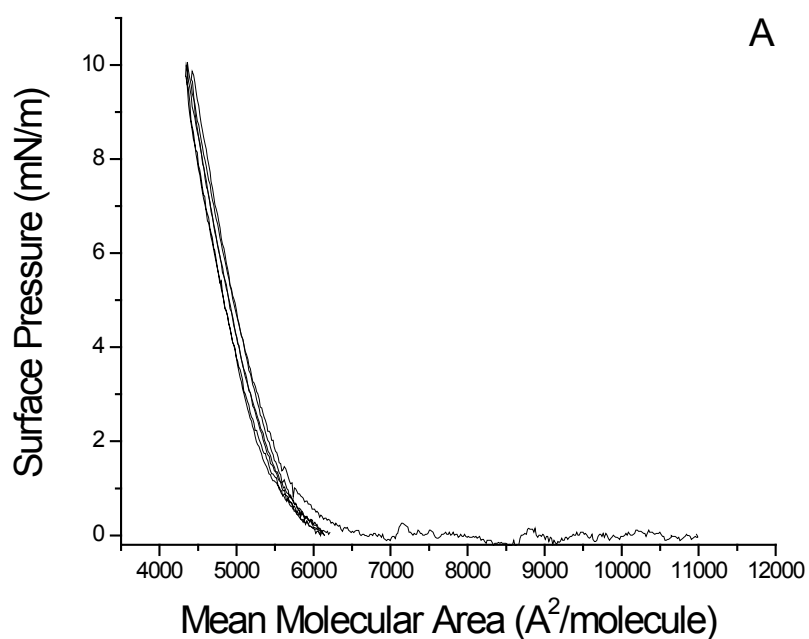
**Figure 3.2** Effect when spreading 0.15 nmol HSA on a 0.01 M NaCl subphase at pH 5.7 (■), 2 (●) and 12 (▼).

This was confirmed by the presence of salt in the subphase which reduced this repulsion and produced more condensed monolayers. Near the pI of the molecule there are an equal number of positive and negative charges from the ionization of the acidic and basic residues. Electrostatic attraction along with an increase in solubility throughout the molecule causes a smaller structure to form thereby reducing the limiting molecular area as compared to the low pH.<sup>104</sup> Extreme basic subphases results in a similar behavior by the protein monolayer where the electrostatic repulsion is carried by the ionized  $R-COO^-$  groups. Upon comparison, monolayers spread on alkaline subphases are more expanded

than when on acidic subphases due to ionization of phenolic hydroxyl groups when the hydrogen bonds of the molecule are broken.<sup>104</sup>

### ***Compression-decompression cycles of the HSA Langmuir monolayer***

During the compression of the monolayer it is important to observe a homogenous one-molecule layer thick film which is free of any aggregation or domain formation. The compression-decompression cycles were conducted to observe at several surface pressures if there is also any loss of the protein from the interface into the subphase, hysteresis, as the molecules are compressed.



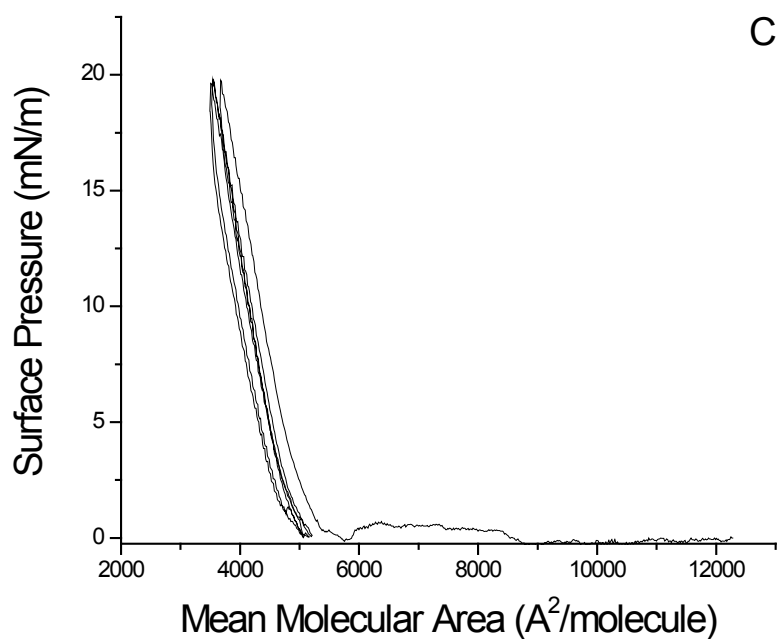
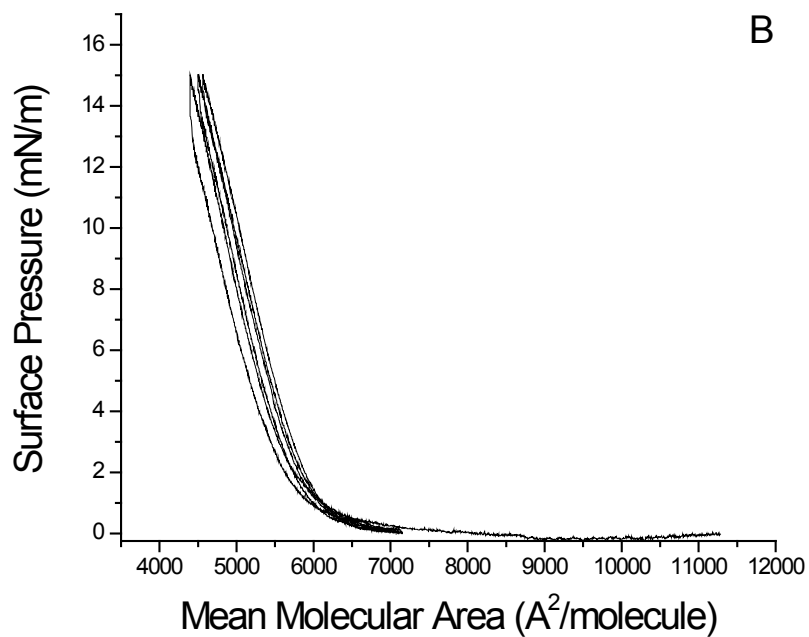


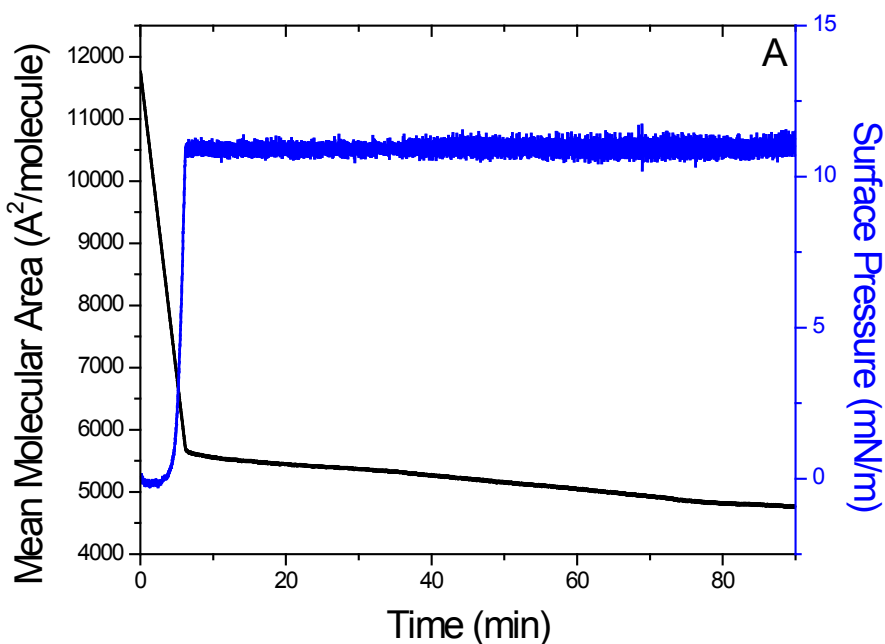
**Figure 3.3** Compression-decompression cycles for the 0.15 nmol HSA Langmuir monolayer on a 0.01 M NaCl subphase up to (A) 10, (B) 15 and (C) 20 mN/m.

Reproduced in triplicate, the three cycle compression-decompression experiments in Figure 3.3A conducted on a pH 5.7, 0.01 M NaCl subphase show that compression up to

10 mN/m there is less than 2% change in the isotherm when comparing the first and last cycle. Figure 3.3B and 3.3C show compression up to 15 and 20 mN/m which also show little hysteresis at changes of 4% each. The lack of hysteresis at these surface pressures shows that the protein monolayer does not form aggregates at the air-water interface within experimental error.

### ***Stability measurements of the HSA Langmuir monolayer***

Stability measurements of the HSA Langmuir monolayer provide insight into the ability of the monolayer to stay at the air-subphase interface for long time periods without appreciable loss of analyte into the subphase. Observed at three important surface pressures gleaned from the  $\pi$ -A isotherm, Figure 3.4A shows that at a surface pressure of 10 mN/m when the monolayer is in a liquid-condensed phase, the monolayer is held for 90 min with an approximate change in area per molecule of only 17%.



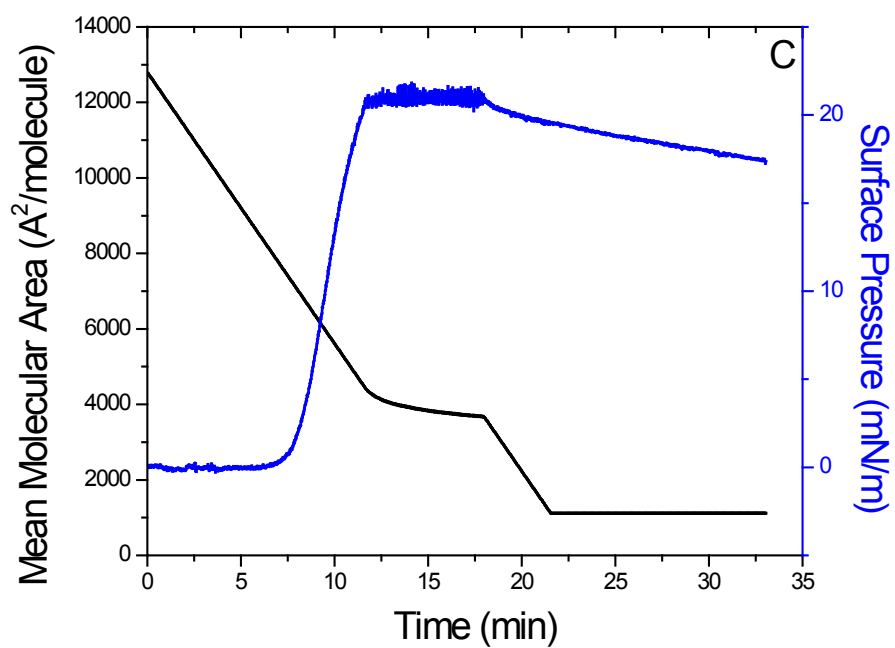
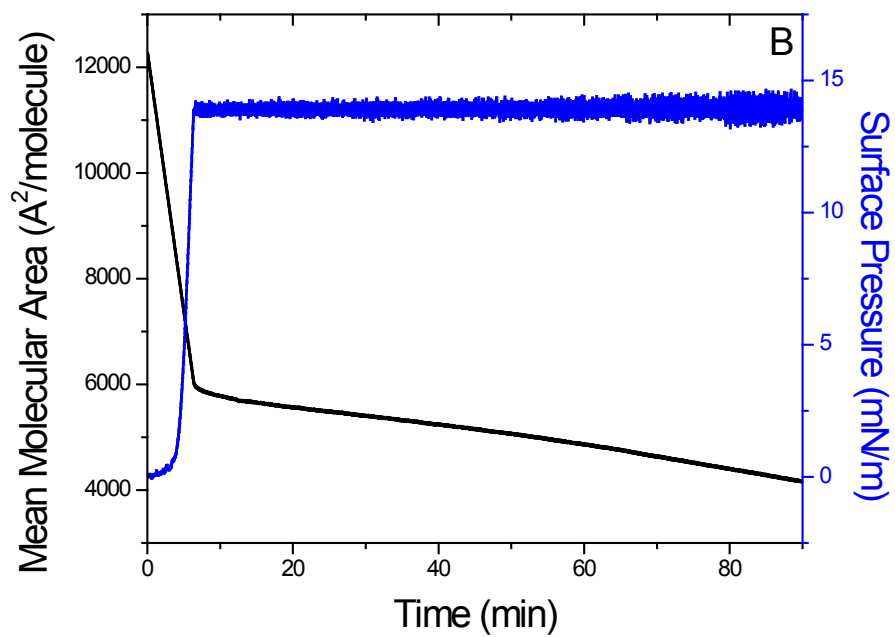


**Figure 3.4** Stability measurements which show over an extended time period if the HSA monolayer can stay at the air-water interface when compressed to higher surface pressures of (A) 10, (B) 15 and (C) 20 mN/m.

Another important surface pressure is the transition from the liquid-condensed phase before the collapse, as in Figure 3.4B a surface pressure of 15 mN/m is held for 90 min at the interface however there is a much greater decrease in the change in area per molecule at 30%. The instability of the monolayer as the surface pressure is increased is evident by this greater change in area per molecule and confirmed by Figure 3.4C. When measuring the monolayer stability at the collapse surface pressure of 20 mN/m, it is not able to be held at this surface pressure for long time periods and collapses after 18 min.

Together, the compression-decompression studies and the stability measurements reveal that while at the highest surface pressure analyzed, 20 mN/m, the effect of time shows that aggregate formation is not immediate. In an attempt to reorient themselves at the air-subphase interface, hysteresis of the HSA molecules expels them into the subphase. These measurements show that the most stable surface pressure for sustained measurements is when the monolayer is the initial liquid-condensed state due to the orientation of the molecules which does not result in aggregate formation.

### **3.2 Photophysical properties of human serum albumin**

#### ***UV-vis absorption and fluorescence spectroscopy in the aqueous phase***

Even with a low content of spectroscopic probes, analysis of human serum albumin produces a large absorbance and high intensity of fluorescence emission. In Figure 3.5 the absorption spectrum of a HSA solution is illustrated to show the sharp peak at  $\lambda_{\max} = 278$  nm correlating to the  $\pi \rightarrow \pi^*$  transitions of benzene rings of tyrosine residues and indole rings of tryptophan residues in peptide chains of HSA. Overlaid with the UV-vis absorbance shows the fluorescence emission at an excitation wavelength of  $\lambda_{\text{exc}} = 285$  nm with an emission band at  $\lambda_{\text{em}} = 350$  nm with set excitation and emission slit widths of 5



nm. The tryptophan moiety has the largest intensity of emission which overlaps any emission of lower intensity occurring from other chromophores in the molecule.

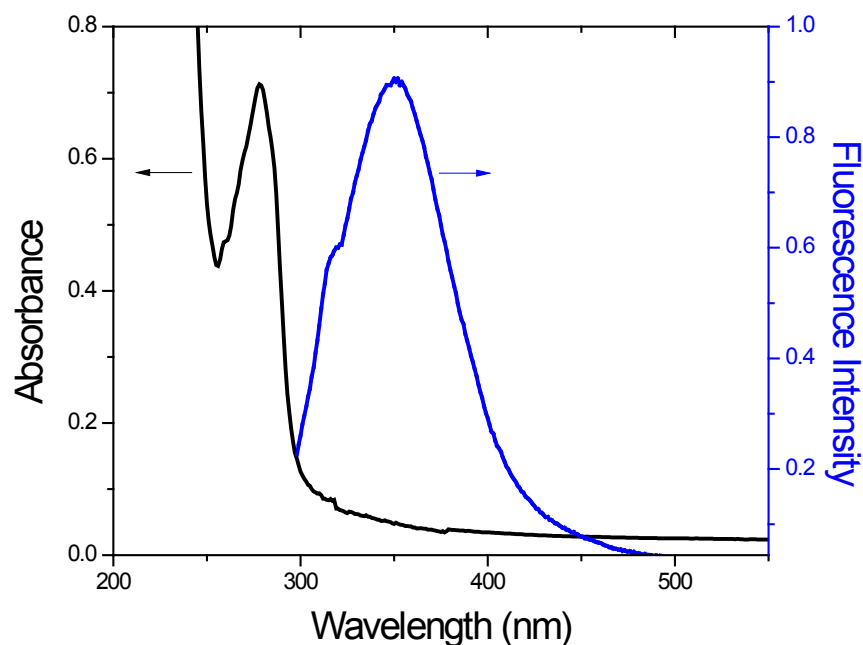


**Figure 3.5** UV-vis absorption and fluorescence spectra of an aqueous HSA solution in pure water, pH 5.7, with a 1 cm optical path length quartz cell analyzed. Analysis of the UV-vis spectrum at  $\lambda_{\text{max}} = 278$  nm correlates to the single tryptophan residues  $\pi$  to  $\pi^*$  electronic transition and a concentration of 1.34 mg/mL (20.16  $\mu\text{M}$ ). Fluorescence spectrum was produced from a solution concentration of 0.1 mg/mL (1.42  $\mu\text{M}$ ) by excitation of the tryptophan residue in HSA at  $\lambda_{\text{exc}} = 285$  nm having a maximum intensity of emission at  $\lambda_{\text{em}} = 350$  nm.

***In Situ UV-vis absorption of the HSA Langmuir monolayer.***

The difference between the behavior of molecules in a bulk solution and their behavior at the air-subphase interface can be seen by not just the physical interaction but also by photophysical observation. UV-vis absorption spectroscopy of the HSA Langmuir monolayer was conducted with a higher concentration of HSA (0.5 mg/mL) in order to accommodate the larger trough area. Conducted in the absence and presence of sodium chloride in the subphase as previously in the formation of the Langmuir monolayer,

Figure 3.6 coincides with the results that increases in salt concentration not only closely packs the molecules at the interface but also reduces the amount of HSA expelled into the subphase. When observing the absorption of HSA at the air-water interface, the increase in the band at  $\lambda_{\max} = 278$  nm relating to the single tryptophan residue was plotted as a function of increases in surface pressure. Pure water subphase shows an increase in absorbance nearing the collapse of the monolayer reported earlier at 25 mN/m. The concentration of salt in the subphase shows that increasing from 0.01 to 0.1 M increase the absorbance of HSA also however observation of the higher salt concentration as is the case with the Langmuir studies shows no formation of a monolayer but rather just a steady increase in HSA absorbance until the collapse at 25 mN/m. The kink point seen in all isotherms relating to the beginning of the monolayer collapse reported in Figure 3.1 correlates with the a larger increase of absorbance over 15 mN/m. The lower concentration of salt, 0.01 M, correlates well with the  $\pi$ -A and  $\Delta V$ -A isotherms which shows up to 10 mN/m, the absorbance is linear until 15 mN/m where there is a sharp rise in absorbance as the monolayer begins to collapse and up to the collapse just before 25 mN/m there is an larger increase in absorbance. As seen in the compression-decompression cycles for the 0.01 M NaCl subphase, absorbance data shows that HSA is forming a stable monolayer on all three subphases. Based on the increases in absorbance for each trial, hysteresis does not occur throughout compression since the absorbance values continue to increase which is direct evidence of the continued presence of the protein at the interface.

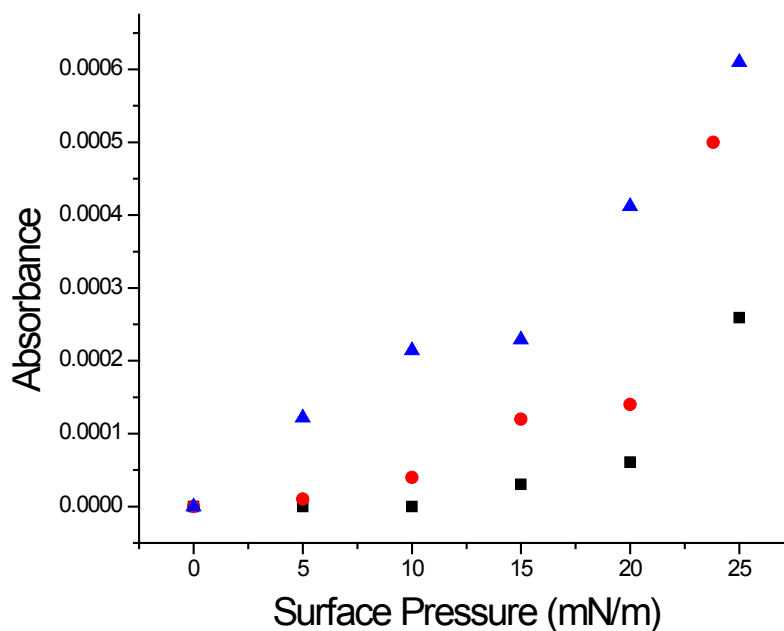


**Figure 3.6** *In situ* UV-vis absorption at the air-water interface of the HSA Langmuir monolayer formed on three different NaCl concentrations, pH 5.7; (■) pure water, (●) 0.01 M NaCl and (▲) 0.1 M NaCl, analyzed at the maximum absorbance,  $\lambda_{\max} = 278$  nm, as a function of increasing surface pressure.

#### *In situ* fluorescence spectroscopy of the HSA Langmuir monolayer

The fluorescence emission of the tryptophan moiety in human serum albumin which has a strong intensity at  $\lambda_{\text{em}} = 350$  nm can be utilized in a similar manner as UV-vis absorption to correlate surface compression with protein stability. With an excitation wavelength of 285 nm, the fluorescence of the single tryptophan in an HSA solution is clearly visible as seen in Figure 3.5 which dominates the fluorescence emissions of other amino acid residues such as tyrosine and phenylalanine at lower wavelengths. Initial studies of the *in situ* fluorescence spectroscopy of the HSA Langmuir monolayer only produced a band of scattering light at  $\lambda_{\text{em}} = 420$  nm, therefore in order to measure the fluorescence of the HSA tryptophan residue a concentrated spreading amount (100  $\mu\text{L}$ , 6 mg/mL) was placed at the air-water interface on a subphase of 0.1 M NaCl in Figure 3.7.

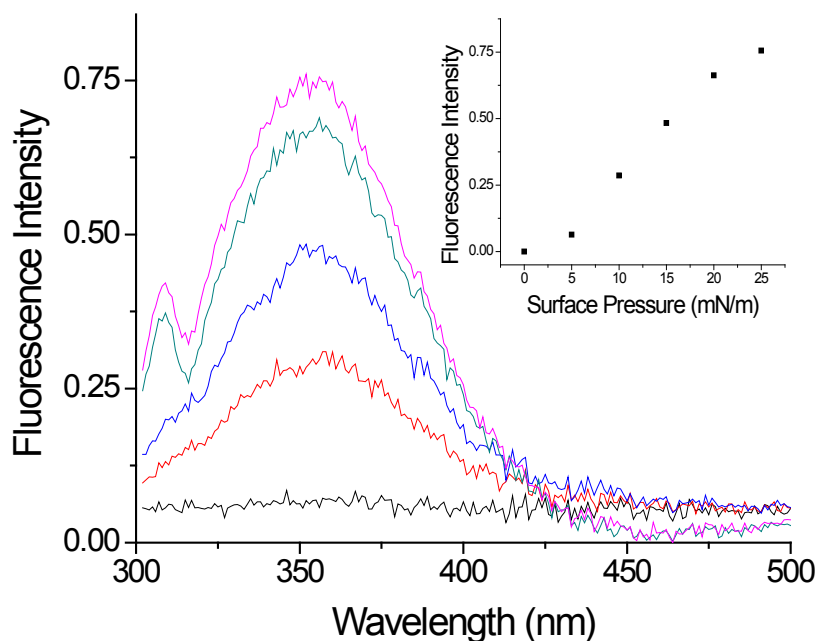


**Figure 3.7** *In situ* fluorescence spectroscopy of HSA produced by 100  $\mu\text{L}$  of a 6 mg/mL solution on a 0.1 M NaCl subphase as compressed from 0 to 25 mN/m onto of a KSV trough with a slit width of 5 nm for both the excitation and emission spectra. Inset: Analysis at the  $\lambda_{\text{em}} = 350$  nm corresponding to the tryptophan moiety in HSA as a function of surface pressure showing no indication of monolayer formation but rather a film as it increases steadily throughout compression.

Analysis of the corresponding spectra showed an increase in the fluorescence intensity of the tryptophan band as the surface pressure was increased from 0-25 mN/m and also the other distinct scattering light band at 420 nm which did not increase in intensity as the experiment proceeded. When compared to the trend of absorbance increase on a 0.1 M NaCl subphase in Figure 3.6, even with an increased amount of protein, there is a similarity to a steadily larger intensity of emission throughout compression due to the closely packed structure of the molecules. These results however are not ideal to measure the proper formation of a Langmuir monolayer as the necessity for an increased spreading amount did not produce all monolayer phases.

### ***In situ protein fibrillation***

The ability of a biomacromolecule to perform innate functions arises from its structural components namely the secondary structure as well as amino acid sequence. During the process of self-association due to external conditions or perhaps loss of protein homeostasis within a biological environment a protein will begin to form aggregates. Such external conditions as temperature have a dramatic effect on protein homeostasis as they can disrupt the natural environment in which the protein persists or the balance of protein synthesis and folding. These types of disruption over an extended period of time results in protein aggregates lack functionality and contribute no relevant biological activity. Without the ability for these proteins to perform essential cell processes, the biological infrastructure can be disrupted to a point of increased toxicity within the body or even cell death which has been discovered to be the cause of many diseases.<sup>106-109</sup>

With information about the necessity of a salt subphase and measured stability of the monolayer, protein fibril formation was studied at the air-water interface utilizing the absorbance of the tryptophan moiety in HSA. A stable monolayer was formed and held at a surface pressure of 10 mN/m while the trough and subphase was kept at physiological temperature of 37°C. As seen in Figure 3.8, the first six h of experimentation show a linear increase in HSA absorbance at  $\lambda_{\max} = 278$  nm correlating to an increase in HSA aggregation at the interface followed by a second trend where for the following four h, the absorbance stayed at a constant value.

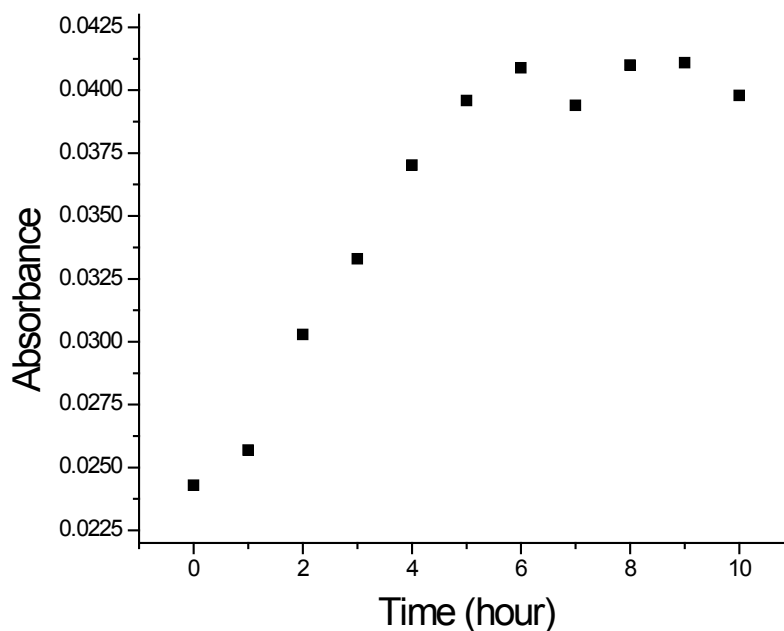


**Figure 3.8** Temperature induced HSA aggregation measured by *in situ* UV-vis absorption at a physiological temperature of 37°C showing two trends of aggregation when the monolayer is held at a surface pressure of 10 mN/m. The first six h of heating analyzed at  $\lambda_{\text{max}} = 278$  nm show a linear increase in absorbance while after this time the absorbance is constant.

These two trends indicate that the protein molecules at the interface aggregated under these conditions during the first six h which did not result in hysteresis due to the monolayer being stable without the need for further compression to hold the surface pressure at 10 mN/m.

### 3.3 Conclusion

A stable and reproducible Langmuir monolayer is shown to be formed by HSA on a NaCl subphase which correlates to the molecules behavior near its isoelectric point. Manipulation of subphase pH showed an increase in electrostatic repulsion when protonated and an even more expanded monolayer when introduced to a basic environment. On the basis of the monolayer stability, *in situ* experimentation revealed

tryptophan absorbance increased throughout compression in excellent correlation to monolayer formation. Fluorescence spectroscopy at the air-water interface showed a closely packed molecular structure only after experimentation was adjusted with an increased spreading amount and salt concentration in the subphase. Aggregation induced by physiological temperatures showed two trends where the molecules have a linear increase in absorbance over the first six hours and a stable absorbance of the monolayer after this time frame.

## Chapter 4

### $\beta$ -galactosidase

#### Background

Analysis by Matrix-Assisted Laser Desorption/Ionization Time of Flight confirms the high molecular weight of the  $\beta$ -galactosidase monomer at 116,646.1 Da as seen in Figure 4.1.

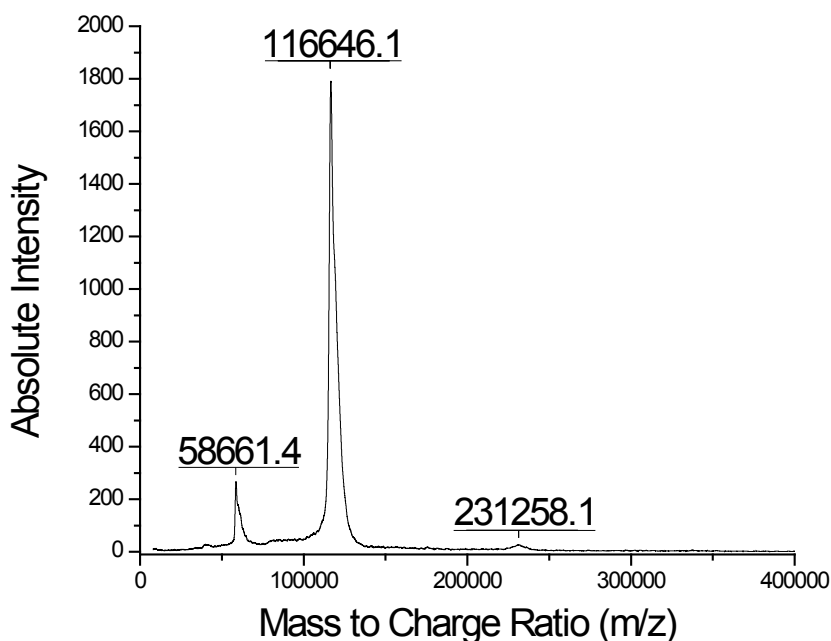


**Figure 4.1 Matrix-assisted laser desorption/ionization time of flight spectrum of  $\beta$ -galactosidase showing a monomer molecular weight of 116,646.1 Da.**

Theoretical analysis of  $\beta$ -galactosidase reveals that based on its amino acid content it also has a high molar extinction coefficient ( $\epsilon = 262,690 \text{ M}^{-1}\text{cm}^{-1}$ ) making it ideal to study analytically to measure changes in concentration while the environmental conditions are altered:<sup>110</sup>

$$\epsilon (\text{M}^{-1}\text{cm}^{-1}) = (\#\text{Trp})(5,500) + (\#\text{Tyr})(1,490) + (\#\text{cysteine})(125) \quad (4.1)$$



UV-vis absorption was used to analyze and confirm the concentration of the  $\beta$ -galactosidase bulk solution. The concentration was accurately calculated based on dilutions of the enzyme, initially a dry powder, kept at  $-4^{\circ}\text{C}$  by utilizing the reported  $E^{1\%} = 20.9$  of the enzyme.<sup>89</sup> Langmuir monolayers were obtained with a bulk solution concentration of  $0.2\text{ mg/mL}$  relating to an absorbance of  $\sim 0.4$  at the maximum absorption of tryptophan moiety,  $\lambda_{\text{max}} = 282\text{ nm}$ .

#### **4.1 Photophysical properties of $\beta$ -galactosidase**

##### *UV-vis and fluorescence emission spectra*

The high content of tryptophan residues among the amino acids contained in  $\beta$ -galactosidase is of interest to researchers because spectroscopically one is able to analyze the state of the enzyme for any conformation changes which would dramatically affect the intensity of absorbance and emissions from the amino acid. Firstly, the characterization of the native enzyme in pure water at pH 5.7 was conducted seen in Figure 4.2 which revealed with UV-vis absorption a maximum absorbance from the tryptophan moiety at  $\lambda_{\text{max}} = 282\text{ nm}$ . Overlaid with the UV-vis absorbance shows the fluorescence emission at an excitation wavelength of  $\lambda_{\text{exc}} = 284\text{ nm}$  with an emission band at  $\lambda_{\text{em}} = 354\text{ nm}$  with set excitation and emission slit widths of  $3\text{ nm}$ . The tryptophan moiety has the largest intensity of emission which overlaps any emission of lower intensity occurring from other chromophores in the molecule.

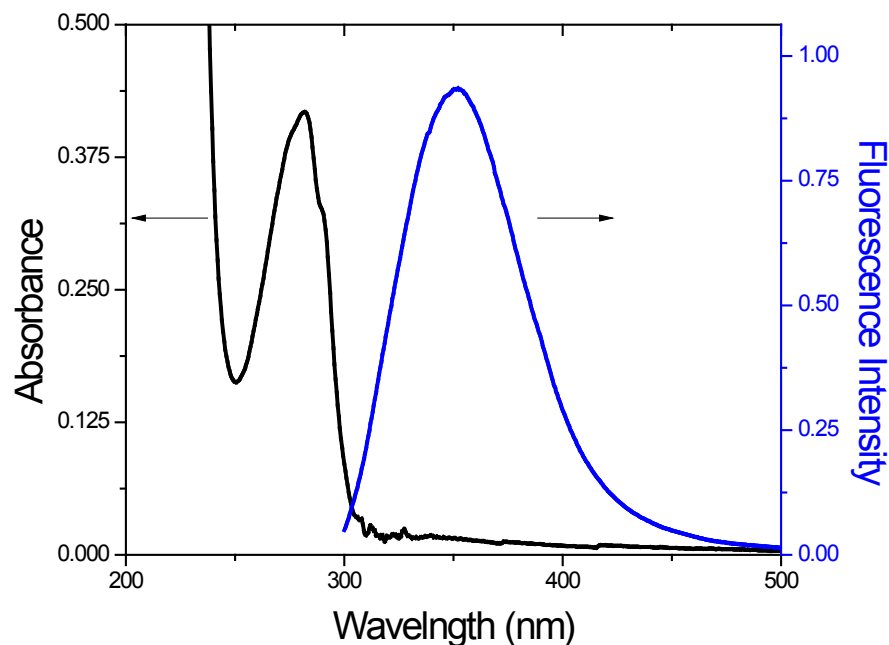


**Figure 4.2** UV-vis absorption and fluorescence spectra of an aqueous  $\beta$ -galactosidase solution in pure water, pH 5.7, with a 1 cm optical path length quartz cell. UV-vis analysis at  $\lambda_{\text{max}} = 282$  nm results in an enzyme concentration of 0.2 mg/mL (1.72  $\mu\text{M}$ ) using the  $E^{1\%}$  of 20.9. Fluorescence spectrum was produced after dilution of the enzyme by a factor of 10 (0.172  $\mu\text{M}$ ) with an excitation wavelength of  $\lambda_{\text{exc}} = 284$  nm having a maximum intensity of emission at  $\lambda_{\text{em}} = 354$  nm having slit widths of 3 nm for both.

#### *Aggregation analysis via UV-vis absorption*

The native state of the enzyme, which has an isoelectric point (pI) of 4.6,<sup>86</sup> shows that at a surrounding aqueous pH of an equivalent nature the enzyme will be in its zwitterionic state. The effect of pH in terms of UV-vis absorption is plotted as a change in absorption intensity over the course of 30 min in Figure 4.3. While in an aqueous environment similar to the pI of the enzyme, an increase in protein concentration is observed via UV-vis as the tryptophan absorption peak intensifies. This observation is in correlates to the formation of protein aggregates and it is possible that the monomeric form of the enzyme forms the tetramer while in this environment due to the reduction in repulsion throughout the molecule. As the pH of the aqueous environment becomes more

acidic and alkaline than the pI, this aggregation effect is not observed possibly due to the repulsion from charged residues on the protein surface.

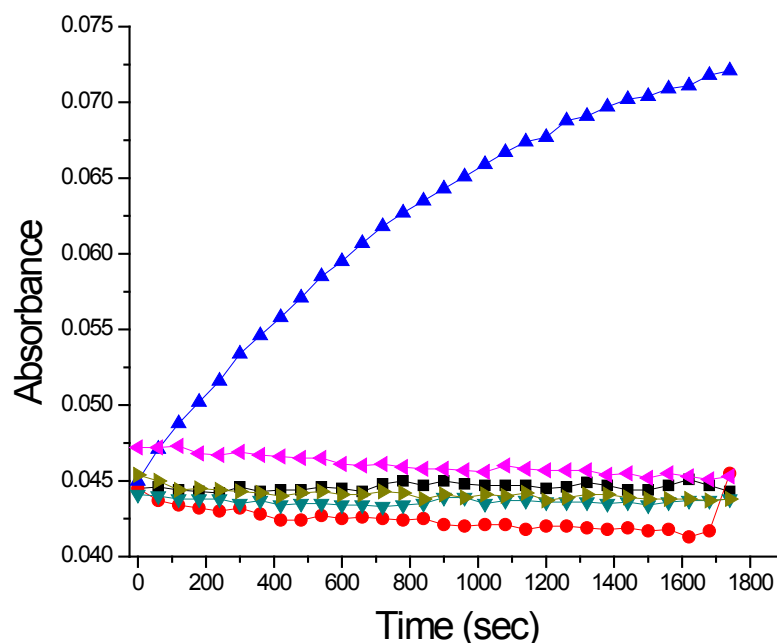


**Figure 4.3** UV-vis absorption of  $\beta$ -galactosidase solution ( $0.172 \mu\text{M}$ ) with a 1 cm optical path length quartz cell by adjusting the aqueous environment to pH 2 (■), 3 (●), 4 (▲), 6 (▼), 8 (◄) and 10 (►) and analysis by UV-vis absorption spectroscopy. The  $\lambda_{\text{max}}$  over a 30 min time period increased in intensity for the pH 4 solution showing that near the pI of the enzyme there is an increase in concentration of  $\beta$ -galactosidase molecules related to the aggregation of the monomer in solution.

#### *Circular dichroism spectropolarimeter*

Along with the unique photophysical properties of  $\beta$ -galactosidase, conformational studies conducted via circular dichroism have shown the enzymatic activity dependence on cations in solution<sup>52-54</sup> and large secondary structure changes during thermal denaturation have been observed which showed a loss in activity and an extended  $\beta$ -sheet like conformation. CD is commonly used in this manner to study the changes in protein conformation especially in  $\beta$ -galactosidase where the  $\beta$ -sheet content calculated to be 48% previously is much higher than the  $\alpha$ -helix content.<sup>31,111</sup>

Circular dichroism is used to observe the  $\alpha$ -helix content with characteristic negative peaks at 209 and 222 nm as well as one positive peak at 192 nm. The  $\beta$ -sheet can also be calculated from these spectra which has a negative band at 218 nm and a positive band at 195 nm. The changes in  $\beta$ -sheet and  $\alpha$ -helix content measured by circular dichroism as a function of change in pH is in good agreement with previously reported values in Figure 4.4.<sup>111</sup> The CD analysis shows a small increase in  $\alpha$ -helix content toward higher pH with a decrease in  $\beta$ -sheet content which has been reported to favor enzyme-substrate interactions. A decrease in pH has been reported to decrease the activity of the enzyme as seen by the shift in secondary structure of the enzyme due to local change in charged residues as well as protein aggregation from these conformational changes.

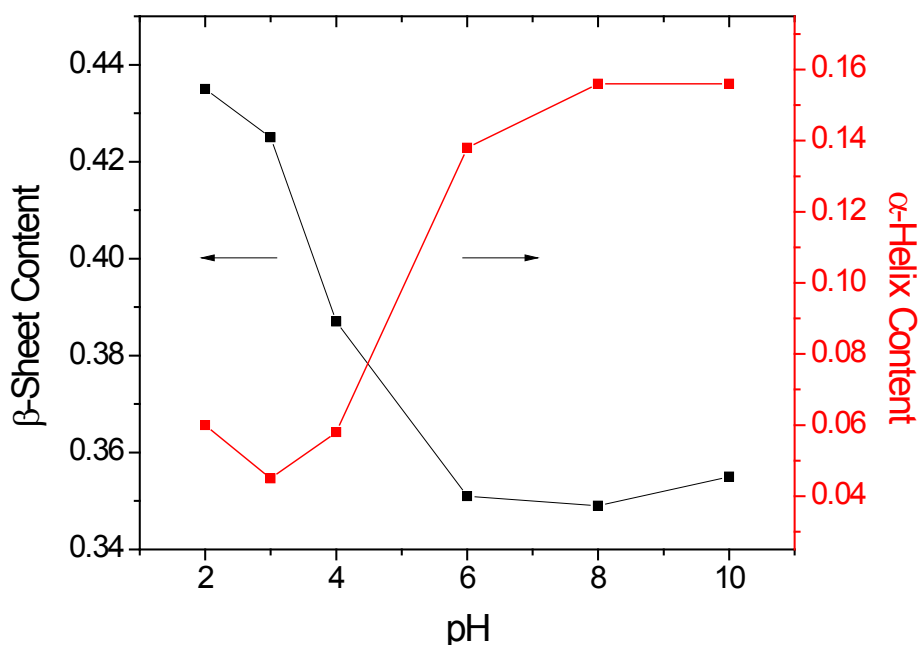


**Figure 4.4** Circular dichroism analysis of 35 averaged scans over a 30 min time period of a  $\beta$ -galactosidase solution ( $0.172 \mu\text{M}$ ) with a 0.2 cm optical path length quartz cell at different pH. As the pH is decreased from the pI of  $\beta$ -galactosidase (4.6),  $\beta$ -sheet content increases, and  $\alpha$ -helix content decreases. An increase in pH away from the pI reduces the  $\beta$ -sheet content and increase the  $\alpha$ -helix content.

### *Fluorescence quenching over time*

The photophysical phenomenon of quenching is observed with experimentation of  $\beta$ -galactosidase over long time periods. Fluorescence spectra obtained at 1 min intervals over 20 min show the intensity of emission from tryptophan analyzed, at  $\lambda_{em} = 354$  nm, is reduced to a very low level of intensity shown in Figure 4.5A. In order to confirm this behavior, the quenching was also observed with emissions being recorded at 5 min intervals over 20 min which showed a similar quenching trend over time Figure 4.5B.

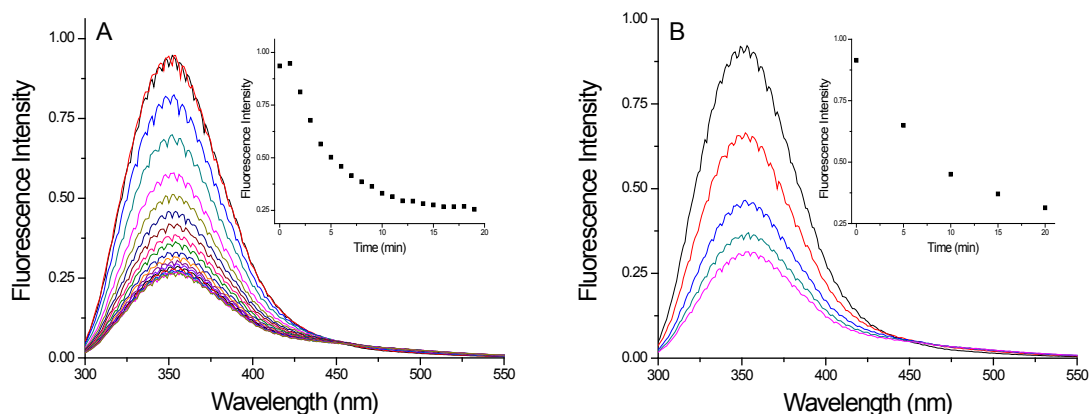


**Figure 4.5** Fluorescence quenching over a 20 min time period of a 0.2 mg/mL aqueous  $\beta$ -galactosidase solution in pure water, pH 5.7, with a 1 cm optical path length quartz cell. Spectra were recorded at (A) one and (B) five min intervals with an excitation wavelength of  $\lambda_{exc} = 284$  nm with slit widths of 3 nm for excitation and emission. (Inset) The maximum intensity of the emission spectra,  $\lambda_{em} = 354$  nm, was used to observe the quenching trend.

The quenching effect of the tryptophan moiety in the enzyme was of particular interest as without accurate and steady fluorescence intensity, other studies could not be conducted. Initially the hypothesis was that the quenching effect was reversible which would result in recovery of emission intensity from the enzyme, however given large amounts of time after the quenching effects inside the fluorometer the emission intensity is not recovered in Figure 4.6.

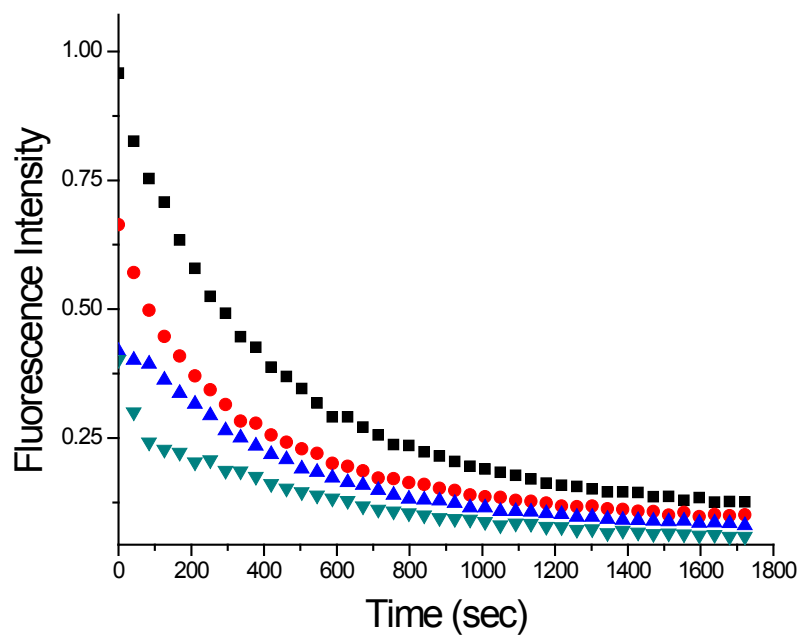


**Figure 4.6** Fluorescence quenching trend of a 0.2 mg/mL aqueous  $\beta$ -galactosidase solution in pure water, pH 5.7, with a given amount of time for recovery using a single sample showed the quenching effect continued without full intensity recovery with different waiting-time periods between trials. Initial fluorescence quenching over a 30 min time period (■), 10 min waiting time period following by 30 min of fluorescence (●), subsequent 15 min waiting time period following by 30 min of fluorescence (▲), and subsequent 30 min waiting time period following by 30 min of fluorescence (▼).

The possibility of a thermal denaturation effect inside the fluorometer would explain that given certain conformation changes in the enzyme structure, the tryptophan moiety was no longer available to emit fluorescence. Observations showed that the temperature inside the instrument measured at slightly ( $\sim 0.5$  °C) above room temperature. Therefore, samples of equal concentration being heated to 37 and 60°C in order to see any irregularity in the fluorescence degradation over time were analyzed however without any difference in quenching trend upon comparing the three different parameters, the stability of the thermal stability of the enzyme was not the cause of fluorescence emission quenching shown in Figure 4.7.

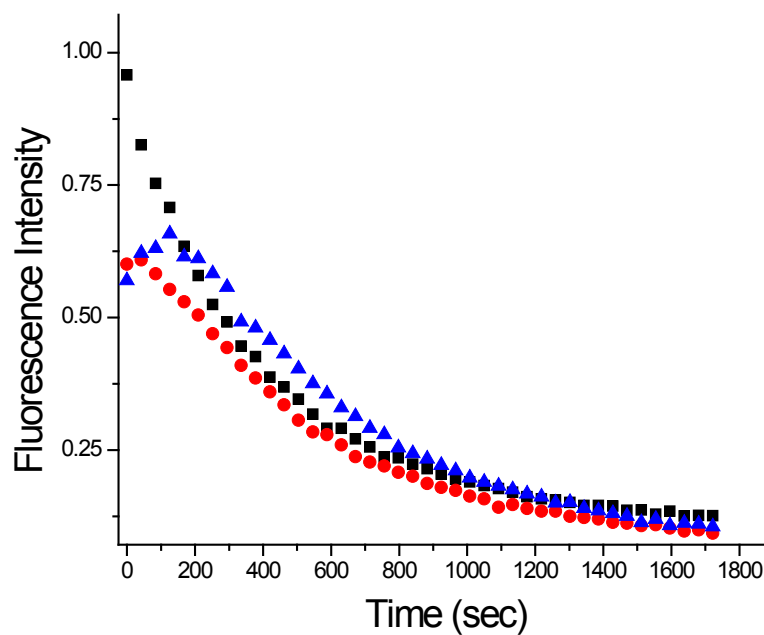


**Figure 4.7 Analysis of fluorescence emission of an aqueous  $\beta$ -galactosidase solution (0.2 mg/mL) in pure water, pH 5.7, at  $\lambda_{em} = 354$  nm with slit widths of 3 nm at different temperatures of 20 (■), 37 (●) and 60°C (▲) resulting in initial decrease in emission intensity but following the same quenching trend.**

The effect of pH on the state of the tryptophan was also necessary in order to see if the stability of the molecule in solution was relevant considering the isoelectric point of the enzyme. The native state of the enzyme which has an isoelectric point of 4.6 shows that at a surrounding pH of an equivalent nature the enzyme will be in its zwitterionic state. Tryptophan is a nonpolar, hydrophobic amino acid therefore it goes unaffected by the change in pH environment in terms of intensity which describes why during the course of pH experimentation, only slight deviations from the initial experimental results were observed in Figure 4.8A-C.

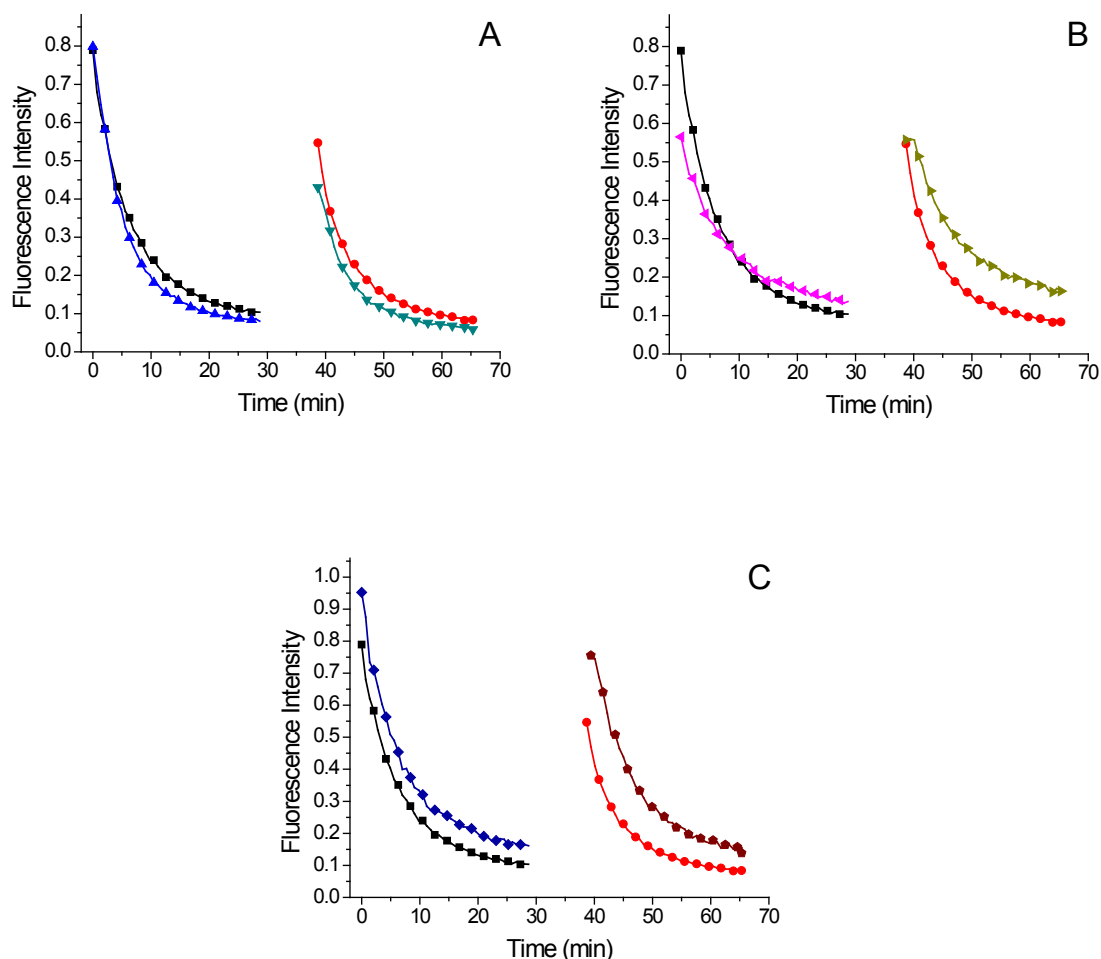


**Figure 4.8** Fluorescence spectra analyzed at 354 nm after excitation at 284 nm having slit widths of 3 nm showing the quenching of a  $\beta$ -galactosidase solution (0.172  $\mu$ M) emission at (A) pH 4 ( $\blacktriangle$ ,  $\blacktriangledown$ ), (B) 2 ( $\blacktriangleleft$ ,  $\blacktriangleright$ ) and (C) 8 ( $\blacklozenge$ ,  $\blacklozenge$ ), with little deviation from the sample in DI H<sub>2</sub>O ( $\blacksquare$ ,  $\bullet$ ).

Analysis of the secondary structure of  $\beta$ -galactosidase before and after fluorescence quenching did not correlate a major change in Figure 4.9. Therefore, the quenching of tryptophan fluorescence over time can be explained possibly by the high content of tyrosine residues which have been shown to engage in non-radiative energy exchange between tryptophan residues according to the Fluorescence Resonance Energy Transfer (FRET) theory.<sup>90</sup>



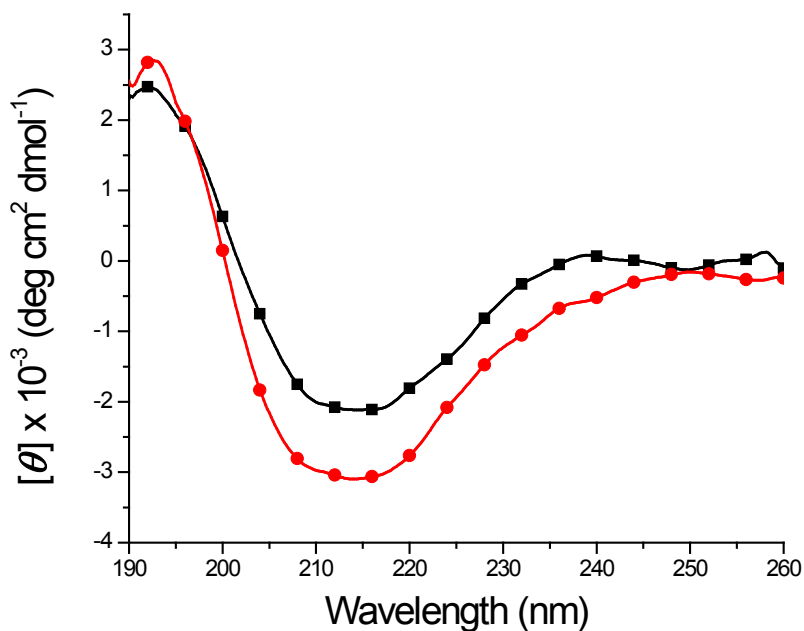


**Figure 4.9** Circular dichroism before (■) and after (●) fluorescence quenching of a  $\beta$ -galactosidase solution (1.72  $\mu\text{M}$ ) with a 0.2 cm optical path length. The spectra reveal little change in the secondary structure of the enzyme with the native enzyme having 6.2%  $\alpha$ -helix and 43%  $\beta$ -sheet before fluorescence and 6.5%  $\alpha$ -helix and 42.2%  $\beta$ -sheet after the quenching effects.

In this process, the energy transfer results in quenching of the donor emission, in this case the tryptophan moiety and an increase in acceptor fluorescence intensity. This increase in tyrosine emission is not observed throughout the experimentation therefore reasoning for the quenching effect of the enzyme can be a mechanism where electrons are exchanged in a non-radiative process from donor in the triplet state to an acceptor group in the ground state during excitation.<sup>112</sup> Commonly referred to as Dexter energy transfer, this process can be an intramolecular process between different moieties in the enzyme molecule or an intermolecular process among other molecules in solution. The result of this process is the subsequent quenching of tryptophan fluorescence which is not able to recover the initial fluorescence intensity of emission.

## 4.2 Substrate interaction studies

### *Michaelis-Menten constant determination: $\beta$ -galactosidase interaction with X-gal*

Classically,  $\beta$ -galactosidase has been used for colorimetric assays which utilized substrates having chromogenic aglycones.<sup>20</sup> Previously discussed, o-nitrophenyl- $\beta$ -D-galactopyranoside is the standard for specific activity determination of  $\beta$ -galactosidase based the hydrolysis of the glycosidic linkage within the substrate by the enzyme. Once free, o-nitrophenol produces a yellow color via tautomerization which is analyzed via an absorption peak at 410 nm. The steady-state rate equation for a homogenous reactions involved a recycling catalyst also referred to as the Michaelis-Menten equation can be calculated from analysis of changes in concentration while keeping the enzyme amount constant.

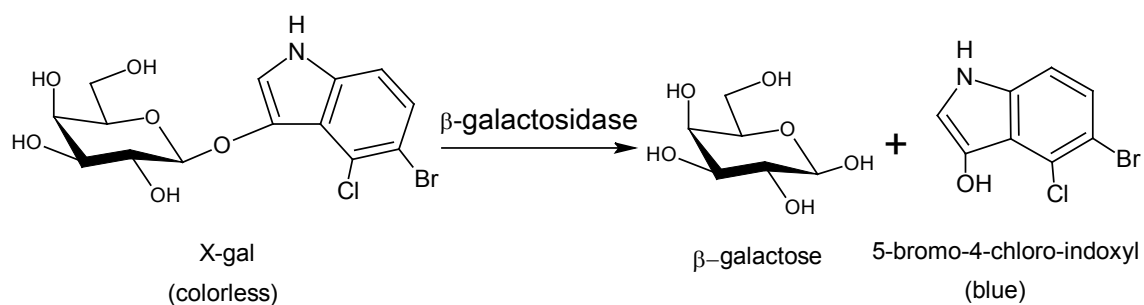
$$\text{Rate } (v) = \frac{d[P]}{dt} = \frac{(\text{Maximum velocity})[\text{Substrate}]}{k_m + [\text{Substrate}]} = \frac{V_{max}[S]}{k_m + [S]} \quad (4.2)$$

A double reciprocal plot, Lineweaver-Burk plot, can then be implemented to analyze the Michaelis-Menten equation above to observe the enzyme kinetics.

$$v = \frac{V_{max}[S]}{k_m + [S]} \quad (4.3) \qquad \frac{1}{v} = \frac{k_m + [S]}{V_{max}[S]} = \frac{k_m}{V_{max}[S]} + \frac{1}{V_{max}} \quad (4.4)$$

The Michaelis constant can then be directly measured which is defined by the substrate concentration at which the reaction rate is at half maximum. It is therefore an inverse measure of substrate affinity for the enzyme, i.e. a small value  $k_m$  is correlated to a high affinity of the enzyme for the substrate.<sup>1</sup> Changes in ONPG concentration have shown that the enzyme has simple enzyme-substrate complex dependence measurable by a Lineweaver-Burk plot.

X-gal is also a glycoside which can be utilized to observe concentration dependence rate changes via the Lineweaver-Burk plot. In the past, X-gal has been used not as a quantifying agent of  $\beta$ -galactosidase but rather as a qualitative analytical tool. In the presence of the enzyme, X-gal is hydrolyzed into two separate moieties, one of which is observed as a blue color in Scheme 4.1. The use of X-gal as a chromogenic substrate while working at optimal pH ranges for  $\beta$ -galactosidase activity makes it a specific and quantifiable substrate for purposes of Michaelis constant determination.<sup>113</sup>



**Scheme 4.1 Enzymatic  $\beta$ -D-galactosyl cleavage via hydrolysis of X-gal, a glycoside substrate, by  $\beta$ -galactosidase resulting in a blue solution.**

Interactions of  $\beta$ -galactosidase and X-gal were analyzed via an increase in absorbance over time as a function of the change in X-gal concentration which revealed that a systematic increase in substrate concentration led to an initial increase in concentration of blue color in Figure 4.10.

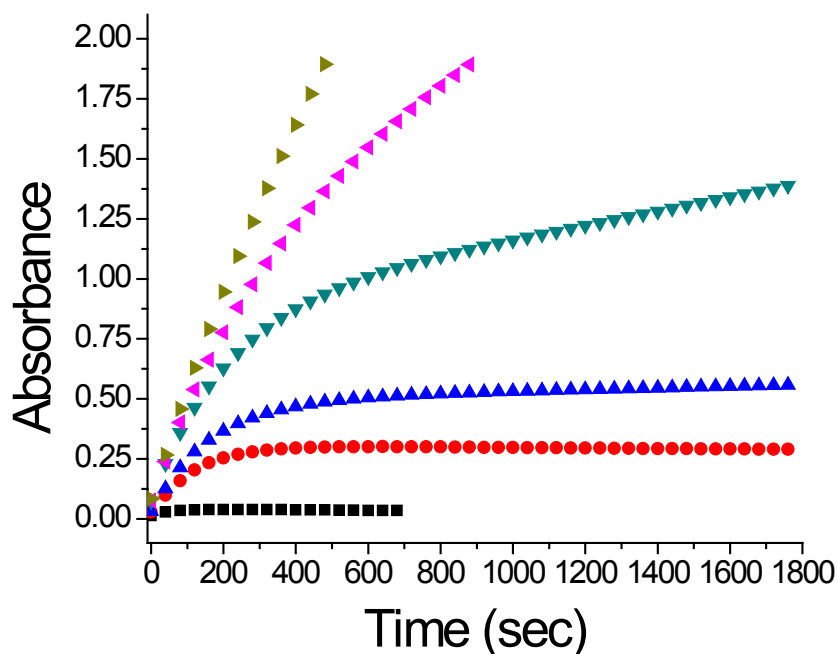


**Figure 4.10** UV-vis absorption studies of  $\beta$ -galactosidase interacting with various concentration of X-gal (mg/mL); 0.02 (■), 0.10 (●), 0.15 (▲), 0.25 (▼), 0.35 (◄), 0.50 (►). An increase in concentration of the substrate is correlated by an increased rate of hydrolysis allowing further analysis to determine the Michaelis constant for X-gal.

Analysis of the concentration of  $\beta$ -galactosidase was not possible due to interference at the wavelength which the enzyme absorbs light therefore analysis was done in the region in which blue color is absorbed. Calculations of the slope created by the progression of blue color in solution during the increase of X-gal concentration were analyzed which accounted for the rate at which the reaction was occurring. The rate of the reaction occurring as a function of the inverse of concentration can then be plotted as a Lineweaver-Burk plot shown in Figure 4.11.

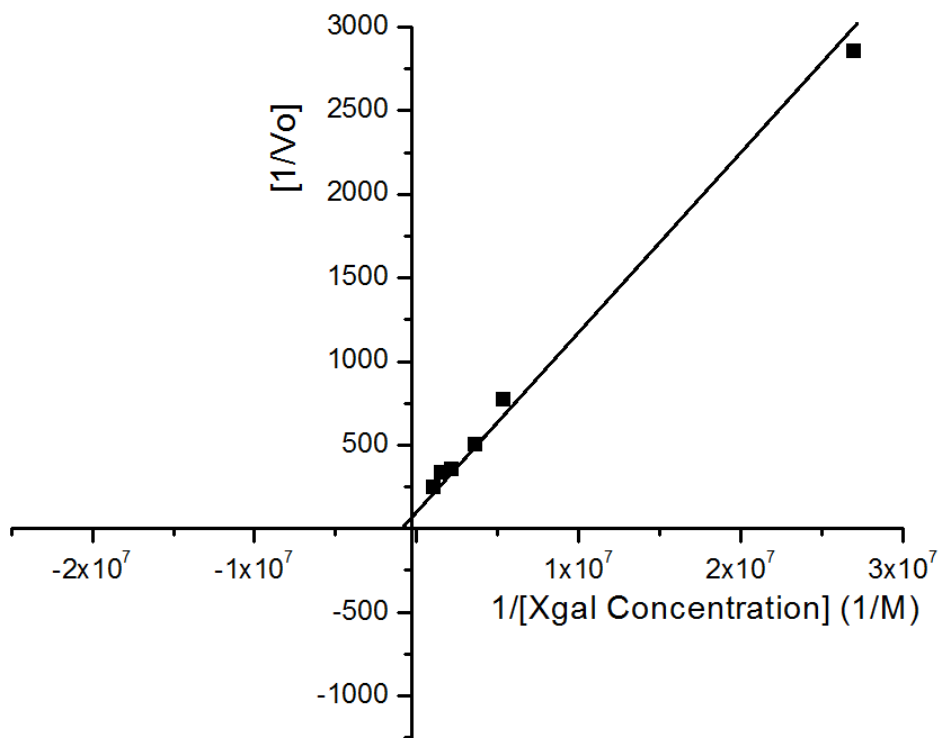


**Figure 4.11 Lineweaver-Burk plot of X-gal interactions with  $\beta$ -galactosidase at different concentrations. Analysis of the plot allowed the Michaelis constant of X-gal to be calculated where the trend line crosses the x-axis,  $k_m = 6.13 \times 10^{-7}$  M.**

Substrate	Michaelis Constant (mM)
X-gal	0.000613
p-Nitrophenyl- $\beta$ -D-galactoside	0.067
Phenyl- $\beta$ -D-galactoside	0.23
o-Nitrophenyl- $\beta$ -D-galactoside	0.30
Lactose	2.50

**Table 4.1 Comparison of known Michaelis constants calculated from substrate interaction with  $\beta$ -galactosidase. From comparison of other galactosides, X-gal with the lowest Michaelis constant correlates to it having the highest affinity for  $\beta$ -galactosidase.**

Comparison of known Michaelis constants calculated with substrate interaction with  $\beta$ -galactosidase shows that X-gal having the lowest Michaelis constant reflecting its high

affinity for the enzyme as seen in Table 4.1. The stabilizing effect of the solvent for X-gal analysis along with N,N-dimethylformamide were crucial factors in analysis with X-gal. Preliminary experiments without spectroscopic techniques revealed that X-gal without its reported solvent but rather just being solubilized in DMF produced no blue color in the presence of  $\beta$ -galactosidase. Other preliminary experiments showed that the blue color produced by the hydrolysis of the substrate is inhibited when solubilizing with a combination of organic solvents, DMF and MeOH. Experimentation to analyze the efficiency of X-gal at optimal pH conditions were inconclusive as the substrate was hydrolyzed immediately in acidic conditions before  $\beta$ -galactosidase was introduced into the system. A well-buffered system for the glycosidic substrate is therefore necessary to facilitate hydrolysis.

### **4.3 Surface chemistry of the $\beta$ -galactosidase Langmuir monolayer**

#### ***Surface pressure- and surface potential-area isotherms***

The interfacial properties and Langmuir monolayer behavior of  $\beta$ -galactosidase were investigated to optimize conditions for conformational and structural studies. Investigations of subphase salt concentration as well as spreading volume resulted in Langmuir monolayer formation with an enzyme concentration of 0.2 mg/mL and a spreading volume of 65  $\mu$ L on a pH 5.7, 0.1 M NaCl subphase. Conducted in triplicate, these conditions reproducibly demonstrated all necessary phases of a proper formation of a two-dimensional enzyme Langmuir monolayer.

Figure 4.12 shows combined surface pressure- and surface potential-area isotherms. The surface pressure-area isotherm calculated to a spreading amount of 0.02 nmol of enzyme at the air-water interface, a small amount which is necessary due to the large

molecular weight of the molecule. An initial zero in terms of surface pressure starting at  $80,000 \text{ \AA}^2\text{molecule}^{-1}$  is ideal correlating to a gaseous phase where the floating film at the hydrophobic-hydrophilic interface has little to no intermolecular interactions. Compression of the molecules at the surface results in an increase in surface pressure of the expanded film as described by a decrease in area per unit molecule. The liquid-expanded (L-E) phase of the monolayer occurring at  $65,000 \text{ \AA}^2\text{molecule}^{-1}$  is of interest because it shows that the molecules' degrees of freedom are being reduced as their orientation becomes uniform. The enzyme molecules continue to condense until  $\sim 35,000 \text{ \AA}^2\text{molecule}^{-1}$  when a steep increase in surface pressure is observed referred to as the liquid-condensed phase where the homogenous monolayer is analogous to a three-dimensional liquid. The higher surface pressure regions are of importance because of the high tension, 30-35 mN/m, found in biological membranes<sup>42,43</sup> where molecules have the least amount of compressibility. The final phase observed in a well-ordered monolayer is the collapse occurring around  $22,000 \text{ \AA}^2\text{molecule}^{-1}$  where the molecules are so closely packed at an absolute minimum area that they begin to form multiple layers along with molecules moving into the subphase or away from the interface. Extrapolating the surface pressure-area curve during the steepest part of the isotherm, typically during the liquid-condensed phase, down to a zero surface pressure allows researchers to determine the condition of the monolayer in a closely packed state. The Langmuir monolayer formed from  $\beta$ -galactosidase has a limiting molecular area of  $42,000 \text{ \AA}^2\text{molecule}^{-1}$ .

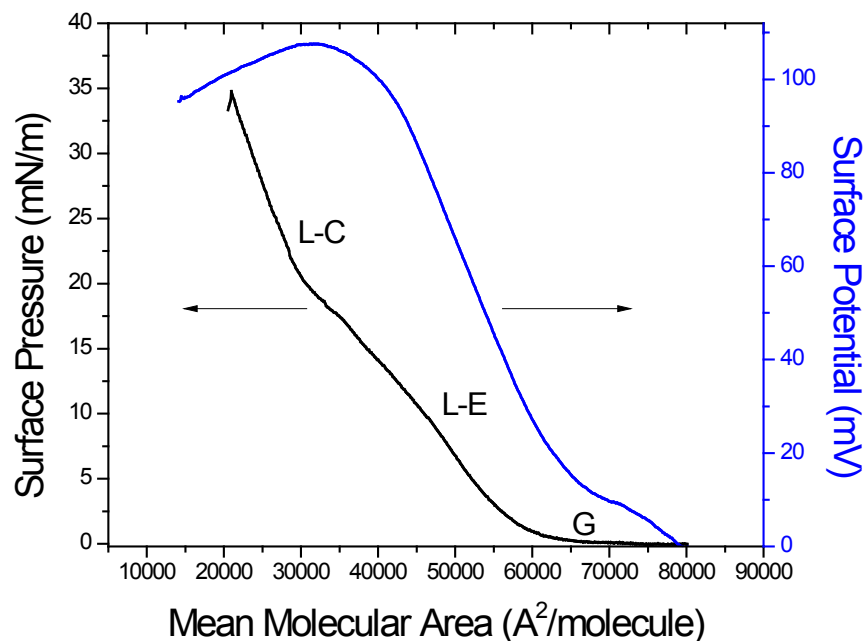


**Figure 4.12 Surface pressure-area and surface potential-area isotherms for 0.02 nmol  $\beta$ -galactosidase spread on a pH 5.7, 0.1 M NaCl subphase.**

In conjunction with surface pressure, surface potential-area isotherms as previously discussed reveal the molecular interactions occurring before and during any type of phase change of the monolayer as seen during compression. These changes in surface potential can be correlated with phase changes in the monolayer as the minimum cross-sectional area per molecule at the air-water interface decreases. In the case of  $\beta$ -galactosidase, the surface potential is most influenced by electrostatic as well as coulombic interactions due to the large surface area and difference of charge throughout the molecule by the amino acid content. Figure 4.12 correlates the two types of monolayer measurements by showing even during the initial gaseous phase, there is an immediate increase in surface potential at 80,000  $\text{\AA}^2/\text{molecule}^{-1}$ .

A kink in surface potential is observed as the monolayer begins to move into a liquid-expanded phase and as the monolayer compression transitions into a liquid-condensed



phase, again a change in surface potential is observed. At a maximum voltage of 108 mV, the surface potential corresponds to a close packing structure of the enzyme molecules at the beginning of the liquid condensed phase. When compared, the two methods seem slightly disjointed which is explained by the difference in detected dipole interactions compared to hydrophobic interactions. Surface potential is considered more sensitive in measuring these changes since they occur at larger intermolecular distances compared to the distance needed for hydrophobic interaction.

#### ***Compression-decompression cycles and stability measurements of the $\beta$ -galactosidase Langmuir monolayer***

The ability of a monolayer to be stable for long time periods is necessary in order to perform certain *in situ* experimentation such as IRRAS therefore compression-decompression cycles are conducted which reveal the extent of analyte which is being lost to desorption from the interface into the subphase, also known as hysteresis. Once a stable and reproducible monolayer was formed, these cycles reveal that when compressed to 10 mN/m in Figure 4.13A, there is a small hysteresis because a stable monolayer has not yet been formed. Although only 4% of the initial isotherm is lost upon comparison of the first and last cycle 20 and 30 mN/m, in Figures 4.13 B and C, only show hysteresis loss of 1 and 2%, respectively. Reorganization of the molecules at the interface shows that under these experimental conditions, the salt subphase renders the  $\beta$ -galactosidase molecules partially insoluble and good reversibility of the isotherm shows that there is little aggregate formation at the interface as well.<sup>114</sup>

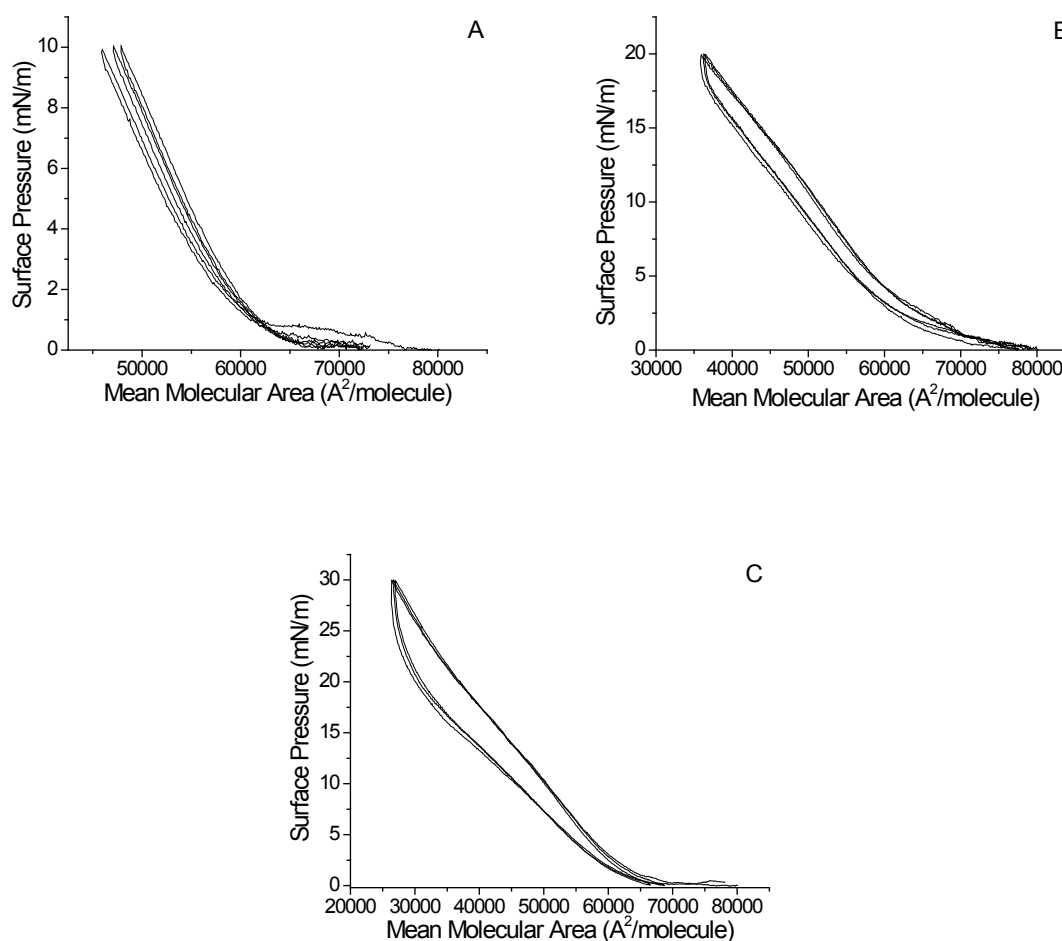


**Figure 4.13** Compression-decompression cycles for the 0.02 nmol  $\beta$ -galactosidase Langmuir monolayer on a 0.1 M NaCl subphase up to (A) 10, (B) 20 and (C) 30 mN/m.

The excellent stability of the enzyme monolayer held at a surface pressure of 20 mN/m for over a 90 min time period in Figure 4.14A shows an approximate change in area per molecule to be 18%. Ideal for future experimentation, the one-molecule-thick monolayer of  $\beta$ -galactosidase molecules can be analyzed at this point during compression as it is transitioning between the liquid-expanded and liquid-condensed phases. Figure 4.14B shows that when holding the monolayer at a higher surface pressure of 30 mN/m, a 20% shift in area per molecule occurs over the first 30 min, after which the monolayer collapses into multiple layers. The instability of the monolayer at this point in

compression is evident by the early collapse showing that this surface pressure cannot be used for time dependent measurements.

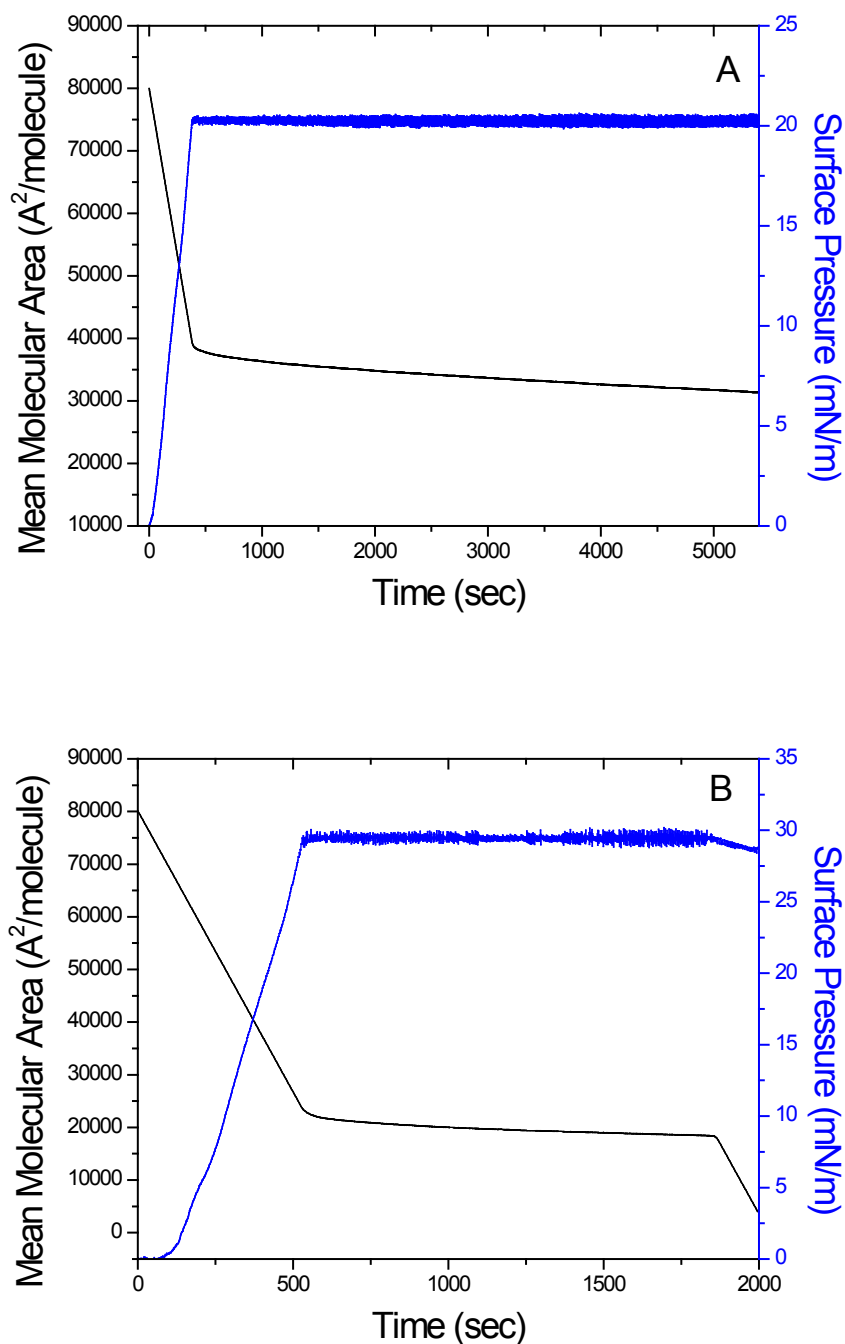


**Figure 4.14** Stability measurements which shows over an extended time period if the  $\beta$ -galactosidase monolayer can stay at the air-water interface when compressed to higher surface pressures of (A) 20 and (B) 30  $\text{mN/m}$ .

#### 4.4 Conformational studies of the $\beta$ -galactosidase Langmuir monolayer using IRRAS

##### *Effect of pH on the limiting molecular area*

The limiting molecular area of the  $\beta$ -galactosidase Langmuir monolayer describes the minimum cross-sectional area per molecule. This value can however change with environmental conditions, namely the subphase pH. As the extrapolated value for the limiting molecular area is shifted due to these changes, the molecular structure and conformation can be analyzed at the air-water interface. Changes in pH can affect the conformation of an enzyme by destabilizing certain vital components throughout the molecule. Figure 4.15 shows the effect of pH on the  $\beta$ -galactosidase Langmuir monolayer by adjusting the subphase pH while keeping the salt concentration constant at 0.1 M NaCl. The isotherm initially was obtained on a subphase of pH 5.7 which is close to the isoelectric point of the enzyme, 4.6.

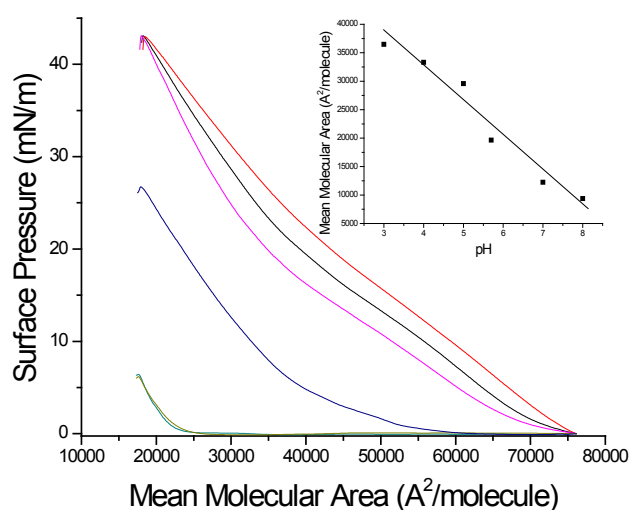


**Figure 4.15** The shift of the  $\beta$ -galactosidase isotherm to a more expanded monolayer as the subphase pH is decreased. (Inset) Analysis of the decrease in mean molecular area as a function of increasing subphase pH at 20 mN/m showing a linear trend,  $y = -5972.8x + 55994$ ,  $R^2 = 0.9591$ .

Around this pH, the charges resulting from functional groups that comprise the enzyme cancel out to a neutral charge. Decreasing the pH increases the mean molecular area of the enzyme resulting in a more expanded monolayer upon compression due to a greater degree of electrostatic repulsion. This type of repulsion is expected since the overall negative charge of the enzyme based on the amino acid composition will be protonated therefore instead of the molecules being closely packed, the molecules are more spread out at the interface. These results are interesting when correlated with the UV-vis absorption and fluorescence spectroscopy of the enzyme in solution at different pH. Figure 4.3, which show the change in UV-vis over time when pH of the solution is varied only showed an aggregation of monomers at pH 4, near the enzyme pI of 4.6. Possibly at the air-water interface there is an expanded monolayer possibly due to the aggregation of these monomers. Fluorescence spectroscopy of the enzyme in solution at different pH shown in Figure 4.8 does not correlate to these results due to the consistent quenching effect seen at a variety of pH. CD analysis of the secondary structure content of the enzyme solution when the pH is manipulated as seen in Figure 4.4 shows that a decrease in pH results in a larger  $\beta$ -sheet content. These CD results correlate well with the results of pH change at the air-water interface and are the main cause of an expanded monolayer evidenced by the shift in limiting molecular area is due to this content rise. Increasing the pH away from the isoelectric point reduces the mean molecular area; also an expected result from the enzyme monolayer since the basic subphase solubilizes the enzyme and hinders monolayer formation which can be correlated with a decrease in  $\beta$ -sheet content. Studies past a subphase of pH 8 resulted in no isotherm being produced which shows that solubilizing effects of the subphase cause the molecules to be expelled into the subphase

before any type of monolayer can be formed. A plot of the mean molecular areas analyzed at 25 mN/m show that there is a trend with a decreasing area as a function of increasing pH.

### ***Infrared absorption-reflection spectroscopy of the native enzyme***

Previously, FTIR research of  $\beta$ -galactosidase was conducted in the bulk solution phase at pH 7.0 which calculated the content of  $\beta$ -sheet and  $\alpha$ -helix to be 40 and 35%, respectively.<sup>31</sup> IRRAS can have positive and negative bands primarily depending on the Brewster angle of water compared to the angle of incident light as well as the polarization of incident light. The two polarizations of light used to study the  $\beta$ -galactosidase Langmuir monolayer differ by the electric vector oscillates in the plane of incidence and perpendicular to that plane for p-polarization and s-polarization light, respectively. Presented in Figure 4.16A,B are the p- and s-polarization IRRAS spectra of the enzyme monolayer collected at different surface pressures during compression at a 40° angle of incidence which had the highest signal-to-noise ratio. During compression, no change in band position and no disappearance of bands reflect no change in the secondary structure. Intensification of signal is solely due to the increase in surface density of enzyme molecules as the unit area is decreased. The sensitivity of the spectra obtained using p-polarized light made it ideal for assigning band positions to the secondary structure and group vibrations.

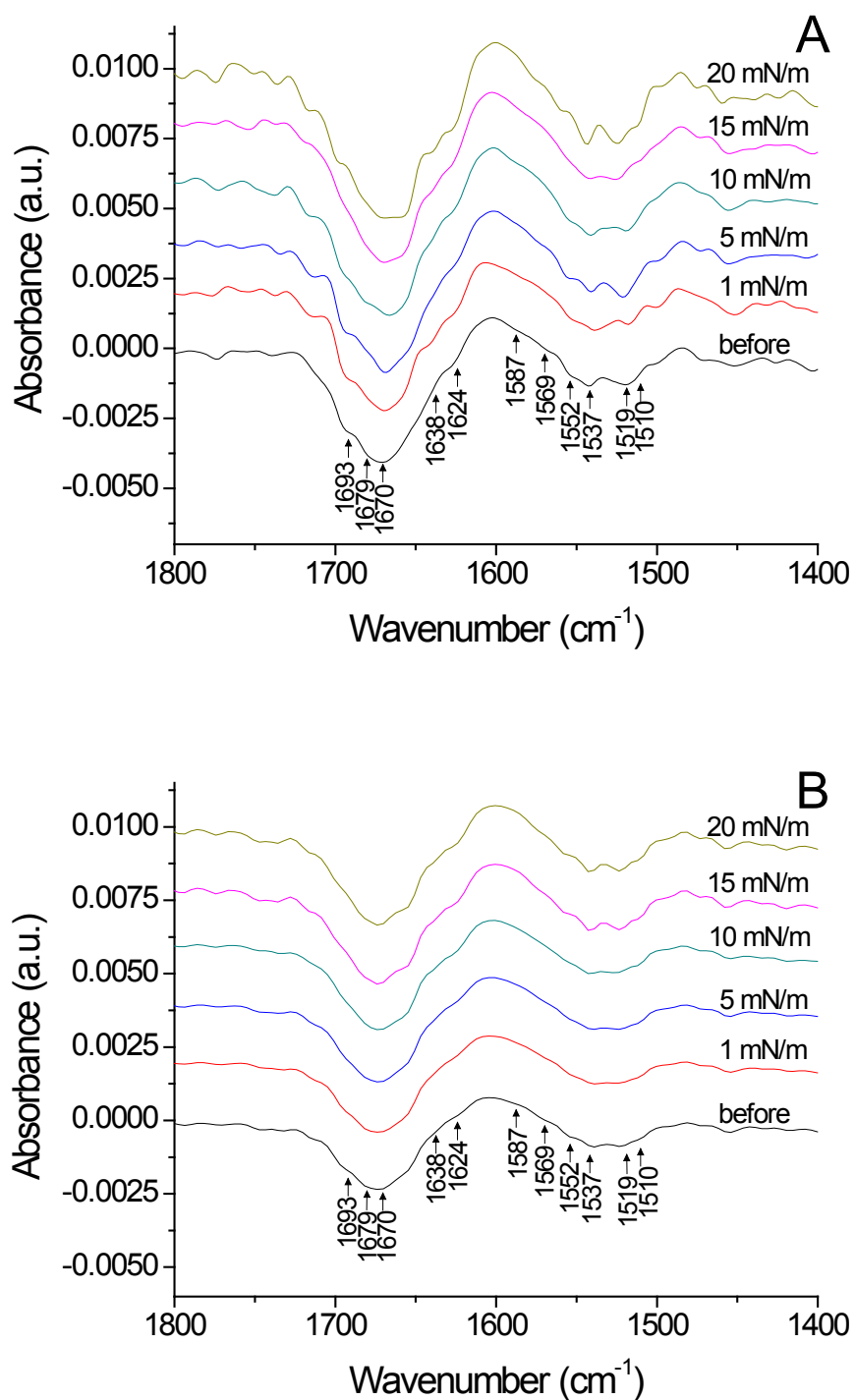


Figure 4.16 IRRAS spectra for the 0.02 nmol  $\beta$ -galactosidase Langmuir monolayer spread on a pH 5.7, 0.1 M NaCl and irradiated with (A) p-polarized light and (B) s-polarized light at a  $40^\circ$  angle with increasing surface pressure.

Band assignment in a  $\beta$ -sheet dominated structure shows the secondary structure has strong absorbance in the amide I region (1700-1600  $\text{cm}^{-1}$ ). Table 4.2 lists the major band position wavenumbers predominantly featured in Figure 4.16A which correspond to antiparallel  $\beta$ -sheet at 1693 and 1638  $\text{cm}^{-1}$  and parallel  $\beta$ -sheets at 1679 and 1624  $\text{cm}^{-1}$ . Symmetric stretching from the carbonyl group of asparagines and glutamine can be attributed to position at 1679 and 1670  $\text{cm}^{-1}$ , respectively, which are not involved in hydrogen bonding and are sterically constrained. The amide II region (1600-1500  $\text{cm}^{-1}$ ) shows mostly  $\alpha$ -helix content at band positions of 1552 and 1537  $\text{cm}^{-1}$  as well as  $\beta$ -sheet content at 1519  $\text{cm}^{-1}$ . Symmetric stretching from aspartic acid and glutamic acid can be attributed to the bands occurring at 1587 and 1569  $\text{cm}^{-1}$ , respectively. The tyrosine content in  $\beta$ -galactosidase shows ring vibration at 1519  $\text{cm}^{-1}$  as well as  $\nu(\text{CN})$  coupled to  $\delta(\text{CH})$  and  $\delta(\text{NH})$  bending modes at 1510  $\text{cm}^{-1}$ . The abundance of  $\beta$ -sheet content in the IRRAS spectra is expected for the molecule however, an increase in  $\beta$ -sheet absorbance can also be attributed to the experimentation conditions conducted at the air-water interface which increases the amount of intermolecular interactions between nearby  $\alpha$ -helix and  $\beta$ -turn secondary structures.

<b>amide I (1700 – 1600 <math>\text{cm}^{-1}</math>)</b>		
band position ( $\text{cm}^{-1}$ )	group vibration	secondary structure
1693		Antiparallel $\beta$ -sheet
1679	Asparagine $\nu(\text{CO})$	$\beta$ -turn and transition dipole coupling
1670	Glutamine $\nu(\text{CO})$ (not involved in H-bonding and sterically constrained)	$\beta$ -sheet
1638		Antiparallel $\beta$ -sheet
1624		Parallel $\beta$ -sheet



amide II (1600–1500 cm <sup>-1</sup> )		
band position (cm <sup>-1</sup> )	group vibration	secondary structure
1587	Aspartic acid $\nu(\text{CO})$	
1569	Glutamic acid $\nu(\text{CO})$	
1552		$\alpha$ -helix
1537		$\alpha$ -helix
1519	Tyrosine ring -OH vibrations	$\beta$ -sheet
1510	Tyrosine $\nu(\text{CN})$	

**Table 4.2 IR band assignments using IRRAS at the air-water interface.**

### *Effect of pH on the native enzyme*

The effect of pH on the enzyme monolayer shows that lowering the pH of the subphase expands the monolayer resulting in a larger mean molecular area due mostly to a shift in secondary structure and electrostatic repulsion. Figure 4.17A shows the IRRAS trends seen in terms of major band positions when altering the subphase pH when irradiated with p-polarized incident light at a 40° angle before compression at 0 mN/m. The amide I band  $\beta$ -sheet content seen at positions 1624 and 1638 cm<sup>-1</sup> increase in intensity as the pH of the subphase decreases while the  $\alpha$ -helix absorbing at 1693 cm<sup>-1</sup> decreases slightly. Correlated to the secondary structure CD analysis in Figure 4.4 of pH manipulation while the enzyme is in solution, the low  $\alpha$ -helix content also decreases with a decrease in pH while the  $\beta$ -sheet content increases. With these results in accord, observation of band positions 1670 and 1679 cm<sup>-1</sup>, also associated with  $\beta$ -sheet content, show these bands can be attributed to polar, uncharged amino acid bond stretching which decreases with the subphase pH due to repulsion.

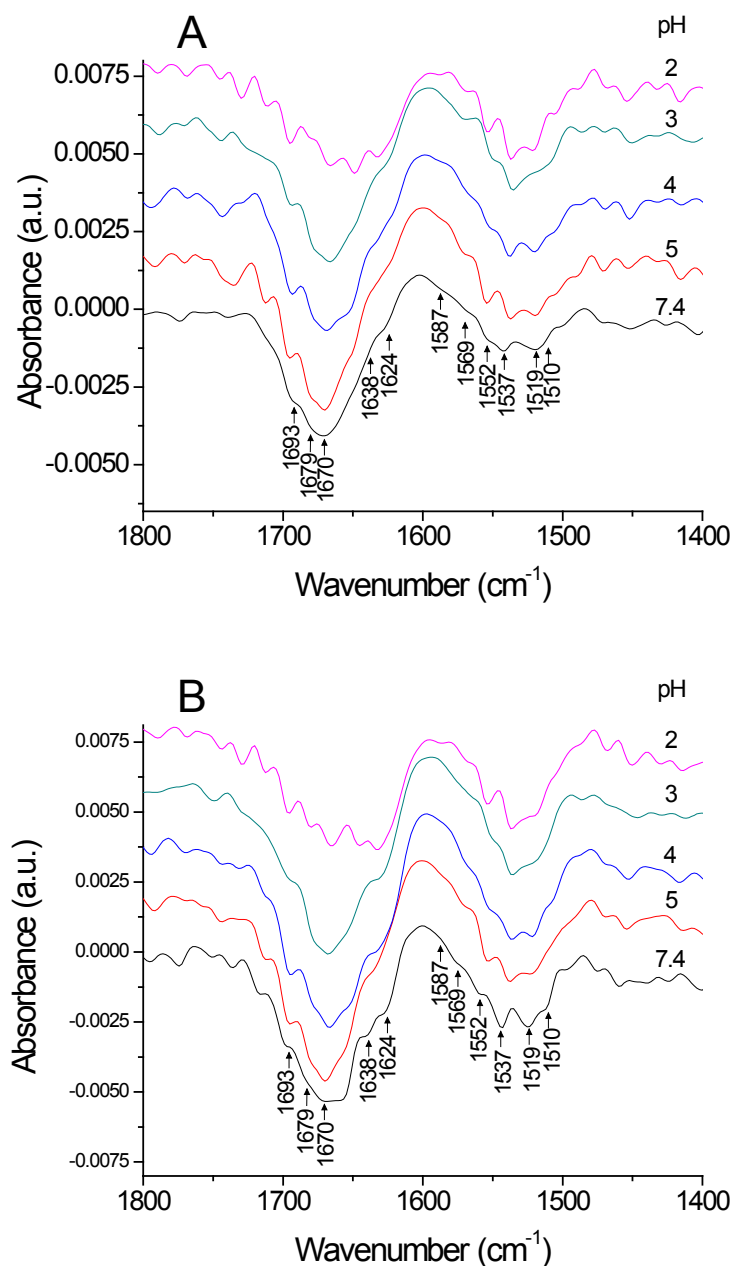


**Figure 4.17** The trends of major IRRAS wavenumbers in the amide I and II band region with decreasing subphase pH which show the enzyme monolayer at a surface pressure of (A) 0 and (B) 20 mN/m irradiated with p-polarized light at a 40° angle.

Before the collapse of the monolayer at a surface pressure of 20 mN/m the trends of major band positions seen in Figure 4.17B show similar results as at 0 mN/m. The stable monolayer produced by  $\beta$ -galactosidase shows an increase in  $\beta$ -sheet content at band positions 1624 and 1638 cm<sup>-1</sup> and the decrease in  $\alpha$ -helix content is more evident at the

higher surface pressure as the pH is decreased. Band positions at 1670 and 1679  $\text{cm}^{-1}$  show good correlated with the enzyme before monolayer compression which show an overall decrease with the pH.

The amide II band shows similar trends in terms of secondary structure at 0 mN/m in Figure 4.17A which increases band absorbance while lowering the subphase pH at 1519  $\text{cm}^{-1}$  correlating to an expanding with  $\beta$ -sheet content. Unexpectedly, the  $\alpha$ -helix content correlating to band positions at 1537 and 1552  $\text{cm}^{-1}$  increase with a decrease in subphase pH. Comparison to the monolayer at 20 mN/m shows in Figure 4.17B that the molecules are closely packed especially when on a very acidic subphase evidenced by a rise in all band position intensity.

#### **4.5 *In situ* photophysical properties of the $\beta$ -galactosidase Langmuir monolayer**

##### ***UV-vis absorption and fluorescence spectroscopy***

The UV-vis absorption and fluorescence spectroscopy of the  $\beta$ -galactosidase Langmuir monolayer was conducted on a 0.1 M NaCl subphase with a larger spreading volume of enzyme, 150  $\mu\text{L}$ , due to the larger trough area. The high content of tryptophan, 39 residues, and tyrosine, 31 residues, present in the amino acid content of the monomer give  $\beta$ -galactosidase a large molar absorptivity and make it ideal to analyze spectroscopically *in situ*. Absorbance of UV-vis light in aqueous solution at pH 6 by tryptophan residues at  $\lambda_{\text{max}} = 280 \text{ nm}$ ,  $\epsilon = 3.6 \times 10^4 \text{ L mol}^{-1}\text{cm}^{-1}$  dominates the absorbance spectra due to the absorbance of tyrosine at  $\lambda_{\text{max}} = 275 \text{ nm}$ ,  $\epsilon = 1.4 \times 10^3 \text{ L mol}^{-1}\text{cm}^{-1}$ .<sup>50,51</sup>

Analysis of the UV-vis spectrum of  $\beta$ -galactosidase at the air-water interface as it was compressed is seen in Figure 4.18. An inset plot of the intensity at  $\lambda_{\text{max}} = 282 \text{ nm}$  does

not increase immediately upon compression as the molecules are still in a film. The linear increase in absorbance is observed as a function of the surface pressure up to 20 mN/m which is associated with the liquid-expanded region of the isotherm seen in Figure 4.12. As compression continues from 25 mN/m, higher absorbance is correlated with the liquid condensed region up to the collapse of the monolayer after 35 mN/m. The increase in tryptophan absorbance reveals that the enzyme is not solubilized into the subphase but rather retained at the interface throughout the compression of the monolayer. If the monolayer were unstable, the absorbance intensity would not steadily increase but rather reach a plateau as molecules are expelled into the subphase.

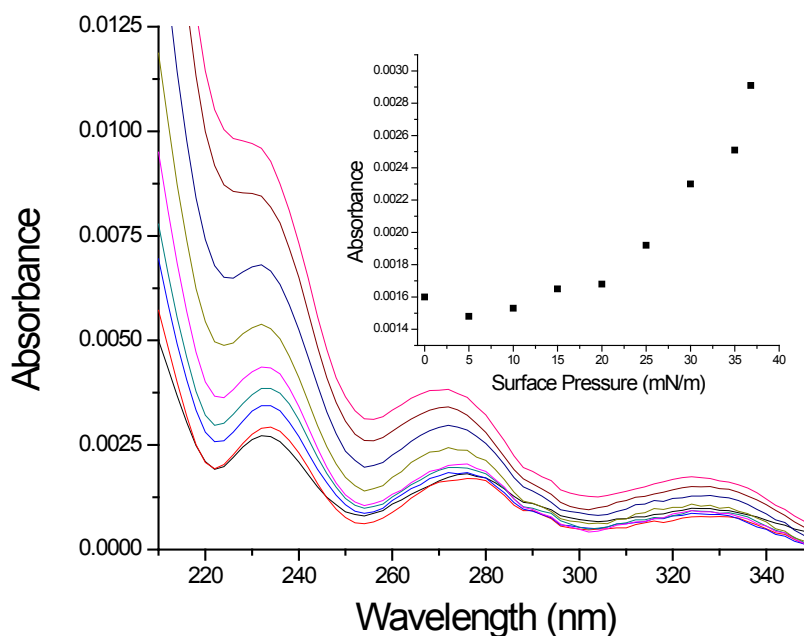


**Figure 4.18** UV-vis absorption at the air-water interface of the  $\beta$ -galactosidase Langmuir monolayer from 0.02 nmol enzyme spread on a pH 5.7, 0.1 M NaCl subphase. (Inset) Analysis of the maximum absorbance,  $\lambda_{\text{max}} = 282$  nm, as a function of increasing surface pressure.

*In situ* fluorescence spectroscopy is also dominated by the presence of tryptophan in  $\beta$ -galactosidase. With an excitation of 284 nm and analysis at 354 nm, Figure 4.19 shows

the increase of emission intensity throughout the compression of the monolayer. Scattering light is initially observed at 420 nm when the monolayer is in its gaseous phase as also seen by no increase in tryptophan emission intensity in the inset. At a surface pressure higher than 20 mN/m, there is a sudden increase in intensity as the monolayer transitions to the liquid-condensed phase which corresponds with observation obtained from the absorbance data at the same surface pressures.

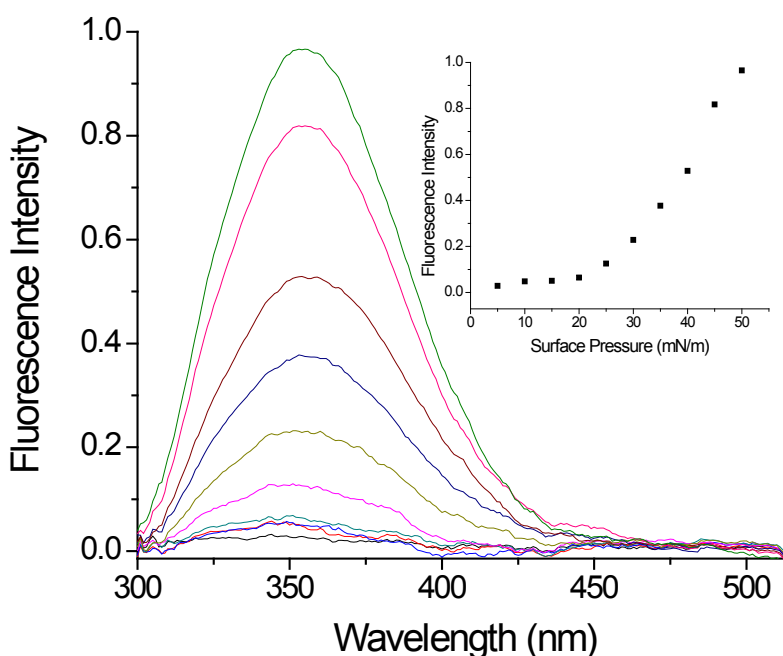


**Figure 4.19** Fluorescence spectra at the air-water interface of the  $\beta$ -galactosidase Langmuir monolayer from 0.02 nmol enzyme spread on a pH 5.7, 0.1 M NaCl subphase with scattering light at 420 nm subtracted. (Inset) Analysis of the maximum emission,  $\lambda_{em} = 354$  nm, as a function of increasing surface pressure.

#### 4.6 Conclusion

In summary,  $\beta$ -galactosidase has a high content of tryptophan residues which makes the large molecule easily possible to analyze with spectroscopic techniques. UV-vis absorption shows that at a pH near the enzymatic pI there is an increase in concentration of  $\beta$ -galactosidase molecules related to the aggregation of monomers to form the tetramer

in solution. Circular dichroism showed no change in the secondary structure after the fluorescence quenching however in acidic conditions the  $\beta$ -sheet content increased while the  $\alpha$ -helix content decreased. Basic conditions analyzed by circular dichroism showed an opposite effect in terms of secondary structure content. Fluorescence emission from the tryptophan residues shows that a consistent reduction in emission intensity is followed by a minor recovery of intensity given a waiting time between excitation of the molecule. The emission quenching is unaffected by thermal denaturation as well as environmental pH changes during the experimentation concluding that a non-radiative quenching process is the cause of the decrease of the intensity of emission over time. Studies involving substrate hydrolysis by  $\beta$ -galactosidase were used to calculate the Michaelis constant of X-gal ( $k_m = 6.13 \times 10^{-7}$  M).

$\beta$ -galactosidase reproducibly forms a stable Langmuir monolayer resulting in a limiting molecular area of  $42,000 \text{ \AA}^2 \text{ molecule}^{-1}$  with no formation of aggregates and little hysteresis into the NaCl subphase. *In situ* photophysical properties of the monolayer utilize the high content of tryptophan residues in the enzyme to confirm, at a surface pressure of 20 mN/m, that a closely packed monolayer begins to form by observing the increase in absorbance and fluorescence intensity of emission. The monolayer expands when spread on a subphase with a very acidic pH and does not form a monolayer when the pH rises beyond seven. IRRAS of the monolayer confirms a large  $\beta$ -sheet content which increases in vibrational amplitude as the pH of the subphase is lowered resulting in an expanded monolayer with large amounts of intramolecular repulsion at the air-water interface.

## Chapter 5

### Characterization of Quantum Dots

#### Background

Colloidal dispersions differ from solutions and suspensions by the several factors such as appearance, particle size, light interaction as well as sedimentation. A colloidal system, as in the case of semiconductor quantum dots, are nanometer sized solid particles which form a homogenous dispersion similar to a solution. The difference however is that instead of light passing through with no reflection, the colloidal quantum dots disperse the light through the Tyndall effect which scatters blue light much more strongly than red light. Synthesis of these particles originally took place in an aqueous medium<sup>115</sup> however the heterogeneous nature of the particle sizes in the samples made it difficult to correlate properties. Monodispersed quantum dots were developed through a method involving high temperatures and organic solvents which was deemed the hot injection method where quantum dot size selection was temperature driven. Accomplished by controlling the temperature (270-320°C) of precursor above that of the nucleation threshold, injection of reagents which immediately reacted with the precursor resulted in instantaneous nucleation. The monodispersity of the resulting quantum dot sample was rapidly cooled after a desired size was synthesized. With advancements into the methodology behind quantum dot synthesis, procedures with greater selection of particle size, safer chemicals and better handling of growth kinetics have given the field of quantum dots great potential.<sup>96,116-118</sup>

QDs are normally modified after synthesis to improve their optical properties because the highly defective core surface degrades the optical properties. The concept of a core/shell

system was introduced to control mainly the optical properties and stability of the nanoparticles<sup>119-121</sup> by adding a second semiconductor coating to the existing core. CdSe, a common core as described previously is made by coupling a II and VI group element in order to facilitate the movement of electrons across the band gap. The addition of ZnS<sup>119</sup> passivates the surface nonradiative recombination sites thereby promoting the stability and optical properties of the quantum dot in terms of the electron-hole created by movement of electrons. With this barrier in place, the model which defines the energy gap as being correlated with the size of the nanoparticle can make the assumption that the potential energy outside of the quantum dot is infinite, thereby restricting the electron-hole to the confines of the interior of the nanoparticle. In addition to these properties, overcoating of the core increases the size of the quantum dot by no more than the radial size of the coating itself meaning that since this process occurs at much lower temperatures, nucleation does not occur.<sup>120</sup>

## **5.1 Characterization by spectroscopy and microscopy**

### ***UV-vis absorption spectroscopy***

The approximate size of the quantum dot core is ascertained by UV-vis absorption spectroscopy of the CdSe dispersed in chloroform after size-selective methanol precipitation which also removes any excess TOPO ligand from the nucleation and storage process.<sup>122</sup> Calculations on the size dependence of the extinction coefficient per mole of quantum dots were done using the first excitonic absorption peak. Absorption spectroscopy as seen in Figure 5.1 shows the original CdSe core as well as three different types of quantum dots produced from surface modification of the core.



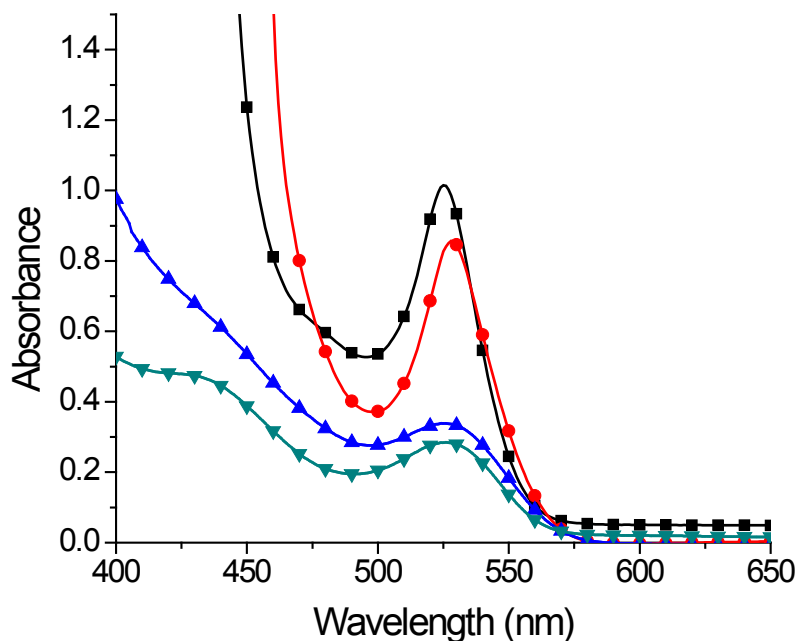


**Figure 5.1** UV-vis absorption spectra of 13.4  $\mu\text{M}$  CdSe-TOPO (■), CdSe(ZnS)-TOPO (●), CdSe(ZnS)-DHLA (▲) and CdSe(ZnS)-MPS (▼) dispersions with maximum absorbance at 525, 528, 527, 526 nm, respectively, and a core size of 2.63 nm.

The empirical fitting function of literature experimentation<sup>123</sup> shows that the diameter of the CdSe core can be calculated from the sharp, first exciton absorption peak:

$$\begin{aligned} \text{Diameter} = & (1.6122 \cdot 10^{-9})(\lambda_{\text{abs}}^4) - (2.6575 \cdot 10^{-6})(\lambda_{\text{abs}}^3) \\ & + (1.6242 \cdot 10^{-3})(\lambda_{\text{abs}}^2) - (0.4277)(\lambda_{\text{abs}}) + 41.57 \end{aligned} \quad (5.1)$$

where the diameter,  $D$  (nm), correlates to a core size of 2.63 nm at a wavelength of 525 nm.<sup>124,125</sup>

The tunable size of CdSe QDs has shown that with a change in diameter, this extinction coefficient at  $\lambda_{\text{max}}$  will also change.<sup>123-126</sup> Correlation between these experimental values and literature data has previously shown that the theoretical  $\epsilon$  values tend to follow a quadratic dependence which suggests the tunable size of the nanoparticles is directly

correlated to an increase in the molar absorptivity as the surface area of the QD increases<sup>127</sup> using the following equation:

$$\varepsilon = (5857)Diameter^{2.65} \quad (5.2)$$

which correlates to a molar absorptivity of 75,960 M<sup>-1</sup>cm<sup>-1</sup> for the core.

It is important to mention the effect of ligands on the absorbance and detectable extinction coefficients of quantum dots. As reported in literature, synthetic methods which coat the quantum dot core with a surface passivating shell or exchange the ligand to make the quantum dots water soluble will not alter the absorbance maximum within experimental error. Mainly due to the routes which adjust the quantum dot are below the temperature required for nucleation, these results can be seen in Figure 5.1 which shows the absorbance peaks of the same quantum dots with the ZnS shell, DHLA ligand and MPS ligand all absorb at the same maximum. Also observable is the contrast between the sharp peaks of the core and core/shell opposed to the broad, reduced peaks when the ligand is exchanged. The size distribution effect arises from inhomogenous variability in the size of quantum dots as the ligands are exchanged. The surface of these nanoparticles is highly defective which without modification would have an adverse effect on the electrical and optical properties.<sup>72,81,82,128,129</sup>

### ***Fluorescence spectroscopy***

The innate optical properties of quantum dots produce a high intensity of luminescence in the green light spectra mainly due to their surface modification. As previously discussed, the addition of a shell to the outside of the core is to enhance the optical properties by stabilizing the excited state vibrational groups thereby producing a greater emission of photons. With the addition of the shell, a calculated 0.5 nm is added to the

radius and the fluorescence increases by more than tenfold as seen in Figure 5.2 with a small shift of intensity from 545 to 553 nm and a narrow size distribution evidenced by the 46 nm full width at half-maximum of the core/shell QD.

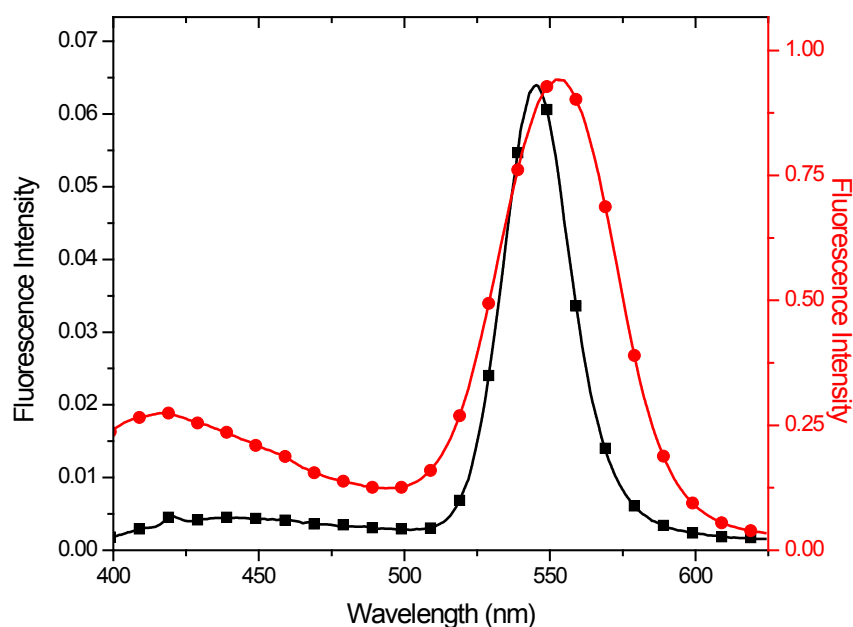


**Figure 5.2** Fluorescence spectra of CdSe-TOPO (■) and CdSe(ZnS)-TOPO (●) QDs excited at 373 nm with emission maxima at 545 and 553 nm, respectively. The QDs were monodispersed with FWHM of 30 and 46 nm, respectively. The addition of a ZnS shell to the CdSe core enhanced the optical properties by over tenfold.

Modification of the quantum dots with ligand exchange to produce the CdSe(ZnS)-DHLA and CdSe(ZnS)-MPS quantum dots are shown in Figure 5.3A and 5.3B, respectively. Having luminescence intensities at 556 nm, these two quantum dots show narrow size distributions however the intensity of luminescence for the hydrophilic stabilizing ligand shows a decrease due to the solvent medium compared to the other organic solvating agents.

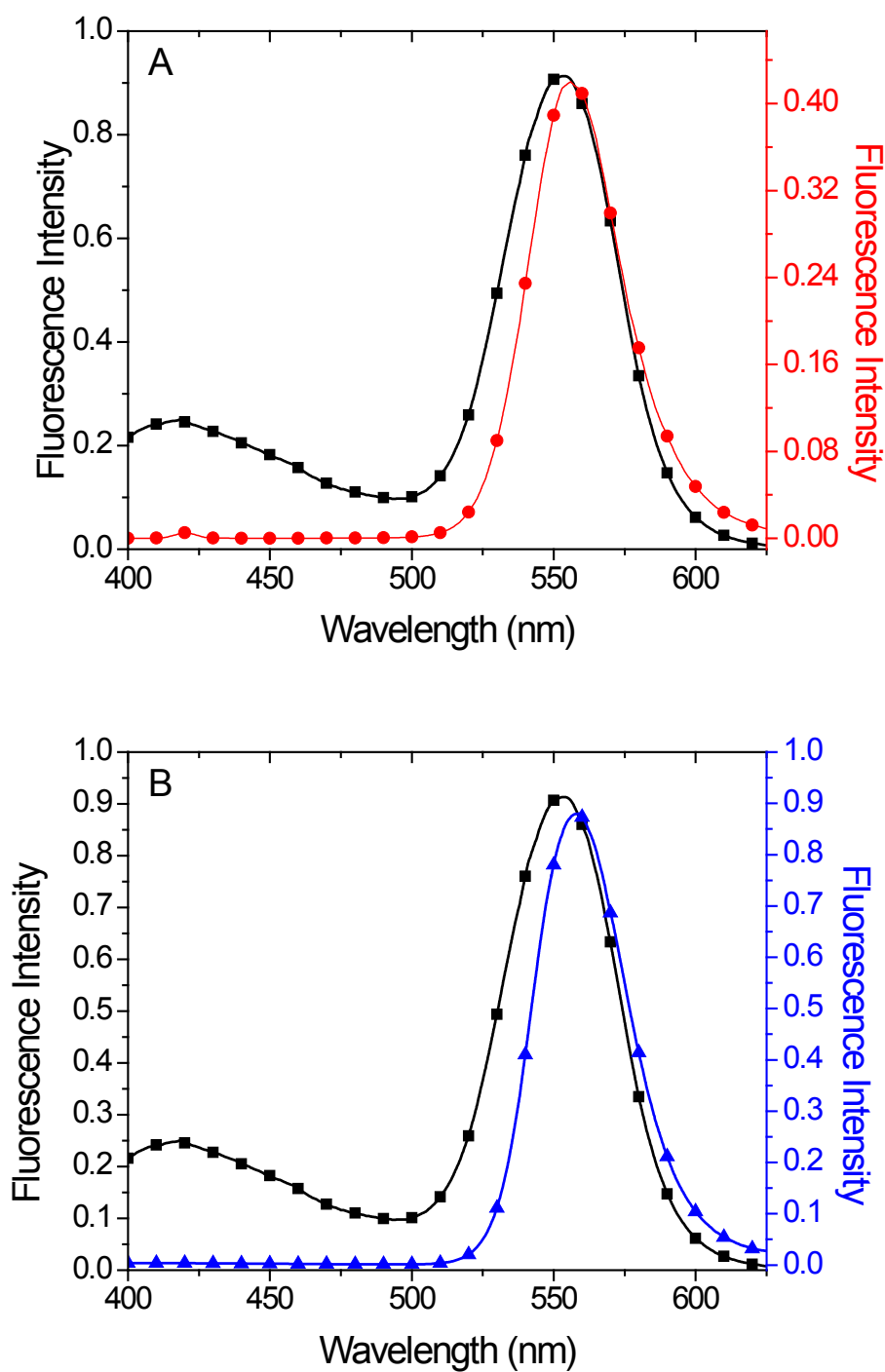


**Figure 5.3** Fluorescence spectra of CdSe(ZnS)-TOPO (■) compared to (A) CdSe(ZnS)-DHLA (●) and (B) CdSe(ZnS)-MPS (▲) QDs excited at 373 nm with emission maxima at 543, 556 and 556 nm, respectively, and excitation/emission slit widths of 3 nm. The QDs were monodispersed with FWHM of 46, 38 and 38 nm, respectively.

### ***Transmission Electron Microscopy***

The addition of a shell or exchange of ligand however undetectable by UV-vis methods does provide some modification to the size of the quantum dot. Seen in Figure 5.4A, the TEM image of the CdSe quantum dot has an average diameter of 3.71 nm and as reported in literature,<sup>130</sup> the TOPO ligand has a thickness of 0.7 nm however this is nonconductive therefore the TEM only shows the bare quantum dot therefore the diameter of the core is  $(2 \times 0.7 \text{ nm}) + 3.71 \text{ nm} = 5.11 \text{ nm}$ .

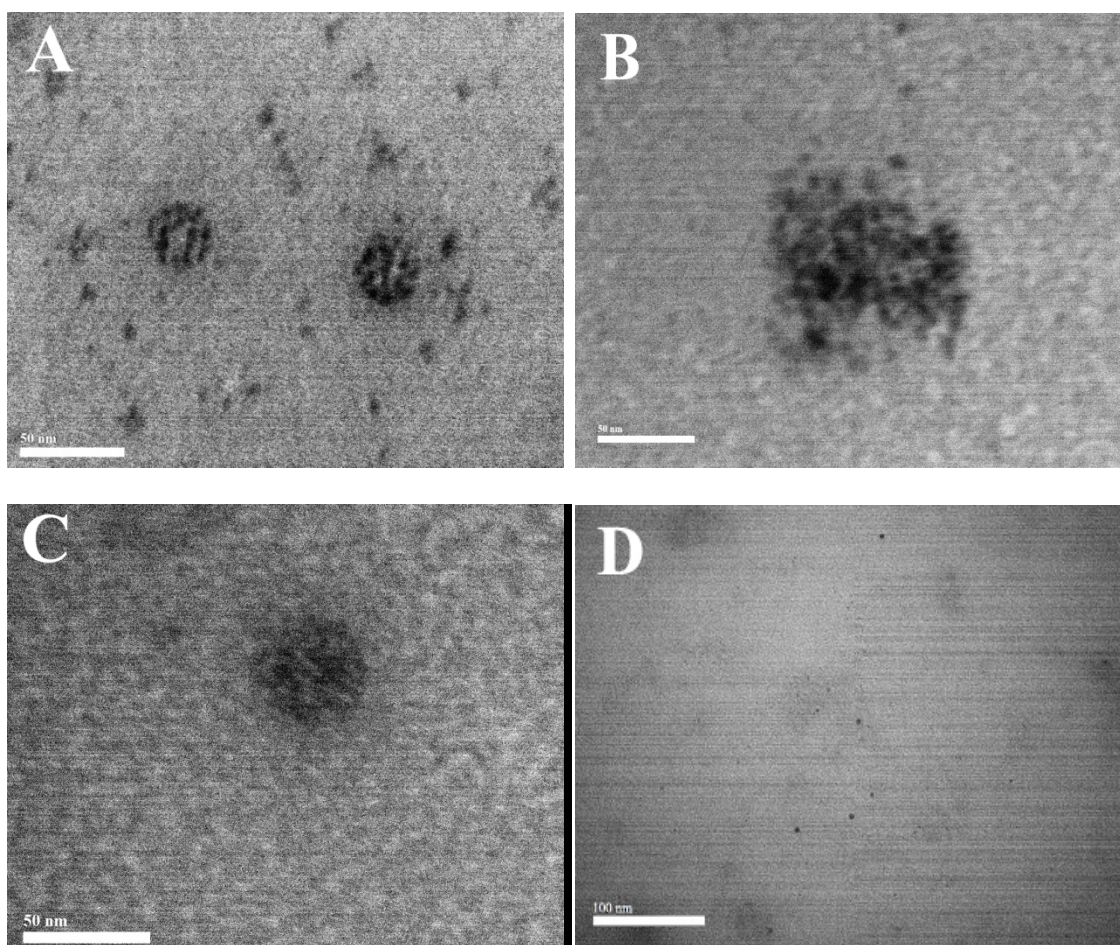


**Figure 5.4** TEM images of (A) CdSe-TOPO, (B) CdSe(ZnS)-TOPO, (C) CdSe(ZnS)-DHLLA and (D) CdSe(ZnS)-MPS dispersions 50, 50, 50 and 100 nm scale bars, respectively.

Addition of the ZnS shell in Figure 5.4B shows an even greater increase in the diameter to an average distribution value of 5.02 nm correlating to a quantum dot of 6.42 nm with the monolayer of TOPO. Calculated to add 1 nm to the size of the quantum dot, this diameter is within experimental values expected for the synthesis of monodispersed nanoparticles. Ligand exchange shows that the quantum dots also retain a larger size as seen in Figure 5.4C, however the larger ligand exchanged for DHLA shows a size distribution averaging 4.80 nm. MPS capped quantum dots on the other hand does not drastically change the size of the quantum, nor does the sample have a large quantity of nanoparticles available for imaging seen in Figure 5.4D which might be the cause of the average size being just above the core size at 3.74 nm. Self-assembly of quantum dots is the cause of a decrease in optical properties as well as formation of larger aggregates. As seen with TOPO, the quantum dots are inhomogeneous however DHLA and MPS ligand exchange produce symmetrical and monodispersed quantum dots. Possibly due to the interdigitation of the three long alkyl chains, these quantum dots irregularly branch into clusters and aggregates of uncontrollable size.

## **5.2 Surface chemistry of the QD Langmuir monolayer**

Previously reported have been the extensive results concerning quantum dots in 2D starting with their self-assembly as a result of size and ligand.<sup>72,131</sup> These studies have been conducted in order to establish the limiting nanoparticle area in conjunction with other established size determination measurements,<sup>82,132</sup> manipulate of the films, and control the interparticle distance.

### *CdSe-TOPO*

Literature shows<sup>133</sup> that quantum dots will form an organized local-hexagonal close packing upon compression of the monolayer and the behavior of this isotherm was also observed for many other QDs which is in line with the properties of colloidal nanoparticle Langmuir films. When at the air-water interface, QD are solubilized by the three alkyl chains of the innate ligand TOPO which is further stabilized by the phosphorus-oxygen bond providing a large dipole moment.<sup>122,134,135</sup> Seen in Figure 5.5 the Langmuir isotherm of the TOPO capped core CdSe quantum dot produced a stable isotherm with a limiting molecular area of 13,500 Å<sup>2</sup>/particle.

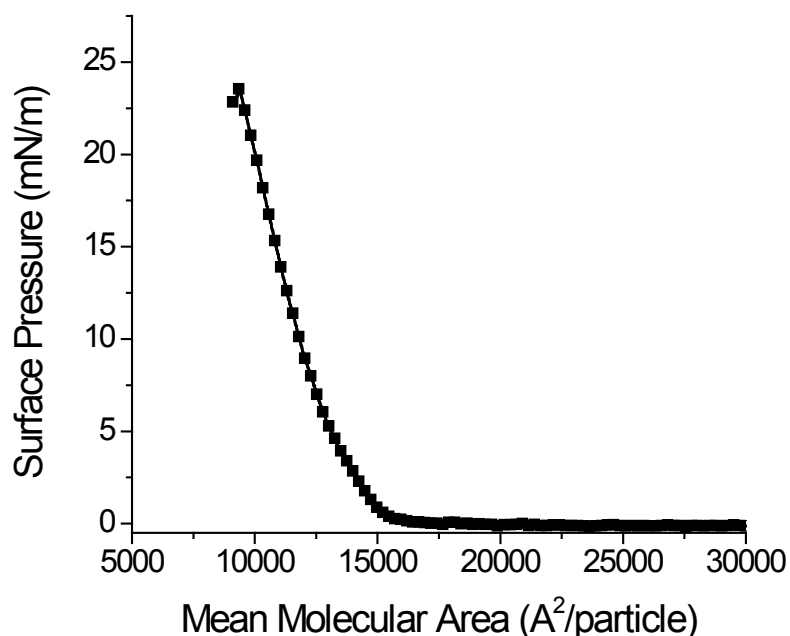


**Figure 5.5** Surface pressure-area isotherm of 0.06 nmol CdSe-TOPO QDs spread on a pH 5.7, water subphase with a limiting molecular area of 13,500 Å<sup>2</sup>/particle.

Freshly synthesized and purified in order to reduce three dimensional aggregates of the nanoparticles at the air-water interface, the TOPO capping stabilizes the nanoparticles

and doesn't penetrate into the quantum dots but rather forms a close-packed Langmuir monolayer on the surface.<sup>72</sup>

### ***CdSe(ZnS)-TOPO***

Previous studies<sup>129</sup> have been done on CdSe QDs which vary the surface ligand even further than just providing a comparison to TOPO. The chain lengths of the ligand surrounding the nanoparticles have been varied (C<sub>6</sub>SH to C<sub>18</sub>SH) as well to show that the QDs can form a stable Langmuir monolayer. The measure of stability has been confirmed by the collapse of these monolayers occurring at higher surface pressures above 25 mN/m. QD-C6 (QDs modified with hexane thiol), QD-C8, QD-C10 and QD-C12 showed similar limiting nanoparticle areas, when compared with pure QDs at approximately 500 Å<sup>2</sup>/nanoparticle. Ligand chain lengths longer than that, QD-C14 to QD-C18 have shown direct correlation to an increase in the limiting nanoparticle area with an increase in the alkane thiol chain length.<sup>129</sup>

The explanation for this behavior of varying ligand chain lengths arises from the role of the TOPO surface ligand on the QD itself. During preparation of the nanoparticles the solvating ligand allows the QDs to be soluble in many nonpolar, organic solvents. As a result when modifying the ligand to attach the varying chain lengths the TOPO is in part washed away but not completely. Actually, the modified QDs have a capping layer which is now a mixture of small amounts of TOPO and the alkane thiols. When analyzing the isotherms of these modified QDs, the limiting nanoparticle area which one observes is a function of the diameter of the QD. Since the diameter now includes the CdSe core along with double the length from the longest portion of ligand, one now sees that if a ligand length is comparable to TOPO then there should be little effect in the isotherm and



packing structure. The TOPO ligand is closest in length to the C12 molecule which is much greater in length than the C6 or even the C8. Therefore, the modified QDs (QD-C6 to QD-C10) are expected to have a limiting nanoparticle area similar to that of pure QDs which are surrounded by the innate TOPO ligand. When the length of the chain exceeds that of TOPO's length (QD-C12 to QD-C18), the modified QDs now present an increased limiting nanoparticle area when analyzing the isotherms and increase proportionality with the new capping layers. Measurements done by UV-vis absorption spectroscopy of the modified QDs also show a linear increase in  $\lambda_{\max}$  absorption with an increase in surface pressure as seen by all of the modified QDs (QD-C6 to QD-C18).

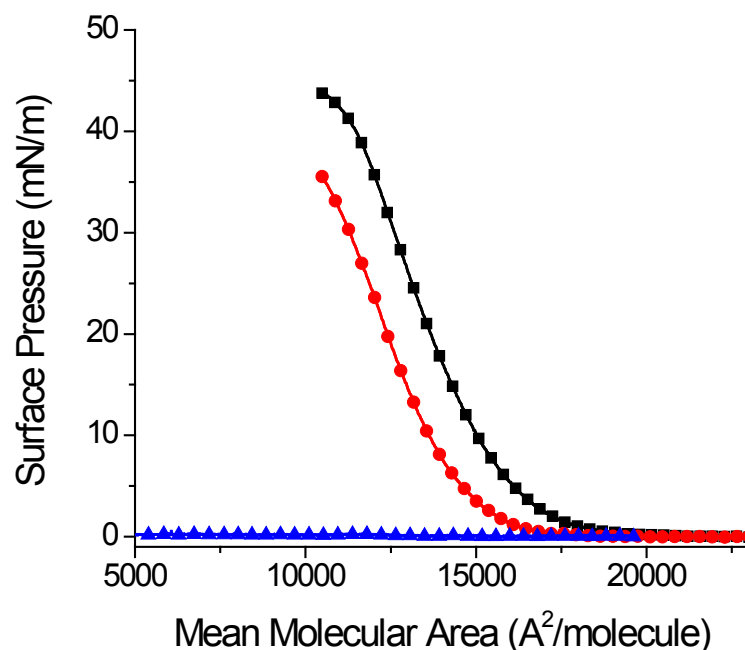


**Figure 5.6** Surface pressure-area isotherm of 0.06 nmol CdSe(ZnS)-TOPO QDs spread on a pH12 (■), 5.7 (●) and 2 (▲) subphase.

As seen in Figure 5.6, the isotherm of the CdSe(ZnS) QDs on three different pH is examined. The initial gaseous phase is seen in all three isotherms with the isotherm on pH 5.7 subphase shows an increase in limiting molecular area to 14,500 Å<sup>2</sup>/particle from

that of the core QD isotherm. This increase is expected due to the increase of particle size from the addition of the shell. When introduced to extreme pH, the quantum dot does not form an isotherm on an acidic subphase. Mostly likely due to the protonation of the surrounding ligand, the quantum dot precipitates into solution without being able to stabilize at the interface. In the case of an alkaline subphase, an increased limiting molecular area is seen correlating to a more closely packing structure at the interface with a limiting molecular area of  $15,700 \text{ \AA}^2/\text{particle}$ . The stability of the monolayer is seen by the high compressibility up to  $\sim 40 \text{ mN/m}$  before the collapse.

### ***CdSe(ZnS)-DHLA***

With the ability to produce highly tunable quantum dots with size dependent emissions, one drawback is that nonpolar, organic solvents are the only solvents able to disperse the nanoparticle due to the organic TOPO ligand. In the need for biocompatibility, water soluble quantum dots have been synthesized by ligand exchange with a hydrophilic surface ligand, namely dihydrolipoic acid.<sup>136-139</sup> Stabilized in buffer solutions, this bidentate water soluble ligand chelates the quantum dots through dithiol groups onto the surface ZnS overcoating, providing an element of enhanced stability<sup>137,138,140</sup> and many avenues for bioconjugation. As seen in Figure 5.7, the isotherm of DHLA capped quantum dots results in a slightly larger limiting molecular area of  $15,500 \text{ \AA}^2/\text{particle}$  and an extremely stable monolayer by collapsing around  $35 \text{ mN/m}$ .

As previously described, an ideal isotherm consists of a period of little interaction followed by an increase in surface pressure, these quantum dots have a defined liquid-expanded and liquid-condensed phase which is not seen in the other isotherms. These phases are evidence of a consistent and homogeneous monolayer which is undergoing

reorientation at the air-water interface as the molecules are compressed together. Unlike other isotherms with hydrophilic moieties, this isotherm does not collapse but rather does not exert more surface pressure upon further compression after  $\sim 35$  mN/m possibly due to expulsion of nanoparticles in the subphase.

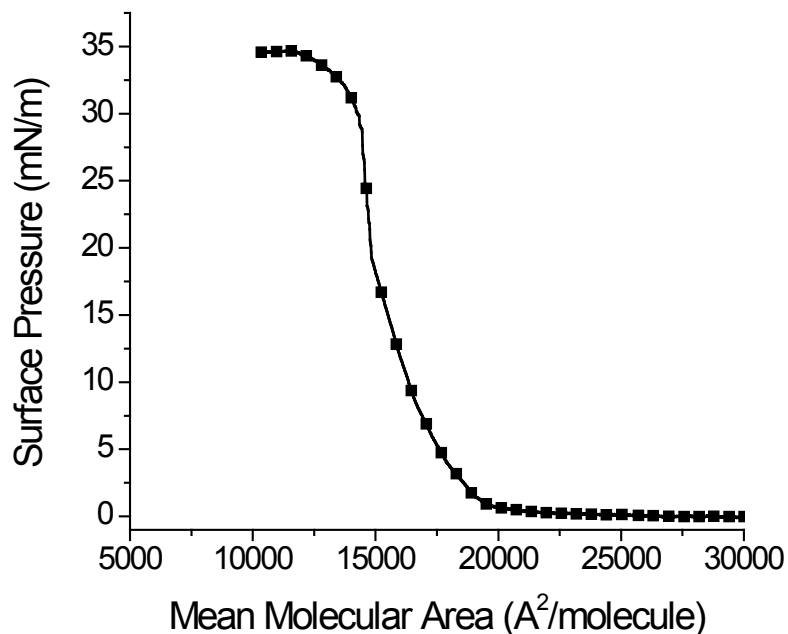


**Figure 5.7** Surface pressure-area isotherm of 0.06 nmol CdSe(ZnS)-DHHLA QDs spread on a pH 5.7, water subphase.

#### *CdSe(ZnS)-MPS*

Hydrophilicity is very interesting in terms of research purposes of bioconjugation and biosensing *in vivo* however, the interparticle distance of quantum dots is also interesting since the propensity to aggregate, as seen in the TEM images, occurs readily. The interparticle distance has been shown in the past to control the interactions between quantum dots with no shell.<sup>136,141,142</sup> Commonly used for these types of three dimensional gels, alkoxysilanes at the air-water interface have been shown to form a polymeric two dimensional films.<sup>143</sup> Further studies<sup>39</sup> were done with CdSe(ZnS) QDs to successfully

control the distance between nanoparticles by applying the sol-gel process in 2D. CdSe(ZnS) QDs were silanized by (3-mercaptopropyl) trimethoxysilane with a homogenous diameter of 3.75 nm as confirm by UV-vis spectroscopy and HR-TEM. Analysis of the CdSe(ZnS) QDs modified by silanization gave the same photophysical and microscopic properties as the unmodified QDs as expected based on the similar lengths of the conjugated TOPO ligand (0.7 nm) and MPS (0.5 nm) molecules.

Subphase manipulation experiments were reproduced which revealed that under neutral conditions, the MPS-QDs did not form close packing however, at a very basic subphase pH, the  $\pi$ -A isotherm presented a condensed phase of low compressibility and collapsed at around 30 mN/m as seen in Figure 5.8.

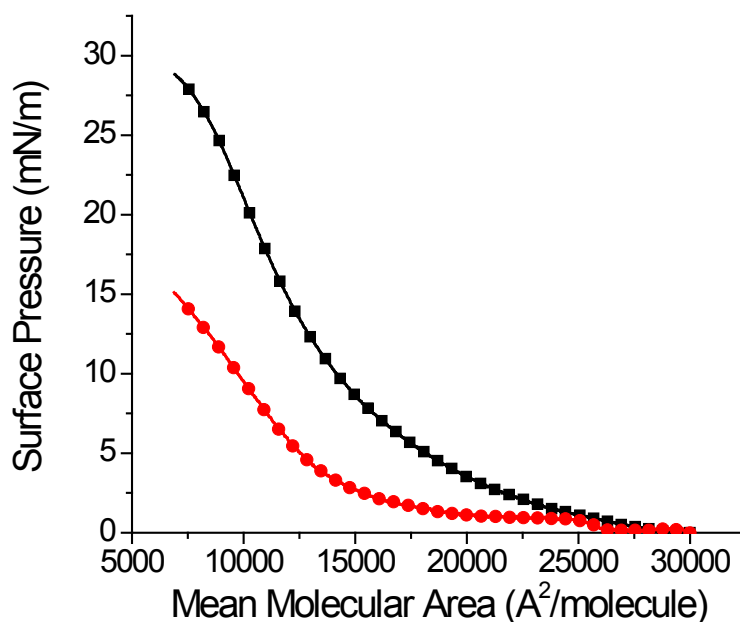


**Figure 5.8** Surface pressure-area isotherm of 0.06 nmol CdSe(ZnS)-MPS QDs spread on a pH 12 (■) and 5.7 (●) subphase.

Analysis of the pH range of each subphase enables a better understanding of bimolecular nucleophilic substitution reactions occurring at the interface. A low pH range is

characterized by a high rate of hydrolysis and a low rate of condensation. Rapid hydrolysis is the key to aggregate formation involving displacement of an alkoxide group leading to cluster-cluster aggregates. These formations are stable however the siloxane bond is irreversibly hydrolyzed before any monomer formation can occur. The aggregates themselves therefore have no structuralization and develop into weak, unsystematic branches. A high pH however involves condensation reactions where the interaction between  $\text{OH}^-$  and  $\text{SiO}^-$  anions occurs rapidly and the protonation/deprotonated simultaneously reacts to form monomer-cluster aggregates which go to completion.<sup>144</sup>

### **5.3 Conclusion**

The surface chemistry and unique optical properties of CdSe and CdSe(ZnS) QDs as well as two different ligands which have been exchanged with the innate TOPO have been studied using Langmuir monolayers. UV-vis absorption of the QD dispersions show a size dependent absorption spectra which was used to calculate the nanoparticle core size as well as the extinction coefficient. Narrow fluorescence spectra show a monodispersed system which is enhanced with the addition of the ZnS shell on the CdSe core by over a tenfold increase in luminescence. Isolated nanoparticle aggregates have been identified by TEM as easily forming aggregates which is slightly reduced by the exchange of the TOPO ligand for a hydrophilic DHLA and even further stabilized as monodispersed with the exchange to MPS. The surface pressure-area isotherm reveals the different behavior of these nanoparticles which increased the limiting molecular area as the quantum dot size increased. Also seen in terms of interfacial behavior is when the subphase is acidic, the quantum dots do not form a monolayer however in an alkaline environment, an expanded film is formed at the interface.

## Chapter 6

### Future Directions

#### 6.1 Protein-lipid interactions

##### *Rationale*

Characterization of a protein and its interaction in different environments begs the question as to how it would interact with different surfactants which are immiscible. Protein-lipid interactions for example are of great importance in biological reactions which occur most at interfaces like the one simulated by the Langmuir technique.<sup>145-153</sup> There are multiple methods by which to go about interacting such molecules but the most desirable imitates physiological conditions.<sup>154-157</sup>

##### *Objective*

Dipalmitoyl phosphatidyl choline (DPPC) has become a phospholipid of wide experimentation based on its importance in the cellular membrane<sup>158</sup> as well as a major constituent of pulmonary surfactant.<sup>159</sup> DPPC is commonly used in the preparation of liposomes therefore studies determining the interaction between these molecules is essential in order to understand their role in a mixed monolayer as well as elucidating the stability of these liposomes when considering practical applications.

Mixed monolayers have been used to understand these interactions and the formation of stable monolayers with and without the mixtures which allow researchers to observe the behavior of the individual molecules. Most commonly, a film of one molecule, usually the lipid, is formed at the air-water interface followed by injecting the protein into the subphase, most commonly water<sup>151,160</sup> however there have been other methods on the experimental parameters.<sup>150,161,162</sup>

Analyzing the behavior of these molecules can be taken a step further by quantifying the number of protein molecules which are interacting with the lipid molecules at the interface. Toimil et al. has conducted research into the interaction of HSA with DPPC. The DPPC monolayer undergoes the phase transition process typical of phospholipid monolayers which are formed below the temperature at which the transition from gel to liquid crystal occurs.<sup>163,164</sup> Mixed monolayers of the two molecules show a contraction of the isotherm as the mole fraction of DPPC is increased. The typical HSA isotherm with no DPPC compared to the isotherm with the most DPPC added lifts off at a later area and has a larger limiting molecular area. Each isotherm has a trend of two noticeable characteristics where below 24 mN/m the molecules are both at the interface and not in competition as the area of the trough decreases. Beyond this surface pressure the isotherms become parallel to one another and all collapse around the same surface pressure. These results are explained again by the miscibility of the two components in a protein-lipid mixed monolayer. Regardless of the protein/DPPC ratio, the hydrocarbon chain arrangements are unchanged and the protein after 24 mN/m is consistently displaced from the interface as seen in previous literature with similar components.<sup>165,166</sup>

Utilizing the knowledge of the model protein HSA can be extended to  $\beta$ -galactosidase to observe the behavior of the molecules in the presence of lipids. As detailed in literature, the head groups of lipids govern the interactions between protein and lipids.<sup>37</sup> Analysis would include the interactions of several lipids including positively charged dioctadecyldimethylammonium bromide (DODAB) and 1,2-distearoyl-sn-glycero-3-ethylphosphocholine chloride salt (DSEPC), negatively charged 1,2-distearoyl-sn-glycero-3-phosphate sodium salt (DSPA) and neutrally charged DPPC head groups.

Similar in terms of their 18-carbon alkyl chain, literature shows that electrostatic interaction governs the incorporation into their monolayers. These studies will reveal the nature and orientation of the enzyme as it interacts with model lipids simulating a cell membrane model system.

## **6.2 Solid support studies of biomacromolecules**

### ***Rationale***

The Langmuir-Blodgett technique provides an expansion on the Langmuir monolayer technique. Along with the formation of multilayer structures on a solid substrate, a wide range of surfactants can be applied such as proteins, phospholipids, fatty acids as well as noncentrosymmetric molecules. Taking advantage of the biomolecules' ability to self-assemble at the air-water interface, the possibility to make ultrathin layers of immobilized, but still active,<sup>167</sup> biomolecules are the basis of biosensors.<sup>168-172</sup> The LB method is elegant in mimicking a system of biological importance.<sup>173</sup> Highly organized and spontaneously assembling, the advantages of LB technology give rise to molecular level instantaneous detection of very low concentrations or activity of target molecules as these systems can also be integrated into bioelectronic devices including immunosensors<sup>155,174</sup> enzyme sensors<sup>175,176</sup> biomolecular microphotodiodes<sup>177,178</sup> and biocatalyst membranes.<sup>157,179,180</sup>

### ***Objective***

Development of such bioelectronic devices highlights advantages over other systems including low amounts of protein or enzyme in the preparation of the layered membrane on the solid substrate. In this change from an air-water interface to an air-solid interface, strong attractive interactions are needed to overcome the molecule's affinity for the



original aqueous subphase environment. While working at desired temperatures and pressures, ambient surroundings avoid the possibility of denaturing the biomolecules while also leaving much room for modification of sensor sensitivity.<sup>168</sup>

In this technique, a substrate is placed vertically at the center of the trough in the subphase before monolayer formation. The ability to modify many parameters of these experiments includes choosing a target surface pressure to transfer the molecules.

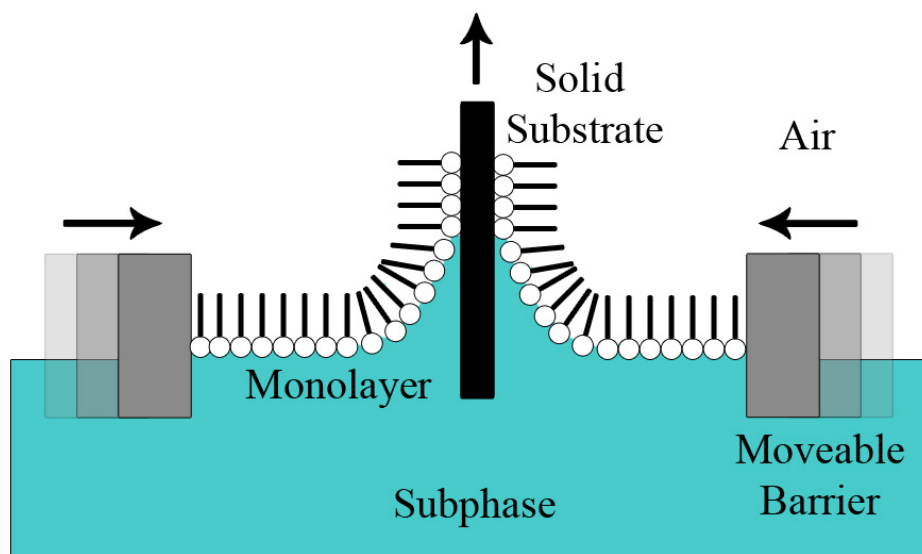


**Figure 6.1 Schematic illustration of a Langmuir-Blodgett film deposition for an ideal amphiphilic molecule.**

In order to retain highly organized arrangements of the molecules as that achieved at the air-water interface, surface pressures are commonly high to minimize the loss of intramolecular cohesion.<sup>168</sup> At the desired point during compression, the substrate is slowly lifted out of the subphase which removes a single layer of surface molecules adhered to the surface exemplified in Figure 6.1. The initial layer formation is crucial and after, multiple layers can be deposited of varying or similar surfactants to the surface of the substrate.<sup>181</sup>

The development of these sensors from LB films has given rise to optimization of techniques to transfer proteins to the surface of a solid substrate by using matrices,<sup>182</sup> highly branched spacer polymers,<sup>183</sup> or direct single to multilayer wetting of the substrate. Transfer of proteins such as serum albumin has innate difficulties due to it having a particular shape, high molecular weight along with a multitude of nonpolar functional groups which are highly soluble in water. Retention of major binding sites of the biomolecule after immobilization on the substrate especially with HSA is of great importance since many compounds bind reversibly making it a broadly usable detector.<sup>184</sup> Given these difficulties serum albumin, along with many other biomacromolecules, create stable films when at the air-water interface.<sup>114,185-187</sup>

Keeping the protein at the interface, reducing the area per residue and obtaining a film with folded molecule chains is of importance therefore a subphase at isoelectric point is ideal. As the monolayer is compressed a coexistence of two protein phases, typical for serum albumin, is observed differing by the protein's secondary structure conformational arrangement at the air-water interface.<sup>114,186-188</sup> Determination of the optimum range for LB film deposition was based on these rearrangements since commonly below 10-15 mN/m the protein monolayer is too expanded and above this range keeping the monolayer stable along with the surface pressure constant has low reproducibility.

LB films are prepared on silanized glass and mica substrates based on the interactions which need to occur when depositing the protein on the surface. The first layer of protein on the substrate is crucial to obtaining a multiple layers on the substrate however mica did not provide enough interaction with the protein to deposit multiple layers. Multiple layers of protein adhesion occurred on silanized glass and a close examination at the

protein characteristics reveals that the nonpolar groups adhere to the substrate leaving the polar regions exposed to the hydrophobic air. Exemplified by lowering the pH, BSA becomes more viscous which increase the  $\alpha$ -helix content thereby intensifying the behavior of the nonpolar groups to attach to the hydrophobic surface.

The kinetics of  $\beta$ -galactosidase as previously discussed in chapter 4 is interesting due to its ability to hydrolyze the glycosidic linkage in specific substrates such as X-gal. By creating a  $\beta$ -galactosidase LB film, this rudimentary sensor when immersed in X-gal would function as a biosensor thereby developing a color change over time. Analysis via UV-vis could prove the activity of the monolayer film leading to the development of glycomics sensors. Reproducibility would be difficult in this case since the single layer of enzyme necessary for activity might vary thereby changing the amount of color detection during substrate interaction. However, attachment of the enzyme to a solid support such as quartz slide would allow enzyme activity to be monitored with X-gal substrate interaction in a more controlled experimental setting.

## REFERENCES

1. Lehninger, A. L.; Nelson, D. L.; Cox, M. M. *Principles of Biochemistry*, W. H. Freeman, New York, **2005**.
2. Westermark, P.; Wernstedt, C.; Wilander, E.; Hayden, D.; O'Brien, T.; Johnson, K. *Proc. Natl. Acad. Sci. U.S.A.* **1987**, *84*, 3881-3885.
3. Westermark, P.; Li, Z.; Westermark, G.; Leckström, A.; Steiner, D. *FEBS Lett.* **1996**, *379*, 203-206.
4. Höppener, J.; Ahrén, B.; Lips, C. *N. Engl. J. Med.* **2000**, *343*, 411-419.
5. Engel, M. F. M.; Khemtémourian, L.; Kleijer, C.; Meeldijk, H.; Jacobs, J.; Verkleij, A.; de Kruijff, B.; Killian, J.; Höppener, J. *Proc. Natl. Acad. Sci. U.S.A.* **2008**, *105*, 6033-6038.
6. Buxbaum, J. N.; Ye, Z.; Reixach, N.; Friske, L.; Levy, C.; Das, P.; Golde, T.; Masliah, E.; Roberts, A. R.; Bartfai, T. *Proc. Natl. Acad. Sci. U.S.A.* **2008**, *105*, 2681-2686.
7. Demuro, A.; Mina, E.; Kayed, R.; Milton, S.; Parker, I.; Glabe, C. G. *J. Biol. Chem.* **2005**, *280*, 17294-17300.
8. Figge, J.; Rossing, T.; Fencl, V. *J. Lab. Clin. Med.* **1991**, *117*, 453-467.
9. Carter, D.; Ho, J. *Adv. Protein Chem.* **1994**, *45*, 153-203.
10. Engel, M. F. M. *Chem. Phys. Lipids* **2009**, *160*, 1-10.
11. Gurlo, T.; Ryazantsev, S.; Huang, C.; Yeh, M.; Reber, H.; Hines, O.; O'Brien, T.; Glabe, C.; Butler, P. *Am. J. Pathol.* **2010**, *176*, 861-869.
12. Daughaday W. *Physiol. Rev.* **1959**, *39*, 885-902.
13. Klopfenstein, W. *Biochim. Biophys. Acta* **1969**, *181*, 323-325.
14. Westphal, U.; Harding, G. *Biochim. Biophys. Acta* **1973**, *310*, 518-527.
15. Goodman, D. *J. Am. Chem. Soc.* **1958**, *80*, 3892-3898.
16. Emerson, T. E., Jr. *Crit. Care Med.* **1989**, *17*, 690-694.
17. Stamler, J.; Singel, J.; Loscalzo, J. *Science* **1992**, *258*, 1898-1902.

18. Rub, M. A.; Khan, J. M.; Yaseen, Z.; Khan, R. H. *J. Prot. Proteomics* **2012**, *3*, 207-215.
19. Jacobson, R. H.; Matthews, B.W. *J. Mol. Biol.* **1992**, *223*, 1177-1182.
20. Lederberg, J. *J. Bacteriol.* **1950**, *60*, 381-392.
21. Juers, D. H.; Jacobson, R. H.; Wigley, D.; Zhang, X. J.; Huber, R. E.; Tronrud, D. E.; Matthews, B. W. *Prot. Sci.* **2000**, *9*, 1685-1699.
22. Gebler, J. C.; Aebersold, R.; Withers, S. G. *J. Biol. Chem.* **1992**, *267*, 11126–11130.
23. Fowler, A. V.; Zabin, I.; Sinnott, M. L.; Zabin I. *J. Biol. Chem.* **1978**, *253*, 5283-5285.
24. Jacobson, R. H.; Zhang, X-J.; DuBose, R. F.; Matthews, B. W. *Nature* **1994**, *369*, 761-766.
25. Ring, M.; Bader, D. E.; Huber, R. E. *Biochem. Biophys. Res. Commun.* **1988**, *152*, 1050-1055.
26. Bader, D. E.; Ring, M.; Huber, R. E. *Biochem. Biophys. Res. Commun.* **1988**, *153*, 301-306.
27. Cupples, C. G.; Miller, J. H.; Huber, R. E. *J. Biol. Chem.* **1990**, *265*, 5512-5518.
28. Juers, D. H.; Heightman, T. D.; Vasella, A.; McCarter, J. D.; Mackenzie, L.; Withers, S. G.; Matthews, B. W. *Biochemistry* **2001**, *40*, 14781-14794.
29. Fowler, A. V.; Zabin, I. *Proc. Natl. Acad. Sci. U.S.A.* **1977**, *74*, 1507–1510.
30. Fowler, A. V.; Zabin, I. *J. Biol. Chem.* **1978**, *253*, 5521-5525.
31. Arrondo, J. L. R.; Muga, A.; Castresana, J.; Bernabeu, C.; Goñi, F. M. *FEBS Lett.* **1989**, *252*, 118-120.
32. Kalnins, A.; Otto, K.; Rütger, U.; Müller-Hill, B. *EMBO J.* **1983**, *2*, 593–597.
33. Johnson, S.; Liu, W.; Thakur, G.; Dadlani, A.; Patel, R.; Orbulescu, J.; Whyte, J. D.; Micic, M.; Leblanc, R. M. *J. Phys. Chem. B* **2012**, *116*, 10205-10212.
34. Thakur, G.; Micic, M.; Leblanc, R. M. *Colloids Surf. B. Biointerfaces* **2009**, *74*, 436-456.
35. Crawford, N. F.; Leblanc, R. M. *Adv. Colloid Interface Sci.* **2013**, *207*, 131-138.

36. Orbulescu, J.; Leblanc, R. M. *J. Phys. Chem. C* **2009**, *113*, 5313-5315.
37. Li, S.; Stein, A. J.; Kruger, A.; Leblanc, R. M. *J. Phys. Chem. C* **2013**, *117*, 16150-16158.
38. Hubbard, A. T. *Encyclopedia of Surface and Colloid Science*, CRC Press, New York, 1st edn., vol. 4, **2002**.
39. Xu, J.; Wang, C.; Wang, J.; Huo, Q.; Crawford, N. F.; Véliz, E. A.; Leblanc, R. M. *J. Colloid Interface Sci.* **2013**, *393*, 21-28.
40. Crawford, N. F.; Leblanc, R. M. *Coord. Chem. Rev.* **2013**, *263*, 13-24.
41. Gaines, G. L., Jr. *Insoluble Monolayers at the Liquid–Gas Interfaces*, Interscience Publishers, New York, **1966**.
42. Feng, S. S. *Langmuir* **1999**, *15*, 998-1010.
43. Nagle, J. F. *J. Membr. Biol.* **1976**, *27*, 233-250.
44. Yudenfreund, M. N.; Becher, P.; Brown, J. B. *Monolayers*, American Chemical Society, **1975**, p 192-201.
45. Jones, M. N.; Capman, D. *Micelles, Monolayers and Biomembranes*, Wiley Publishers, New York, **1995**.
46. Liu, G.; Yang, S.; Zhang, G. *J. Phys. Chem. B* **2007**, *111*, 3633-3639.
47. Orbulescu, J.; Micic, M.; Ensor, M.; Trajkovic, S.; Daunert, S.; Leblanc, R. M. *Langmuir* **2009**, *26*, 3268-3274.
48. Iwamoto, M.; Mizutani, Y.; Sugimura, A. *Phys. Rev. B* **1996**, *54*, 8186-8190.
49. Baoukina, S.; Monticelli, L.; Risselada, H. J.; Marrink, S. J.; Tieleman, D. P. *Proc. Natl. Acad. Sci. U.S.A.* **2008**, *105*, 10803-10808.
50. Santos, N. C.; Castanho, M. A. R. B. *Trends Appl. Spectrosc.* **2002**, *4*, 113-125.
51. Edelhoich, H. *Biochemistry* **1967**, *6*, 1948-1954.
52. Becker, V. E.; Evans, H. J. *Biochim. Biophys. Acta, Protein Struct. Mol. Enzymol.* **1969**, *191*, 95-104.
53. Reithel, F. J.; Kim, J. C. *Arch. Biochem. Biophys.* **1960**, *90*, 271-277.
54. Neville, M. C.; Ling, G. N. *Arch. Biochem. Biophys.* **1967**, *118*, 596-610.

55. Siegel, J. B.; Steinmetz, W. E.; Long, G. L. *Anal. Biochem.* **1980**, *104*, 160-167.
56. Nakanishi, K.; Berova, N.; Woody, R. W. *Circular Dichroism Principles and Applications*, VCH Publisher, New York, **1994**; p 476-481.
57. Whitmore, L.; Wallace, B. A. *Biopolymers* **2007**, *89*, 392-400.
58. Byler, D. M.; Susi, H. *Biopolymers* **1986**, *25*, 469-487.
59. Surewicz, W. K.; Mantsch, H. H. *Biochim. Biophys. Acta, Protein Struct. Mol. Enzymol.* **1988**, *952*, 115-130.
60. Vagharchakian, L.; Desbat, B.; Hénon, S. *Macromolecules* **2004**, *37*, 8715-8720.
61. Dluhy, R. A. *Appl. Spectrosc. Rev.* **2000**, *35*, 315-351.
62. Jackson, M.; Mantsch, H. H. *Crit. Rev. Biochem. Mol. Biol.* **1995**, *30*, 95-120.
63. Pribie, R.; van Stokkum, I. H. M.; Chapman, D.; Haris, P. I.; Bolemendal, M. *Anal. Biochem.* **1993**, *214*, 366-378.
64. Surewicz, W. K.; Mantsch, H. H.; Chapman, D. *Biochemistry* **1993**, *32*, 389-394.
65. Arrondo, J. L. R.; Muga, A.; Castresana, J.; Goñi, F. M. *Prog. Biophys. Mol. Bio.* **1993**, *59*, 23-56.
66. Zhou, W.; Schaack, J.; Zawada, W. M.; Freed, C. R. *Brain Res.* **2002**, *926*, 42-50.
67. Chan, W. C. W.; Nie, S. *Science* **1998**, *281*, 2016-2018.
68. Bruchez, M., Jr.; Moronne, M.; Gin, P.; Weiss, S.; Alivisatos, A. P. *Science* **1998**, *281*, 2013-2016.
69. Jaiswal, J. K.; Mattoussi, H.; Mauro, J. M.; Simon, S. M. *Nat. Biotechnol.* **2002**, *21*, 47-51.
70. Jaiswal, J. K.; Goldman, E. R.; Mattoussi, H.; Simon, S. M. *Nat. Methods* **2004**, *1*, 73-78.
71. Gao, X.; Cui, Y.; Levenson, R. M.; Chung, L. W.; Nie, S. *Nat. Methods* **2004**, *22*, 969-976.
72. Gattás-Asfura, K. M.; Constantine, C. A.; Lynn, M. J.; Thimann, D. A.; Ji, X.; Leblanc, R. M. *J. Am. Chem. Soc.* **2005**, *127*, 14640-14646.

73. Noh, M.; Kim, T.; Lee, H.; Kim, C.; Joo, S.; Lee, K. *Colloids Surf. A.* **2010**, *359*, 39-44.
74. Reiss, P.; Bleuse, J.; Pron, A. *Nano Lett.* **2002**, *7*, 781-784.
75. Wang, X.; Qu, L.; Zhang, J.; Peng, X.; Xiao, M. *Nano Lett.* **2003**, *8*, 1103-1106.
76. Han, H.; Cai, Y.; Liang, J.; Sheng, Z. *Anal. Sci.* **2007**, *23*, 651-654.
77. Mattoussi, H.; Mauro, J. M.; Goldman, E. R.; Anderson, G. P.; Sundar, V. C.; Mikulec, F. V.; Bawendi, M. G. *J. Am. Chem. Soc.* **2000**, *122*, 12142-12150.
78. Nandhakumar, I. S.; Gabriel, T.; Li, X.; Attard, G. S.; Markham, M.; Smith, D. C.; Baumberg, J. J. *Chem. Commun.* **2004**, *12*, 1374-1375.
79. Lin, Y.; Skaff, H.; Emrick, T.; Dinsmore, A. D.; Russell, T. P. *Science* **2003**, *299*, 226-229.
80. Guldi, D. M.; Zilbermann, I.; Anderson, G.; Kotov, N. A.; Tagmatarchis, N.; Prato, M. *J. Am. Chem. Soc.* **2004**, *126*, 14340-14341.
81. Yang, Y.; Pradhan, S.; Chen, S. *J. Am. Chem. Soc.* **2004**, *126*, 76-77.
82. Dabbousi, B. O.; Murray, C. B.; Rubner, M. F.; Bawendi, M. G. *Chem. Mater.* **1994**, *6*, 216-219.
83. Murphy, C.; Coffey, J. L. *Appl. Spectrosc.* **2002**, *56*, 16A-27A.
84. Brus, L. *J. Phys. Chem.* **1986**, *90*, 2555-2560.
85. Kippelen, T.; Swafford, L. A.; Rosenthal, S. A. *J. Chem. Educ.* **2002**, *79*, 1094-1100.
86. Wallenfels, K.; Rudolf, W. *The Enzymes*, Academic Press, New York, vol. 7, **1972**, p 617-663.
87. Denney, R. C.; Sinclair R. *Visible and Ultraviolet Spectroscopy*, Wiley Publisher, New York, **1987**.
88. Hunter, M. J.; McDuffie, F. C.; *J. Am. Chem. Soc.* **1959**, *81*, 1400-1406.
89. Craven, G. R.; Steers, E.; Anfinsen, C. B. *J. Biol. Chem.* **1965**, *240*, 2468-2477.
90. Lakowicz, J. R. *Principles of Fluorescence Spectroscopy*, Springer Science, LLC, New York, 3rd edn., **2006**.
91. Hirst, J. D.; Colella, K.; Gilbert, A. T. *J. Phys. Chem. B* **2003**, *107*, 11813-11819.



92. Sreerama, N.; Venyaminov, S. Y.; Woody, R. W. *Prot. Sci.* **1999**, *8*, 370-380.
93. Provencher, S. W.; Gloeckner, J. *Biochemistry* **1981**, *20*, 33-37.
94. van Stokkum, I. H.; Spoelder, H. J.; Bloemendal, M.; van Grondelle, R.; Groen, F. C. A. *Anal. Biochem.* **1990**, *191*, 110-118.
95. Mendelsohn, R.; Brauner, J. W.; Gericke, A. *Annu. Rev. Phys. Chem.* **1995**, *46*, 305-334.
96. Peng, Z. A.; Peng, X. G. *J. Am. Chem. Soc.* **2001**, *123*, 183-184.
97. Engel, M. F. M.; Yigittop, H.; Elgersma, R. C.; Rijkers, D. T. S.; Liskamp, R. M. J.; de Kruijff, B.; Höppener, J. W. M.; Killian, J. A. *J. Mol. Biol.* **2006**, *356*, 783-789.
98. Leblanc, R. M. *Curr. Opin. Chem. Biol.* **2006**, *10*, 529-536.
99. Khemtémourian, L.; Lahoz Casarramona, G.; Suylen, D. P.; Hackeng, T. M.; Meeldijk, J. D.; de Kruijff, B.; Höppener, J. W. M.; Killian, J. A. *Biochemistry* **2009**, *48*, 10918-10925.
100. Holm, B. A.; Notter, R. H.; Finkelstein, J. N. *Chem. Phys. Lipids* **1985**, *38*, 287-298.
101. Holm, B. A.; Enhorning, G.; Notter, R. H. *Chem. Phys. Lipids* **1988**, *49*, 49-55.
102. Dluhy, R. A.; Cornell, D. G. *J. Phys. Chem.* **1985**, *89*, 3195-3197.
103. Trillo, J. M.; Iribarnegaray Jado, E.; García Fernández, S.; Sanz Pedrero, S. *Kolloid Z. Z. Polym.* **1972**, *250*, 318-324.
104. Trillo, J. M.; Iribarnegaray Jado, E.; García Fernández, S.; Sanz Pedrero, S. *Kolloid Z. Z. Polym.* **1972**, *250*, 325-329.
105. MacRitchie, F. *Adv. Colloid Interface Sci.* **1986**, *25*, 341-385.
106. Chiti, F.; Dobson, C. M. *Annu. Rev. Biochem.* **2006**, *75*, 333-366.
107. Fändrich, M. *Cell. Mol. Life Sci.* **2007**, *64*, 2066-2078.
108. Stefani, M.; Dobson, C. M. *J. Mol. Med.* **2003**, *81*, 678-699.
109. Dobson, C. M. *Nature* **2003**, *426*, 884-890.
110. Pace, C. N.; Vajdos, F.; Fee, L.; Grimsley, G.; Gray, T. *Prot. Sci.* **1995**, *4*, 2411-2423.

111. Tello-Solis, S. R.; Jiménez-Guzmán, J.; Sarabia-Leos, C.; Gómez-Ruiz, L.; Cruz-Guerrero, A. E.; Rodríguez-Serrano, G. M.; García-Garibay, M. *J. Agric. Food Chem.* **2005**, *53*, 10200-10204.
112. Dexter, D. L. *J. Chem. Phys.* **1953**, *21*, 836-850.
113. Kiernan, J. A. *Biotech. Histochem.* **2007**, *82*, 73-103.
114. Sánchez-González, J.; Cabrerizo-Vílchez, M. A.; Gálvez-Ruiz, M. J. *Colloids Surf. B. Biointerfaces* **2001**, *21*, 19-27.
115. Henglein, A. *Ber. Bunsenges. Phys. Chem.* **1982**, *86*, 301-305.
116. Qu, L.; Peng, Z. A.; Peng, X. *Nano Lett.* **2001**, *1*, 333-336.
117. Yu, W. W.; Peng, X. *Angew. Chem. Int. Ed.* **2002**, *41*, 2368-2371.
118. Dai, Q.; Lei, D.; Chen, H.; Kan, S.; Li, H.; Gao, S.; Hou, Y.; Liu, B.; Zou, G. *J. Phys. Chem. B* **2006**, *110*, 16508-16513.
119. Hines, M. A.; Guyot-Sionnest, P. *J. Phys. Chem.* **1996**, *100*, 468-471.
120. Dabbousi, B. O.; Rodriguez-Viejo, J.; Mikulec, F. V.; Heine, J. R.; Mattoussi, H.; Ober, R.; Jensen, K. F.; Bawendi, M. G. *J. Phys. Chem. B* **1997**, *101*, 9463-9475.
121. Ebenstein, Y.; Mokari, T.; Banin, U. *J. Phys. Chem. B* **2004**, *108*, 93-99.
122. Murray, C. B.; Norris, D. J.; Bawendi, M. G. *J. Am. Chem. Soc.* **1993**, *115*, 8706-8715.
123. Yu, W. W.; Qu, L.; Guo, W.; Peng, X. *Chem. Mater.* **2003**, *15*, 2854-2860.
124. Leatherdale, C. A.; Woo, W. K.; Mikulec, F. V.; Bawendi, M. G. *J. Phys. Chem. B* **2002**, *106*, 7619-7622.
125. Schmelz, O.; Mews, A.; Basche, T.; Herrmann, A.; Mullen, K. *Langmuir* **2001**, *17*, 2861-2865.
126. Striolo, A.; Ward, J.; Prausnitz, J. M.; Parak, W. J.; Zanchet, D.; Gerion, D.; Milliron, D.; Alivisatos, A. P. *J. Phys. Chem. B* **2002**, *106*, 5500-5505.
127. Dong, C.; Ren, J. *Analyst* **2010**, *135*, 1395-1399.
128. Alivisatos, A. P. *Science* **1996**, *271*, 933-937.
129. Sui, G.; Ji, X.; Leblanc, R. M. *J. Cluster Sci.* **2003**, *14*, 123-133.

130. Taylor, J.; Kippeny, T.; Rosenthal, S. J. *J. Cluster Sci.* **2001**, *12*, 571-582.
131. Xu J.; Wang C.; Leblanc R. M. *Colloids Surf. B. Biointerfaces* **2009**, *70*, 163-168.
132. Kotov, N. A.; Meldrum, F. C.; Wu, C.; Fendler, J. H. *J. Phys. Chem.* **1994**, *98*, 2735-2738.
133. Lambert, K.; Justo, Y.; Sundar, J.; Hens, Z. *Angew. Chem.* **2011**, *123*, 12264-12267.
134. Jiang, J.; Krauss, T. D.; Brus, L. E. *J. Phys. Chem. B* **2000**, *104*, 11936-11941.
135. Peng, X. G.; Schlamp, M. C.; Kadavanich, A. V.; Alivisatos, A. P. *J. Am. Chem. Soc.* **1997**, *119*, 7019-7029.
136. Kimura, J.; Uematsu, T.; Maenosono, S.; Yamaguchi, Y. *J. Phys. Chem. B* **2004**, *108*, 13258-13264.
137. Coe, S.; Woo, W.; Bawendi, M. G.; Bulovic, V. *Nature* **2002**, *420*, 800-803.
138. Lambert, K.; Moreels, I.; Van Thourhout, D.; Hens, Z. *Langmuir* **2008**, *24*, 5961-5966.
139. Lowman, G. M.; Nelson, S. L.; Graves, S. M.; Strouse, G. F.; Buratto, S. *Langmuir* **2004**, *20*, 2057-2059.
140. Santhanam, V.; Andres, R. P. *Nano Lett.* **2004**, *4*, 41-44.
141. Xu, J.; Ji, X.; Gattás-Asfura, K. M.; Wang, C.; Leblanc, R. M. *Colloids Surf. A.* **2006**, *284*, 35-42.
142. Döllerfeld, H.; Weller, H.; Eychmüller, A. *Nano Lett.* **2001**, *1*, 267-269.
143. Puccetti, G.; Leblanc, R. M. *Photochem. Photobiol.* **2000**, *71*, 426-430.
144. Brinker C. J.; Scherer, G. W. *Sol–Gel Science: The Physics and Chemistry of Sol–Gel Processing*, Academic Press, San Diego, CA, **1990**.
145. Caetano, W.; Ferreira, M.; Tabak, M.; Sanchez, M. I. M.; Oliveira, O. N.; Kruger, P.; Schalke, M.; Losche, M. *Biophys. Chem.* **2001**, *91*, 21-35.
146. de Souza, N. C.; Caetano, W.; Itri, R.; Rodrigues, C. A.; Oliveira, O. N.; Giacometti, J. A.; Ferreira, M. *J. Colloid Interface Sci.* **2006**, *297*, 546-553.
147. Vernoux, N.; Maniti, O.; Besson, F.; Granjon, T.; Marcillat, O.; Vial, C. *J. Colloid Interface Sci.* **2007**, *310*, 436-445.

148. Wang, X. L.; He, Q.; Zheng, S. P.; Brezesinski, G.; Möhwald, H.; Li, J. B. *J. Phys. Chem. B* **2004**, *108*, 14171-14177.
149. Boussaad, S.; Dziri, L.; Arechabaleta, R.; Tao, N. J.; Leblanc, R. M. *Langmuir* **1998**, *14*, 6215-6219.
150. Wang, X.; Zhang, Y.; Wu, J.; Wang, M.; Cui, G.; Li, J.; Brezesinski, G. *Colloids Surf. B. Biointerfaces* **2002**, *23*, 339-347.
151. Wang, X.; Zhang, H. J.; Cui, G. C.; Li, J. B. *J. Mol. Liq.* **2001**, *90*, 149-156.
152. Ihalainen, P.; Peltonen, J. *Langmuir* **2003**, *19*, 2226-2230.
153. Rodland, I.; Halskau, O.; Martinez, A.; Holmsen, H. *Biochim. Biophys. Acta, Biomembr.* **2005**, *1717*, 11-20.
154. Girard-Egrot, A. P.; Chauvet, J. P.; Boullanger, P.; Coulet, P. R. *Langmuir* **2001**, *17*, 1200-1208.
155. Girard-Egrot, A. P.; Godoy, S.; Chauvet, J. P.; Boullanger, P.; Coulet, P. R. *Biochim. Biophys. Acta, Biomembr.* **2003**, *1617*, 39-51.
156. Kiss, E.; Dravetzky, K.; Hill, K.; Kutnyanszky, E.; Varga, A. *J. Colloid Interface Sci.* **2008**, *325*, 337-345.
157. Yin, F.; Kafi, A. K. M.; Shin, H. K.; Kwon, Y. S. *Thin Solid Films* **2005**, *488*, 223-229.
158. Zasadzinski, J. A.; Ding, J.; Warriner, H. E.; Bringezu, F.; Waring, A. J. *Curr. Opin. Colloid Interface Sci.* **2001**, *6*, 506-513.
159. Warriner, H. E.; Ding, J.; Waring, A. J.; Zasadzinski, J. A. N. *Biophys. J.* **2002**, *82*, 835-842.
160. Glomm, W. R.; Volden, S.; Halskau, Ø., Jr.; Ese, M. H. G. *Anal. Chem.* **2009**, *81*, 3042-3050.
161. Zhang, H.; Wang, X.; Cui, G.; Li, J. B. *Colloids Surf. A* **2000**, *175*, 77-82.
162. Li, J. B.; Zhao, J.; Wu, J.; Miller, R. *Nahrung* **1998**, *42*, 232-233.

163. Toimil, P.; Prieto, G.; Miñones, J., Jr.; Sarmiento, F. *Phys. Chem. Chem. Phys.* **2010**, *12*, 13323-13332.
164. Horn, L. W.; Gershfeld, N. L. *Biophys. J.* **1977**, *18*, 301-310.
165. Conde, J. M.; Trillo, J. M.; Rodríguez Patino, J. M. *J. Phys. Chem. B* **2006**, *110*, 11582-11591.
166. Toimil, P.; Prieto, G.; Miñones, J., Jr.; Trillo, J. M.; Sarmiento, F. *Colloids Surf. B. Biointerfaces* **2012**, *92*, 64-73.
167. Caseli, L.; Furriel, R. P. M.; de Andrade, J. F.; Leone, F. A.; Zanicuelli, M. E. D. *J. Colloid Interface Sci.* **2004**, *275*, 123-130.
168. Girard-Egrot, A. P.; Godoy, S.; Blum, L. J. *Adv. Colloid Interface Sci.* **2005**, *116*, 205-225.
169. Caseli, L.; Moraes, M. L.; Zucolotto, V.; Ferreira, M.; Nobre, T. M.; Zanicuelli, M. E. D.; Rodrigues-Filho, U. P.; Oliveira, P. N. *Langmuir* **2006**, *22*, 8501-8508.
170. Caseli, L.; Crespilho, F. N.; Nobre, T. M.; Zanicuelli, M. E. D.; Zucolotto, V.; Oliveira, O. N. *J. Colloid Interface Sci.* **2008**, *319*, 100-108.
171. Schmidt, T. F.; Caseli, L.; Viitala, T.; Oliveira, O. N. *Biochim. Biophys. Acta* **2008**, *178*, 2291-2297.
172. Caseli, L.; Perinotto, A. C.; Viitala, T.; Zucolotto, V.; Oliveira, O. N. *Langmuir* **2009**, *25*, 3057-3061.
173. Rosilio, V.; Boissonnade, M. M.; Zhang, J.; Jiang, L.; Baszkin, A. *Langmuir* **1997**, *13*, 4669-4675.
174. Oh, B. K.; Chun, B. S.; Park, K. W.; Lee, W. C.; Lee, W. H.; Choi, J. W. *Mater. Sci. Eng., C* **2004**, *24*, 65-69.
175. Caseli, L.; Zanicuelli, M. E. D.; Furriel, R. P. M.; Leone, F. A. *Colloids Surf. B. Biointerfaces* **2002**, *25*, 119-128.
176. Paternolli, C.; Ghisellini, P.; Nicolini, C. *Mater. Sci. Eng., C* **2002**, *22*, 155-159.

177. Oh, S. Y.; Park, J. K.; Ko, C. B.; Choi, J. W. *Biosens. Bioelectron.* **2003**, *19*, 103-108.
178. Choi, J. W.; Nam, Y. S.; Kong, B. S.; Choi, H. G.; Lee, W. H.; Fujihira, M. *Colloids Surf. B. Biointerfaces* **2002**, *23*, 263-271.
179. Pastorino, L.; Nicolini, C. *Mater. Sci. Eng., C* **2002**, *22*, 419-422.
180. Pastorino, L.; Berzina, T. S.; Troitsky, V. I.; Fontana, M. P.; Bernasconi, E.; Nicolini, C. *Colloids Surf. B. Biointerfaces* **2002**, *23*, 357-363.
181. Sánchez-González, J.; Ruiz-García, J.; Gálvez-Ruiz, M. J. *J. Colloid Interface Sci.* **2003**, *267*, 286-293.
182. Ramanathan, K.; Ram, M. K.; Malhotra, B. D.; Murthy, A. S. N. *Mater. Sci. Eng., C* **1995**, *3*, 159-163.
183. Anzai, J.; Lee, S.; Osa, T. *Makromol. Chem., Rapid Commun.* **1989**, *10*, 167-170.
184. Frostell-Karlsson, A.; Remaeus, A.; Roos, H.; Andersson, K.; Borg, P.; Hamalainen, M.; Karlsson, R. *J. Med. Chem.* **2000**, *43*, 1986-1992.
185. Roberts, G. G. *Langmuir Blodgett Films*, Plenum Press, New York, **1990**.
186. MacRitchie, F. *Chemistry at interfaces*, Academic Press, San Diego, CA, **1990**.
187. MacRitchie, F. *J. Colloid Interface Sci.* **1997**, *61*, 223-226.
188. Ahluwalia, A.; De Rossi, D.; Monici, M.; Schirone, A. *Biosens. Bioelectron.* **1991**, *6*, 133-141.

## VITA

Nicholas Franklin Crawford, born in Abington Hospital to Howard and Gina Crawford on January 12, 1988, was raised in Willow Grove, a suburb of Philadelphia, PA. Nicholas' education began at St. David Roman Catholic Church under the guidance of Reverend Monsignor Richard T. Bolger. In May 2006, he graduated from La Salle College High School in Wyndmoor, PA with honors and was accepted to the Honors program at Temple University in Philadelphia, PA. While attending, Nicholas focused his studies on Chemistry while participating in the Temple University Diamond Marching Band and met his wife, Karolina, in his sophomore year. After graduating with honors and a B.S. in Chemistry with a Mathematics minor in May 2010, Nicholas and his wife were soon wed. Both traveled to Miami, FL where Nicholas began his graduate studies in the Department of Chemistry at the University of Miami where during his first year he joined Dr. Roger M. Leblanc's research group. Working as a teaching assistant, his graduate work detailed the usage of the Langmuir and spectroscopic techniques to understand and characterize biomacromolecules and in June 2014, Nicholas Crawford graduated with a Ph.D. in Chemistry from the University of Miami. This thesis presents the major findings of his work and listed below are the major publications relating to this research throughout his graduate career.

1. Xu, J.; Wang, C.; Wang, J.; Huo, Q.; Crawford, N. F.; Véliz, E. A.; Leblanc, R. M. *J. Colloid Interface Sci.* **2013**, *393*, 21-28.
2. Crawford, N. F.; Leblanc, R. M. *Coord. Chem. Rev.* **2013**, *263*, 13-24.
3. Crawford, N. F.; Leblanc, R. M. *Adv. Colloid Interface Sci.* **2013**, *207*, 131-138.
4. Crawford, N. F.; Micic, M.; Orbulescu, J.; Weissbart, D.; Leblanc, R. M. *Langmuir* (submitted) **2014**.
5. Crawford, N. F.; Micic, M.; Orbulescu, J.; Leblanc, R. M. *Colloids Surf. A.* (submitted) **2014**.

Permanent Address: 232 Lawnton Rd. Willow Grove, PA 19090